Study of the electronic structure, magnetic and superconducting properties of $Zn_{(1-x)}$(Fe, V)$_x$Se$_y$Te$_{(1-y)}$ materials using computational and experimental method

Kunsa Haho Habura

A PhD Dissertation Submitted to the Department of Applied Physics,
School of Applied Natural Science

Presented in a Partial Fulfillment of the Requirement for the Degree of
Doctor of Philosophy in Applied Physics (Condensed Matter Physics)

Office of Graduate Studies
Adama Science and Technology University

November 2023
Adama, Ethiopia

Study of the electronic structure, magnetic and superconducting properties of $Zn_{(1-x)}$(Fe, V)$_x Se_y Te_{(1-y)}$ materials using computational and experimental method

PhD Candidate:
Kunsa Haho Habura

Major-supervisor:
Dr. Mesfin Asfaw[1] (Associate Prof. of Physics)

Co-supervisor:
Prof. Fekadu Gashaw[2] (Professor of Physics)

[1]Adama Science and Technology University, Department of Applied Physics, P.O.Box 1888, Adama, Ethiopia
[2]Addis Ababa University, Department of Physics, P.O.Box 1176, Addis Ababa, Ethiopia

A Dissertation Submitted to the Department of Applied Physics,
School of Applied Natural Science

Presented in a Partial Fulfillment of the Requirement for the Degree of Doctor of Philosophy in Applied Physics(Specialization in Condensed Matter Physics)

Office of Graduate Studies
Adama Science and Technology University

November 2023
Adama, Ethiopia

DECLARATION

I hereby declare that this PhD Dissertation entitled "**Study of the electronic structure, magnetic and superconducting properties of $\mathbf{Zn_{(1-x)}(Fe, V)_xSe_yTe_{(1-y)}}$ materials using computational and experimental method**" is my original work and has not been submitted the award of any academic degree, diploma or certificate in any other university. All sources of material used for this dissertation have been duly acknowledged through appropriate citations.

(Name of Candidate)	Signature	Date

RECOMMENDATION

I/we, the supervisor(s) of this dissertation, hereby certify that I/we have read and revise the dissertation entitled "Study of the electronic structure, magnetic and superconducting properties of $Zn_{(1-x)}(Fe,V)_xSe_yTe_{(1-y)}$ materials using computational and experimental method", prepared under my/our guidance by **Kunsa Haho Habura** submitted in the partial fulfillment of the requirements for the degree of Doctor of Philosophy in **Applied Physics (specialization in a condensed matter physics)**. Therefore, I/we recommend the submission of the dissertation to the department for further review and defense.

(Supervisor)	Signature	Date
(Co-supervisor)	Signature	Date

APPROVAL SHEET

I/We, certify that the recommendations and suggestions made by the board of examiners are appropriately incorporated into the final version of the dissertation entitled "Study of the electronic structure, magnetic and superconducting properties of $Zn_{(1-x)}(Fe, V)_xSe_yTe_{(1-y)}$ materials using computational and experimental method" by **Kunsa Haho Habura**.

(Supervisor)	Signature	Date
(Co-supervisor)	Signature	Date

We, the undersigned, members of the Board of Examiners of the dissertation open defense by **Kunsa Haho Habura** have read and evaluated the dissertation entitled "Study of the electronic structure, magnetic and superconducting properties of $Zn_{(1-x)}(Fe, V)_xSe_yTe_{(1-y)}$ materials using computational and experimental method" and examined the candidate during open defense. This is therefore to certify that the dissertation is accepted for partial fulfillment of the requirement of the degree of Doctor of Philosophy in **Applied Physics (Specialization in Condensed Matter Physics)**

(Chairperson)	Signature	Date
(Internal Examiner 1)	Signature	Date
(Internal Examiner 2)	Signature	Date
(External Examiner 1)	Signature	Date
(External Examiner 2)	Signature	Date

Final approval and acceptance of the dissertation proposal is contingent upon submission of its final copy to the Office of Postgraduate Studies (OPGS) through the Department Graduate Council (DGC) and School Graduate Committee (SGC).

(Department Head)	Signature	Date
(School Dean)	Signature	Date
(Office of Postgraduate Studies, Dean)	Signature	Date

ACKNOWLEDGMENT

First and foremost, I would like to thank the Almighty God for providing me with health, knowledge, and perseverance during my research work, as well as tolerance in all parts of life's complexities, obstacles, ups and downs, and finally allowing me to win it with a great battle. Next, I would like to express my heartfelt gratitude to **Dr. Mesfin Asfaw**, who is my **supervisor** for this research as well as my instructor, for showing me all the ways during my research work, motivating and encouraging me when I felt discouraged, and providing constructive suggestions and scientific criticism on my trials. Furthermore, I appreciate him for his brotherly and fatherly approach, as well as his unfailing support and encouragement during this research endeavor and my total stay during my PhD studies. I would also like to thank **Prof. Fekadu Gashaw**, my **co-supervisor** for this research. He assisted me by criticizing my efforts, making helpful suggestions, sharing materials, and assisting me in resolving all technical issues encountered throughout my job. His scientific passion, sincerity, and over-the-top enthusiasm left a lasting impression on me.

I would also like to thank **Mr. Manza Ztiyab**, a friend and Ph.D. candidate in condensed matter physics from Adama Science and Technology University, for his diligent assistance in providing helpful comments. My heartfelt gratitude also goes to my classmate and Ph.D. candidate in condensed matter physics, **Mrs. Membere W/Sadik Sema**, an amazing classmate who assists me in providing useful recommendations during my work.

It is also difficult to leave Adama Science and Technology University without thanking the applied physics laboratory technicians and attendants, **Mr. Leuleseged Bekele** and **Mr. Deja Bayissa**, who was extremely friendly and gave unreserved support during my laboratory work. My heartfelt thanks also go to **Mr. Chilotaw Tona**, a staff member in the Department of Physics at Arbaminch University who relentlessly assisted me with technical challenges concerning my study when I was in Adama. I thank the department of **applied physics** and Adama Science and Technology University in general, as well as all staff members in the applied physics department at **Arbaminch University** for financial support, and the Federal Ministry of Education (particularly **Mrs. Lensa Abera**) for providing HPC accounts for computational work.

Again, I'd like to thank my elder brothers **Halala Haho**, **Falaha Haho**, and my mother **Ganie Galo** for their moral and financial support. Also, I'd like to thank my father, **Haho Habura**, who is unlucky to see these good days.

Last but not least, I would like to thank my beloved wife, w/ro **Tigist Debalke Dalcho**, for her decision to care for a family while I was studying. It is also time to honor my little king, **Naod Kunsa**, for his maturity and understanding of things when I was away from home.

TABLE OF CONTENTS

LIST OF FIGURES

LIST OF TABLES

LIST OF ACRONYMS AND ABBREVIATIONS

XRD	X-ray Diffraction
PL	Photo luminescence
UV-V	Ultra violet visible Spectroscopy
FHW	Full Half Width
DFT	Density functional Theory
RTM	Room Temperature Magnetism
HSC	High Superconductors
GGA	General Gradient Approximation
LDA	Local Density Approximation
FM	Ferromagnetic
AFM	Antiferromagnetic
CBD	Chemical bath deposition
PH	Potential of hydrogen
RF	Radio frequency
LED	Light emitting diode
JCPDS	Joint committee on power diffraction standards
ICCD	International center for the diffraction data
FWHM	Full width half maxima
PBE	Predew-Burke-Ernzerhof
USPP	Ultra soft pseudo potential
MFA	Mean Field Approximation
NM	Non-Magnetic
DOS	Density of states
TDOS	Total density of states
LO	Longitudinal optical
TO	Transverse optical
LA	LOngitudinal acoustic
TA	Transverse acoustic
BCS	Bardeen Cooper Schrieffer
EPW	Electron-phonon wanner

ABSTRACT

The quaternary compound $Zn_{(1-x)}(Fe, V)_xSe_yTe_{(1-y)}$ is a transition metal chalcogenide with fascinating properties that can be employed in electronics, energy storage, spintronics, and magneto-optical devices. The need for alloying and doping these types of materials is largely for further optimization for better and more specialized applications. The electronic structure, magnetic, vibrational, and superconducting properties of the $Zn_{(1-x)}(Fe, V)_xSe_yTe_{(1-y)}$ materials and their fragments are investigated using both computational and experimental methods. In the computational approach, both DFT and DFT+U approximations were considered. For this study, the quantum espresso and electron-phonon wannier (EPW) programs were employed. The second section of this dissertation focuses on synthesizing the iron-doped ZnSe (i.e., $Zn_{(1-x)}Fe_xSe$) thin films by the chemical bath deposition method to understand how structural, electrical, and optical features are affected by iron doping. This study revealed that the DFT+U calculation enhances the electrical properties more than the DFT approximation. When the iron concentration in $Zn_{(1-x)}Fe_xSe$ is less than 12.5%, half-metallic qualities are observed, while greater concentrations are in spin glass states, which is compatible with the experimental observations reported. However, vanadium doping demonstrated that the $Zn_{(1-x)}V_xSe$ can behave as a dilute magnetic material even at room temperature, with potential applications in spintronics and magneto-optical devices. Remarkably, the doping of iron and vanadium in ZnSe results in considerable changes to the system's structural, electrical, and magnetic properties. Furthermore, while theoretically it is conceivable to generate n-type iron and vanadium-co-doped ZnTe semiconductors, obtaining n-type ZnTe semiconductors has remained disputed. The iron selenide-based superconductors are one of four families of iron-based superconductors that exhibit enhancements in magnetic and superconducting properties over time. However, the anisotropic and isotropic superconducting behavior of FeSe remains challenging. In this case, the isotropic behavior of the tetragonal FeSe superconductor was investigated. It revealed that the superconductivity critical temperature enhancement up to 26 K is theoretically possible under room conditions. Also, the experimental results indicate that the determined lattice constant and band gap of the iron-doped system are decreasing as the iron concentration increases. This is consistent with the DFT result, except that the band gap of the DFT result lags behind due to discontinuities in the functional used.

***Key Words**: Ferromagnetism, Electronic Structure, Superconductivity, ZnSe, ZnTe, Thin Films, FeSe, Hubbard Parameter, Lattice Vibration, Chalcogenides, Transition Metal Doped*

1. INTRODUCTION

1.1. Background

Dilute magnetic semiconductors (DMSs) are a class of semiconductors that can display normal electrical and magnetic properties, as well as novel ones such as large Faraday rotations and giant magneto-resistance (Dietl and Ohno, 2014; Pradhan and Das, 2017a; Tsymbal and Igor Zutic Nasirpouri, 2013; Majorana and Zichichi, 1991; Tanaka, 2020). These materials can be formed by doping host II-VI, III-V, and other type semiconductors (like ZnSe, ZnTe, GaAs, InP, CdTe, InAs, ZnO, TiO_2, etc.) with magnetic transition metals such as V, Co, Cr, Mn, and Fe, etc., which are supposed to replace some cations in the host material (Gupta et al., 2020; Majorana and Zichichi, 1991; Tanaka, 2020). The concept of dilute magnetic semiconductors first emerged in the early 1980s, but the science of dilute magnetic semiconductors became well-known in the early 1990s. Some literature also claims that the discovery of Mn-doped GaAs is attributed to Hideo Ohno and Tomasz Dietel (Dietl and Ohno, 2014). In this regard, it should also be boldly raised that a famous compound of manganese-doped GaAs from III-V contributed to the discovery of dilute semiconductor material in 1988 by two American physicists, Nitin Samarth and Jacek K. Furdyna (Samarth and Furdyna, 1988). Soon after that, other dilute magnetic semiconductors consisting of Mn-doped II-VI alloys of the form $A_{(1-x)}Mn_xB$ (A = Hg, Zn, and B = Se, Te) were discovered by physicist Vitali Zakharchenya and his colleagues in the 1980s (Samarth and Furdyna, 1988). As a result, these material alloys are known to integrate two major fields of condensed matter physics: **semiconductors and magnetism**. These materials' principal applications include magneto-optical devices, optoelectronics, spin injection, quantum computing devices, solar cells (heat sensing), laser diodes, photo-detectors, gun diodes for microwave production, and so on (Dietl and Ohno, 2014).

Currently, understanding the origin of magnetism and impurities in DMS materials, controlling and manipulating magnetic properties, and exploring room-temperature DMS materials is challenging (Mekuye and Abera, 2023; Majid et al., 2023). In this case, the search for ferromagnetic semiconductor materials at room temperature is focused. Dependence of transport and optical properties on the magnetic state, and that the materials retain their fundamental semiconducting characteristics, i.e., strong sensitivity to doping, external fields, and light, and are compatible and integrated with conventional (non-magnetic) micro- and optoelectronic semiconductor technologies. Furthermore, these materials are seen as potential candidates for future spintronics devices, which enable the use of electron spin degrees of freedom in addition to charge degrees of freedom in information processing and data storage devices. This also opens the door to spintronics, a new growing discipline of electronics (Pradhan and Das, 2017a; Samarth and Furdyna,

1988; Tsymbal and Igor Zutic Nasirpouri, 2013; Tanaka, 2020).

Chalcognides (compounds and alloys of sulfur, selenium, and tellurium) exhibit an unusual range of physical phenomena, from intriguing electrical, thermal, and optical properties to unique types of superconductivity and magnetism (Ahluwalia, 2018; Kuan, 1995). Numerous properties and applications can be acquired when chalcogenides are combined with transition metals (such as Cd, Zn, Fe, Mg, Mn, etc.) to form transition metal chalcogenides. These substances have applications in many areas (Zaari et al., 2014a; Sharma et al., 2013; Guo et al., 2011). To list some of them, such as photovoltaic, lasers, diodes, visible light photo-detectors, nonlinear optical materials, magneto-optical devices, sensors, photo-converters, and other innovative devices (Ahluwalia, 2018; Kuan, 1995). Mainly, the current study is on transition metal chalcogenides such as ZnTe, ZnSe, and FeSe separately, as well as alloys of them. In this regard, zinc telluride is a binary chemical compound with the chemical formula ZnTe. This solid is a semiconductor material with a direct band gap of 2.26 eV (Mahi and Bouhafs, 2012). It is usually a p-type semiconductor inherently, but it can also be n-type based on dopants and other conditions (Adachi, 1999; Yang and Lu, 2000). Its crystal structure is cubic like that of sphalerite and diamond (Singh et al., 2018; Trujillo et al., 2012). Also, ZnSe has a similar crystal structure and space group as ZnTe, but its experimental band gaps can extend up to 2.8 eV.

The report of this work mainly focused on the electronic structure, phonon, magnetic properties, and superconductivity of the quaternary compound $Zn_{(1-x)}(Fe,V)_xSe_yTe_{(1-y)}$ and its fragments, which may be composed of chalcogenides of transition metal-doped materials of ZnTe, ZnSe, and FeSe. The material $Zn_{(1-x)}(Fe,V)_xSe_yTe_{(1-y)}$ is formed by replacing the iron atom with zinc and the telluride atom with selenide. So far, no computational or experimental investigations have been published on this material, despite its remarkable magnetic, superconducting, and nematic properties.

In addition to this, upon rearranging the values for x and y, we can get the different fragments of compound $Zn_{(1-x)}(Fe,V)_xSe_yTe_{(1-y)}$, for example, $Zn_{(1-x)}(Fe,V)_xSe$, and $Zn_{(1-x)}Fe_xTe$, which belong to the special class of magnetic compound called dilute magnetic semiconductor, which has plenty of technological applications (Ismayilova and Abbasov, 2021). For light iron atom doping, ZnTe and ZnSe are supposed to be used as light-emitting diodes, laser diodes, magnetic and spintronic devices, magneto-optical devices, etc. In these fragments, the former one is supposed to be both magnetic and superconducting for the lower Zn atom presence, while the latter one is magnetic but not superconducting.

Remarkably, compared to other traditional electronics, magnetic and spintronic devices are superior in terms of quick switching, high storage capacity, low power requirements, etc. However, in order to function, they require ferromagnetic materials that can be used at room temperature. Due to issues with the manufacturing of materials that are consistently doped, it is difficult to synthesize ferromagnetic magnetic materials. In this instance,

computational doping (substitution) methods will be used to explore the electrical and magnetic characteristics of $Zn_{(1-x)}(Fe,V)_xSe_yTe_{(1-y)}$ materials and their fragments.

Another issue in this report is the investigation of superconductivity in the quaternary compound $Zn_{(1-x)}(Fe,V)_xSe_{(1-y)}Te_y$ and in its fragments. Basically, superconductivity was first observed by Kamerlingh Onnes in 1911 while studying the behavior of mercury at liquid helium temperature. He observed that at 4.2 K, the resistance of mercury suddenly vanished (Sizoo and Onnes, 1925). This phenomenon of the disappearance of electrical resistance below a certain temperature is called superconductivity. The characteristic temperature at which the state comes into existence is called the critical or transition temperature (T_c) (P. and et al, 2014).

Re-arranging the values of x and y in the alloy (i.e., x = 1, y = 1), it can be turned into FeSe, which is among the classes of iron-based superconductors. The 11-type superconductors have been extensively studied to understand the mechanism of Fe-based superconductivity. The 11-type superconductor FeSe exhibits superconductivity with $T_c = 13K$ and its T_c reaches 37 K under high pressure (4−6 GPa) (David M Uhrig, 2019; Muratov et al., 2018). Thus, 11-type superconductors have the potential to achieve a high Tc. According to some reports, the T_C may extend if FeSe film, grown on a $BaTiO_3$ (BTO) substrate, is doped with Nb (with even larger values of the lattice constant $\sim 3.99A^o$). The highest critical temperatures in the iron-based superconductor family exist in thin films of FeSe, where a critical temperature above 100 K was reported in 2014 (Zargar and et.al, 2014). But, T_c enhancements, an invention of novel superconducting materials, mechanisms of superconductivity, and magnetic properties in iron-based superconductors remain challenging and still not well understood.

In this regard, the theoretical prediction of the superconductivity temperature of materials is challenging, especially those with high Tc superconductors. The conventional superconductivity with a low critical temperature can be predicted via BCS theory (usually $T_c < 30K$). That is, for those superconductors with weak electron-phonon couplings, their critical temperature can be predicted via the gap equation at zero temperature, i.e., $2\Delta_o = 3.53k_BT_c$. However, this theory fails to explain the cases of strong coupling, as it was derived based on the assumptions of weak electron coupling. Thus, investigation of the electronic structure, phonon, and superconducting characteristics of tetragonal FeSe will then be carried out using the electron-phonon wannier (EPW) concept of Migdal-Eliashberg formalism.

1.2. Statement of the Problem

Despite plenty of technological applications for magnetic superconducting materials, their critical temperature is still below room temperature. As a result, the search for novel superconductors remains a major scientific task today. For example, the applications of

high-temperature superconductors include induction heaters, transformers, fault current limiters, power storage, motors and generators, fusion reactors, quantum computing, magnetic levitation devices, and so on (Hosono et al., 2018). However, there are two main challenges in the experimental study of superconductivity and the realization of high T_c: i) searching for novel superconductors from among the enormous number of candidate compounds comprised of many elements, and ii) delineating the key physical parameters that control the superconductivity (like low temperature) through establishing a reliable multidimensional phase diagram. Thus, as a solution, recent developments recommend that machine learning and ab initio calculations should serve in the investigation of novel superconducting materials with higher critical temperatures. So in this study, one of the main focus areas is to study the $Zn_{(1-x)}(Fe,V)_xSe_yTe_{(1-y)}$ computationally (Nekrasov et al., 2016).

On the other hand, diluted magnetic semiconductors (DMSs) are promising materials for spintronics; however, to use their functional possibilities, the Curie temperature of the materials should be substantially above the room temperature (Chowdhury and Islam, 2018). Thus, the key challenge in dilute magnetic semiconductors is the ability to achieve both semiconductivity and ferromagnetism at room temperature. Many attempts have been made to improve the Tc of DMS by different techniques, but still, it remains to achieve room Tc since the maximum Tc achieved is still below 190 K for $Ga_{1-x}Mn_xAs$ despite their multifunctional applications at room temperature (Snider and et. al, 2020). The unique properties of iron-based superconductors originating from the multi-band electronic structure, strongly orbital-dependent phenomena, extremely small Fermi energy, electronic nematicity, and topological aspects give rise to many distinct and fascinating superconducting states. Specifically, iron selenide-based superconductors exhibit unique features such as isotropic superconductivity, magnetic field-induced superconductivity, electronic nematicity, and topological superconductivity (Böhmer and Kreisel, 2018; Ciechan and Winiarski, 2011; Lumsden and Christianson, 2010). However, the magnetic properties and mechanisms of superconductivity in iron-based superconductors are not well understood. Thus, in this research, the focus will be on the computational calculation and explanation of the magnetic and superconducting properties of $Zn_{(1-x)}Fe_xSe_yTe_{(1-y)}$.

At room temperature, $Zn_{(1-x)}Fe_xSe_yTe_{(1-y)}$ has its own application and properties. Thus, in this study, the one fragment, i.e., $Zn_{(1-x)}Fe_xSe$ thin films, will be synthesized by the chemical bath deposition method and characterized by different instruments to study its electronic properties.

1.3. Research Questions

The basic research questions that are to be answered upon the completion of this study are the following:

- How does iron doping in ZnSe affect the magnetic and electronic properties in $Zn_{(1-x)}Fe_xSe$?
- How do the iron and selenide co-doping affect the electronic and magnetic properties in $Zn_{(1-x)}Fe_xSe_yTe_{(1-y)}$ material?
- Is that possible to get the different magnetic properties by doping Vanadium than iron in $ZnSe$?
- How to deduce the isotropic properties of FeSe superconductor and theoretically enhance the superconductivity temperature and electron-phonon coupling constant?
- How do the iron concentration in $Zn_{(1-x)}Fe_x$ Se thin films affectes its structural and electronic properties?

1.4. Objective of the Study

1.4.1 General Objectives

The overall purpose of this study is to investigate the electronic structure, magnetic, and superconducting properties of $Zn_{1-x}(Fe,V)_xSe_yTe_{(1-y)}$ materials using computational and experimental methods.

1.4.2 Specific Objectives

The purpose of this research is to attain the following specific objectives:

- To compute the electronic structure, phonon, and magnetic properties of ternary compounds $Zn_{(1-x)}Fe_xSe$ (for x = 0, 0.0625, 0.125, 0.25, and 0.5) using GGA functional
- To analyze comparatively the electronic structure and magnetic properties of ternary compounds $Zn_{(1-x)}(Fe,V)_xSe$ (for x = 0, 0.083, 0.125, 0.25, and 0.5) using LDA functional
- To calculate the electronic structure, phonon, and magnetic properties of quaternary compounds, $Zn_{(1-x)}Fe_xSe_yTe_{(1-y)}$ (for x = 0, 0.125, 0.25, 0.5, and y=0, 0.0625, 0.125, 0.25)
- To calculate the superconducting properties such as electron-phonon coupling strength, superconducting gap, and Tc for $Zn_{(1-x)}Fe_xSe_yTe_{(1-y)}$ (for x = 1 and y = 1).
- To synthesize $Zn_{(1-x)}Fe_xSe$ on thin films by chemical bath deposition method for x = 0.01, 0.02, 0.03, and 0.04, to study the effect of iron doping on the electronic properties of ZnSe.

1.5. Scope of the Study

This study is limited to the experimental and computational study of compound $Zn_{(1-x)}(Fe,V)_xSe_yTe_{(1-y)}$ for values $0 \leq x,y \leq 1$. Electronic structure calculation is limited to the study of crystal structure, band structure, the projection density of states (PDOS), density of states (DOS), Fermi level (E_f), Fermi surface, magnetic properties, optical properties, and phonon density calculation. The calculation of electronic structure is done using the free quantum espresso code and electron-phonon wanner (EPW). Also, the experimental study will be employed for the study of the electronic structure, morphology, and crystal size of the thin films derived from the main compound with values of x and y as indicated above. In this case, the solution growth method is selected as there are different methods in this category that are easily accessible and economical methods for the preparation of chalcogenide thin films.

1.6. Organization of the Dissertation

This dissertation covers different properties of $Zn_{(1-x)}Fe_xSe_yTe_{(1-y)}$ alloy and its fragments, ZnSe (doped with Fe and V) and FeSe (doped with Zn). As a result of the structural analysis, the electronic, phonon, and magnetic properties are clearly investigated. This dissertation is organized so that it begins with a general introduction, goes through a review of related literature, materials, and methods, presents the results, and concludes with a summary and conclusions. The introduction (Chapter 1) focuses on the background, rationale, research questions, and objectives of the research, and it explains the overall structure of the dissertation. The literature review in Chapter 2, emphasizes applications as well as the sequential and coherent description of the backgrounds of the subjects of this study. And also the technological applications of materials under study, future prospects, and research directions of these materials, both computationally and experimentally. The basic principles of applying and the areas of applications of the results of this research (especially in magnetic and spintronics devices). In addition, it discusses all the theories underlying the research methodologies such as density functional theory, thin film synthesis by chemical bath deposition, and characterization techniques used in this dissertation. The correlational functional and pseudo-potentials are briefly discussed. Chapter 3, provides a brief and detailed description of the methodologies (such as computational and experimental) used in this study. Also, all the materials used and procedures followed during the experimental work are explained in detail. Chapter 4, discusses the results and discussions obtained by the density functional theory approach for iron- and vanadium-doped ZnSe, Fe, and Se-co-doped ZnTe and FeSe systems by using different functional such as GGA, GGA+U, LDA, and LDA+U. Then it deals with the results of superconductivity properties of iron selenide using the EPW package. Finally, this chapter

presents, the results of experimental work, which are the structural and electronic properties of iron-doped zinc selenide thin films i.e. $Zn_{(1-x)}Fe_xSe$. It presents the major effects of iron doping on structural and electronic properties in ZnSe thin films that are synthesized by chemical bath deposition. Finally, Chapter 5, presents the summary, conclusion, and recommendations of future research work and interests in this area.

2. REVIEW OF RELATED LITERATURE

2.1. Transition Metal Doped Zinc Chalcognides

Transition metal chalcogenide compounds are formed from the unification of transition metals (such as Cd, Zn, Fe, Mg, Mn, etc.) with chalcogenides (O_2, S, Se, Te, and Po) (Robinson, 2020; Bechiri et al., 2009; Bechiri et al., 2009; Zhang et al., 2016). However, because of its technological importance, the term chalcogenide is most of the time associated with the compounds sulfur (S), selenium (Se), and tellurium (Te) (Kabita and Indrajit Sharma, 2017; Chowdhury and Islam, 2018). The scientific interest in BII-VI semiconductor materials is rapidly increasing due to the multitude of their applications in technology. These compounds exhibit applications in photovoltaic cells, lasers, diodes, visible light photo-detectors, nonlinear optical materials, magneto-optical devices, sensors, photo-converters, luminescence devices, and other optical devices (Bechiri et al., 2009; Zhang et al., 2016; Kabita and Indrajit Sharma, 2017).

Zinc selenide is one of the earliest found BII-VI semiconductors with a wide, direct bandgap averaging (2.5–2.9 eV) at room temperature with the space group F-43m (Bechiri et al., 2009; Kabita and Indrajit Sharma, 2017). Since zinc and selenium belong to groups II and VI, respectively, of the periodic table, they are referred to as a category of BII-VI semiconductor compounds. Due to its wide band gap, strong electronic transport capabilities, high refractive index, big exciton binding energy (21 meV), high refractive index, and great optical transparency over a broad range in the visible spectrum, it is a suitable material for the application (Mahmood et al., 2020; Chowdhury and Islam, 2018; Sharma et al., 2013; Behloul et al., 2016; Gavrichev et al., 2002; Basak et al., 2012). It crystallizes with cubic zinc-blende (ZB)(with lattice parameter a = 5.668 $\mathring{A}$) and the hexagonal wurtzite (WZ) structure(with a = 3.820 $\mathring{A}$ and c = 6.628 $\mathring{A}$) (Bechiri et al., 2009; Wang et al., 2016a). The third-nearest neighbor atomic arrangement is the only difference between the ZB and WZ structures; hence, their electrical characteristics behave similarly except the difference in their band gap is 0.05 eV ($E_g^{WZ} > E_g^{ZB}$) (Wang et al., 2016a; Yu et al., 2014). In this case, we consider only the cubic zinc blended structure, with the Zn atoms occupying the edges and face positions while the Se atoms allow the crystal to form an interpenetrating face-centered cubic (Yu et al., 2014; Xie et al., 2014). Its unit cell contains four molecules with Zn at the Wyckoff position of 4a $(0,0,0)$ and Se at 4d $(\frac{3}{4},\frac{3}{4},\frac{3}{4})$ respectively as shown in Figure 8. For this matter, it is also among the most investigated semiconductors, either computationally or experimentally (Sharma et al., 2018).

Undoped zinc selenide compounds are nonmagnetic, and it is impossible to get the desired properties for spintronics and magneto-optics applications in an undoped one. When it is doped with transition magnetic metals such as Fe, Mn, Co, etc., it gives rise to

novel properties, usually called dilute magnetic semiconductors (Yu et al., 2014; Xie et al., 2014; Benstaali et al., 2013; Faschinger et al., 1994a; Mahmood et al., 2016; Kumar and Singh, 2011). They are a class of semiconductors that can display normal electrical and magnetic properties, as well as novel ones such as large Faraday rotations and giant magneto-resistance (Su and Wang, 2010; Adetunji et al., 2012). These semiconductors are attractive materials in the science and potential technological applications of spin transport electronics (Su and Wang, 2010; Pradhan and Das, 2017b). Thus, the substitution of transition metals helps to get magnetic properties in it, in addition to the band modification of the material. Thus, the substitution of iron reduces the resistivity so that the conductivity of ZnSe is enhanced (Benstaali et al., 2013). In addition, active media and passive Q switches can be made from zinc selenide crystals doped with transition metal for use in biology, medicine, wave optics, and communications technologies (Nitsuk, 2014). Specifically, the reports indicate that efficient lasing is attained in the Fe: ZnSe system, and the V: ZnSe system can be used as passive Q switches (Nitsuk, 2014; Radevici et al., 2016). These materials' optical and magnetic properties make them excellent candidates for both applications in this sense. However, in-depth research is still needed since it can reveal fundamental features that are applicable to magneto-optics, magneto-electronics, and spintronics devices. The experimental study was performed on Fe-doped ZnSe, and the spin glass behavior was observed below the temperature of 45K (Laiho et al., 2010). The other group confirmed that ferromagnetic stabilization can occur for concentrations below 5% of iron in ZnSe as a result of LDA approximation. The other experimental group reported that vanadium-doped ZnSe that had been created under epitaxial growth conditions showed ferromagnetic properties at room temperature (Tahashi et al., 2009). In addition, it is possible to use this material as a suitable material for magnetic devices based on further experimental investigations with the lowest possible iron substitution in it.

In the present study, the structural and electronic properties as well as the magnetic properties of iron-doped ZnSe for different configurations using GGA and GGA+U are covered. The bandgap and lattice constant of ZnSe for these configurations well agrees with the previously reported theoretical results. To this end, the bandgap energy is underestimated as compared to experimental results due to exchange-correlation function problems in DFT calculations.

Also, despite its multi-functionality, the configuration-wise study of transition metal-doped ZnSe is inadequate. Hence, in this study, we focus on the structural, electronic, and magnetic properties of vanadium and iron-doped ZnSe for different configurations using LDA and LDA+U functionals. Moreover, the lattice vibration modes for pristine and doped zinc chalcogenides will be investigated in this case.

2.2. Zinc Telluride Semiconductor and Its Alloy with ZnSe

The chalcogenide compounds have been extensively studied due to their multi-functional properties in solid-state devices and other technological applications. Prominent applications of these compounds include light-emitting diodes (blue LED), semiconductor lasers, photovoltaic cells, microwave devices, non-linear optical materials, radiation detectors, visible light photodetectors, magneto-optical devices, and other optoelectronic applications (Singh et al., 2018; A.SArico, D. Silvestro, P.L.Antonucci and V.Antonucci, 1997; Isherwood et al., 2017; Younus et al., 2020; Zaari et al., 2014a). These chalcogenides are well known for their broad direct band gaps, which make them have novel optical and electrical behaviors. They remain a hot area of research. These chalcogenides typically crystallize in one of the following structures: zinc blende (face-centered cubic), wurtzite (hexagonal), or rock salt (simple cubic) crystal structures (Habura et al., 2023; Zaari et al., 2014a).

Zinc telluride (ZnTe) is a member of the II-VI family with a direct band gap of 2.26 eV at ambient conditions. As shown in Figure 1 (Jang et al., 2019), that of ZnSe is on average 2.7 eV. It is an essential semiconducting material for the development of various technological applications. Scientific interest in ZnTe has been increasing over time due to its promising applicability in diverse areas such as detectors (IR detectors, electro-optic field detectors), phosphors in X-ray imaging, thin-film transistors, laser diodes, and microwave devices (Singh et al., 2018; Rajpal and Kumar, 2018; Mondal et al., 1992). Furthermore, it has attracted attention for its high mobility semiconducting behavior and the exhibition of novel properties, such as magnetic and spintronics devices, upon doping with other magnetic elements. ZnTe has zinc blend cubic symmetry; its unit cell consists of four molecules, with Zn at the Wyckoff location of 4a (0, 0, 0) and Te at 4d ($\frac{1}{4}, \frac{1}{4}, \frac{1}{4}$). The space group for the zinc blende cubic ZnTe structure is F-43M (No: 216) (Mehmood et al., 2019; Guo et al., 2011).

Transition metal-doped ZnTe compounds are investigated for their novel properties in electrical and magnetic behaviors. The experimental study chromium-doped ZnTe shows that the band gap decreases (from 2.57 to 1.47 eV) with respect to the pristine compound (Sharma et al., 2013; Lungu et al., 2023). According to the study, ZnTe can exhibit magnetic properties when doped with transition elements magnetic atoms such as Mn, Fe, Co, and Ni at low concentrations (6.25%) (Mahmood et al., 2016). Mn results in semiconducting behavior, whereas Ni and Fe result in half-metallic behavior. The tuning of the ZnTe band gap by Fe, Co, and Ni doping has also been observed. According to the findings, pd-hybridization can be detected up to Fe, Co, or Ni doping in ZnTe, and the ferromagnetic semiconducting state can be exhibited by doping with these metals at lower concentrations (Zelai et al., 2022; Ismayilova and Abbasov, 2021; Shaaban et al., 2018). The experimental study on Cu: ZnTe shows that increasing Cu concentration induces a decrease in the band gap (Ochoa-Estrella et al., 2018). The addition of a magnetic transition

metal to zinc chalcogenides aids in the formation of unique magnetic qualities known as diluted magnetic materials, according to (Sato and Katayama-Yoshida, 2002). The study on the magnetic characteristics of Mn, V: ZnTe indicated that for low concentrations (through 6.25 % Mn and 12.5% V and fewer values), the system exhibits ferromagnetic features, but larger concentrations of Mn give rise to spin glass states (Guo et al., 2011). It also revealed that Mn- and V-doping produce semiconductor and half-metallic behavior in the material, respectively. Another study employing WIN2K found that low concentrations of Mn, Cr, and Ti doping in ZnTe can cause ferromagnetic behavior (Zaari et al., 2014b).

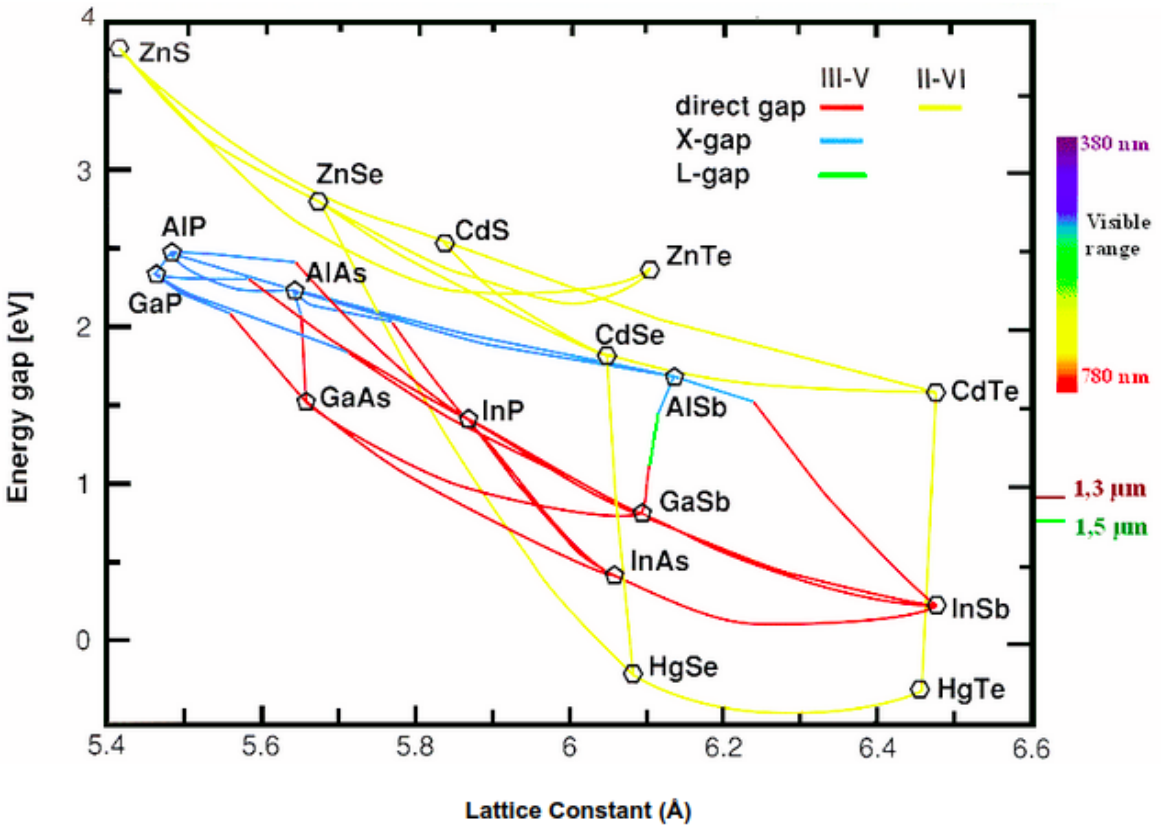

Figure 1: For semiconductors III-V and II-VI, the band gap energy is plotted against the lattice constant. Although the band gap of ZnSe is greater than that of ZnTe, the lattice constant of ZnTe is greater than that of ZnSe.

However, the alloy of ZnTe and ZnSe is of particular relevance in our research endeavor. The primary motive for the desire for this type of structure is that the alloy has many essential features, and unique properties, and the desire to further optimize for better and more customized applications. Some of the reasons include that alloys can achieve a tunability band gap by adjusting compositions, which is not achievable in pure ZnSe and ZnTe. As a result of the variable band gaps, the material is suited for a wide range of optical and solar cell applications. It also improves the material's stability (chemical and mechanical), which is beneficial in obtaining an efficient optical property. Alloying also greatly improves the difference in lattice constants between two pristine compounds. When

compared to individual molecules, it may also lessen undesirable processes and features (reduce non-radiative recombination).

Despite its new features and several technological uses, $ZnSe_yTe_{(1-y)}$ has received little attention and has a scarcity of literature, particularly when it is further doped with transition metal magnetic atoms such as iron. In addition, the configuration-wise doping of magnetic atoms in this ternary alloy makes it a quaternary complex while disclosing its structural, vibrational, and magnetic properties when doped with iron instead of zinc. That is the doping of Fe and Se in a cubic ZnTe to form the structure called a quaternary alloy, which consists of four elements: Zn, Fe, Se, and Te. It is an inorganic material that may also be supposed to be formed from ZnTe, ZnSe, and FeSe with interesting magnetic, electronic, and optical properties depending on the concentrations (x and y). It is supposed to be applicable to spintronics, thermoelectrics, and novel electronic materials. Thus, in this study, we will look at the electronic structure, lattice vibration, and magnetic characteristics of $ZnSe_yTe_{(1-y)}$ when iron atoms are doped instead of zinc atoms in different configurations.

2.3. Magnetism in Solids

The magnetic properties of materials arose from the spin of electrons and their orbital motion, and magnetism properties are regulated by the electronic arrangement inside atoms and the crystal structure of the material (Mermin and N.David, 1976). The different types of magnetic ordering with different magnetic characteristic is presented as a result of electron organization and exchange interaction, as shown in Figure 2. As a result, the magnetism of materials can be classified as paramagnetism, diamagnetism, ferromagnetism, ferrimagnetism, antiferromagnetism, helimagnetism, and so on, as illustrated in the diagram (Zhang, 2014). Semiconducting materials having a modest number of magnetic impurities (such as transition metals) that allow them to have both semiconducting and/or magnetic properties are of particular relevance in this scenario. Dilute magnetic semiconductors are the name given to this class of materials. This type of material could be used in magnetic and spintronics devices such as magnetic refrigerators, magnetic sensors, magnetic water treatment, magnetic energy storage, quantum computing, spin valves, magnetic tunneling junctions, spin transistors, spin torque oscillators, spin-hall effect devices, spin Seebeck effect devices, spin filters, etc.(You et al., 2023). Some of the common dilute magnetic materials include transition metal-doped III-V semiconductors (such as GaMnAs, GaMnN, GaMnP, InMnAs, InMnSb, GaCrN, and GaFeN), transition metal-doped II-VI semiconductors (ZnMnSe, ZnMnSe, CdMnTe, HgMnTe, etc), rare earth-doped semiconductors (such as GaGdN, GaEuN, etc.) and oxide base DMS ($Zn_{(1-x)}M_xO$ (M = Fe, Mn, V, Co), $TiCoO_2$, etc). However, it is still of scientific interest to achieve stable ferromagnetic materials at high temperatures (You et al., 2020; Slade et al., 2023). Transition metals (in this case, V and Fe)-doped ZnSe and ZnTe systems are of this kind of

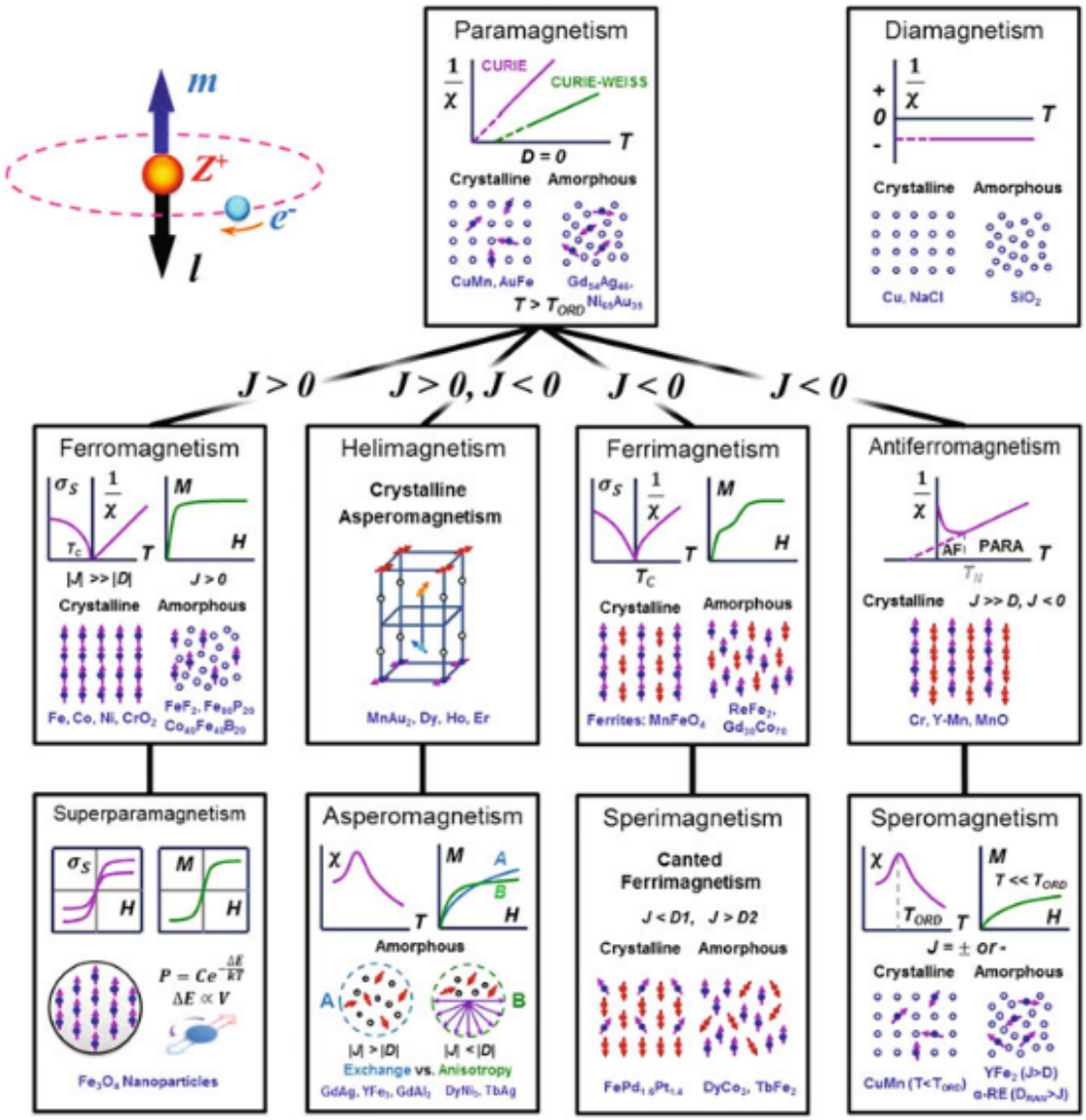

Figure 2: The classification and properties of magnetism of materials

interest in this research.

2.4. Critical Temperature Approximation in Ferromagnetism

In the Heisenberg model of mean-field theory (MFA), the disparity in total magnetic energy is a key factor in defining the critical temperature of magnetic systems (Sadique and Shahjahan, 2018). In the Heisenberg model, the Hamiltonian for an interacting spin-spin system in an applied magnetic field is given by (Alsaad, 2009; Search et al., 2003; Coey, 2008):

$$H = H_{ex} + H_z = -\sum_{ij} J_{ij} S_i . S_j + g\mu_B s_i . B, \tag{2.1}$$

where J_{ij} is the exchange coupling constant of magnetic atoms at sites i and j (if $J_{ij} > 0$ it is a ferromagnetic system and J_{ij}<0 it is antiferromagnetic exchange interaction in the system), and $S_i(S_j)$ is the spin at site i(j). The value of the $S_i.S_j$ will take the values between $-s^2$ and s^2. Since $J_{ij} = J_{ji}$ up on interchanging the sites i and j, And exchange interaction (H_{ex}), the interaction energy of the neighboring spins and the Zeeman Hamiltonian (H_z), the energy of the spins in the magnetic system with an effective magnetic field (B).

The Heisenberg model takes its most common form by accounting the each pair of the spins one (factor 2 indicates that the summation includes each pair of electrons twice and $i > j$ avoids the double counting).

$$H_{ex} = -2\sum_{i>j} J_{ij} S_i.S_j, \tag{2.2}$$

The Zeeman Hamiltonian (H_z), the energy of the spins in the magnetic system with an effective molecular magnetic field (B_f) at the i^{th} spin site can be given by

$$H_z = g\mu_B s_i B_f \tag{2.3}$$

where μ_B is the Bohr magneton and g is the Lande g factor. Now considering there is no angular momentum and defining the effective molecular magnetic field at the i^{th} spin position can be obtained from this condition by equating H=0,

$$B_f = -\frac{2}{g\mu_B}\sum_j J_{ij} s_j, \tag{2.4}$$

According to the Weiss classical molecular field of a molecule, the internal magnetic field of molecular ferromagnetic material (B_f) is proportional to the magnetization (M).

$$B_f = n_w M, \tag{2.5}$$

where n_w is the parameter which strength of the molecular field. In the presence of the applied magnetic field, the net field acting on the given dipole is given by

$$B = B_{ex} + n_w M, \tag{2.6}$$

If all the atoms in the solid have a total angular momentum of j, the total magnetization as a function of temperature for the specimen is given by

$$M(T) = Ng\mu_B j B_j^{'}(x), \tag{2.7}$$

Where,

$$x^{'} = \frac{jg\mu_B B}{k_B T}, \tag{2.8}$$

where, k_B is a Boltzmann constant and the function called the Brillouin function is given by

$$B_j^{'}(x^{'}) = \frac{2j+1}{2j}\coth\frac{2j+1}{2j}x^{'} - \frac{1}{2j}\coth\frac{x^{'}}{2j}, \tag{2.9}$$

N is the number of atoms per unit volume. Thus for the ferromagnetic system, the total magnetic field can be placed in the equation (2.8) which gives

$$x^{'} = \frac{jg\mu_B}{k_BT}[B_{ex} + n_wM], \tag{2.10}$$

If we consider spontaneous magnetization, the external field will be zero, B_{ex} = 0, and then from equation (2.11) and (2.10) respectively, the reduced magnetization will be

$$\frac{M(T)}{M(0)} = B_j^{'}(x^{'}), \tag{2.11}$$

and

$$\frac{M(T)}{M(0)} = \frac{k_BT}{Nn_wg^2\mu_B^2j^2}x^{'}, \tag{2.12}$$

where M(0) = $Ng\mu_Bj$ and for the small value of $x^{'}$, the Brillouin function can expand to

$$B_j^{'}(x^{'}) = \frac{j+1}{3j}x^{'} - \frac{j+1}{3j}\frac{2j^2+2j+1}{30j^2}x^{'3}, \tag{2.13}$$

This implies that for the small value of $x^{'}$ ($x^{'} \ll 1$)

$$B_j^{'}(x^{'}) = \frac{j+1}{3j}x^{'}, \tag{2.14}$$

Inserting equation (2.14) to (2.11), the temperature-dependent magnetization is given by

$$M(T) \approx \frac{N\mu_B^2g^2j(j+1)}{3k_BT}B, \tag{2.15}$$

Now, the molar magnetic susceptibility is given by

$$\chi = \frac{M(T)}{B} = \frac{N\mu_B^2g^2j(j+1)}{3k_BT}, \tag{2.16}$$

Then susceptibility follows the Curie law.

$$\chi = \frac{C}{T}, \tag{2.17}$$

where, the Curie constant, $C = \frac{N\mu_B^2g^2j(j+1)}{3k_B}$.

Considering the condition for the external magnetic field, B_{ex}, we have

$$M(T) \approx \frac{N\mu_B^2 g^2 j(j+1)}{3k_B T}[B_{ex} + n_w M], \tag{2.18}$$

Rearranging this equation, the susceptibility can be written as

$$\chi = \frac{M(T)}{B_{ex}} = \frac{C}{T-\theta}, \tag{2.19}$$

Where $\theta = n_w C$ is the Curie-Weiss temperature. On the other hand, from the quantum concept of mean field approximation, thermal energy can be expressed as

$$k_B T_c = \frac{2\hbar^2 J_0 j(j+1)}{3}, \tag{2.20}$$

Where J_0 is the exchange coupling constant. In this case, the exchange coupling term, $J_0 \approx \hbar^2 J_0 j(j+1)$ (i.e., if term $j(j+1)$ is included in J_0) can be expressed in terms of total energy difference and dopant concentration (Wolfgang Nolting · Anupuru Ramakanth, 2020).

$$J_0 = \frac{\Delta E}{N_{imp}}, \tag{2.21}$$

where $\Delta E = E_{FM} - E_{AFM}$ is the difference between the total magnetic energies of ferromagnetic and antiferromagnetic states and N_{imp} is the number of transition metal dopants in the supercell. The transition temperature (Curie/Neel) can be calculated using the Mean-Field Approximation (MFA) theory based on the energy difference between the ferromagnetic and antiferromagnetic states of the systems.

$$\frac{3}{2} k_B T_c^{MFA} = \frac{\Delta E}{N_{imp}}, \tag{2.22}$$

Where k_B is the Boltzmann's constant, N_{imp} is the total number of dopants in each configuration, and T_c is the mean-field approximation of Curie temperature.

2.5. Application of Dilute Magnetic Materials

Dilute magnetic materials are among the best candidates for magnetic and spintronics devices and they often include, semiconductors, alloys, and oxides (Žutić et al., 2004; Liu et al., 2019). Others include ferromagnetic materials and topological insulators, such as Bi_2Se_3, which have high spin polarization, extended spin lifetimes, and high magnetic moments. Materials with strong spin-orbit couplings, including platinum and heavy metals, were recognized as having an intriguing application in spintronics devices. Currently, it has been determined that ferromagnetic materials are the most practical for use in magnetic and spintronics devices. This is the result of both the magnetic characteristics' durability when

subjected to external magnetic fields and the persistent alignment of the electron magnetic moments in a specific direction. These devices are widely used in cutting-edge fields like electronics, safety, security, medical, energy, transportation, and other advanced domains. They are also used in data processing and storage. The applications of magnetic and spintronics devices, however, are the main emphasis of this study. Depending on the material characteristics and level of doping, the dilute magnetic material may exhibit metallic behavior or semiconductor. GaMnAs is an example of a diluted magnetic material with a band gap that may be suggested for use in spintronics devices. Fe: ZnO, on the other hand, may not have a band gap that can be recommended for applications in magnetic devices.

2.5.1 Magnetic Devices

These devices belong to a class of electronic equipment whose operation is based on classical magnetism, which entails the interaction of magnetic fields with moving charges (Li and Yang, 2016a). This interaction enables the devices to carry out many tasks, including the storing, processing, and transmission of information. In order to store and manipulate information, it therefore works with magnetizable materials and takes advantage of such materials' magnetic properties. Magnetic devices include, for instance, hard disk drives, magnetic sensors, magnetic tape, and magnetic memory chips.

2.5.2 Spintronics Devices

Based on electronic properties (such as Fermi level position in the density of spin-polarized channels), the spintronic materials are usually classified into magnetic metals, topological materials, and magnetic semiconductors as demonstrated in Figure 3(Li and Yang, 2016b). Similar to magnetic devices, these are the kinds of electrical gadgets that employ magnetic fields to control how electrons behave. On the other hand, its operating mechanism sets it apart from magnetic devices (Li and Yang, 2016a). The underlying quantum physics that governs electron spin is the basis for how spintronics devices function. In place of its charge, it operates by using both the magnetic field and the spin of electrons. A binary value can be represented by the electron's spin, which can be either up or down (Fusil et al., 2014). It is conceivable to employ these devices for effective and quick data processing and storage applications by manipulating the electron's spin. Spintronics devices include, for instance, spin valves, magnetic tunnel junctions, spin transistors, etc.

For use in magnetic and spintronics devices, all diluted magnetic materials with a higher Curie temperature, higher magnetic moments, good electrical conductivity, improved thermal stability, and low coercivity are often acceptable. There are many benefits to these magnetic and spintronics systems over traditional electronics. Low power consumption, quicker switching rates, larger storage capacity, non-volatility, and better performance are

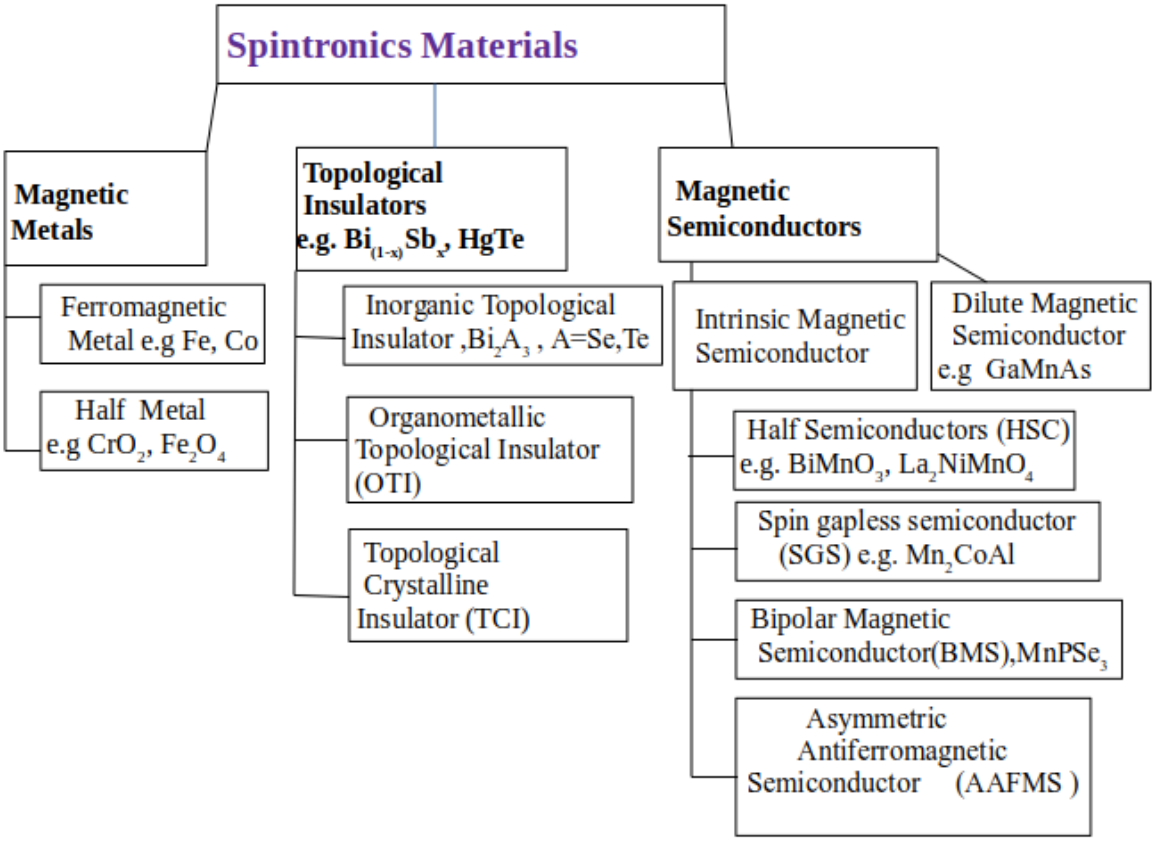

Figure 3: The classification of spintronics materials

some of the benefits. Dilute magnetic semiconductors dilute magnetic alloys, and dilute magnetic oxides, however, might be challenging to make or generate. The difficulties include managing doping concentrations, achieving uniform magnetic impurity distribution, complex (efficient and scalable) synthesis methods, comprehending the mechanism underlying ferromagnetism, high-temperature stability, and finding new materials with novel properties.

2.6. Density Functional Theory (DFT)

Density Functional Theory (DFT) is a quantum mechanical method used in physics, chemistry, and material science to investigate and calculate the physical properties of atoms, molecules, and solids (Dixon, 2016; Stanton, 2001). In general, it deals with many different situations: spin-polarized systems, multi-component systems such as nuclei and electron-hole droplets, free energy at finite temperatures, superconductors with electronic pairing mechanisms, relativistic electrons, time-dependent phenomena and excited states, bosons, molecular dynamics, etc. It was not considered an accurate rate method for the calculation of quantum physics until the 1990s. In 1998, Walter Kohn was awarded the Nobel Prize in Chemistry for his development of the density functional theory(Piela, 2020; Kohn and Sham, 1965).

2.6.1 The Born-Oppenheimer Approximation

The time- and position-dependent representation of the non-relativist Schrodinger equation of the nuclei of the electron system is given by (Koch and Holthausen, 2015)

$$\hat{i}\hbar\frac{\partial\Phi(R_\mu,r_i;t)}{\partial t}=\left[-\sum_\mu\frac{\hbar^2}{2M_\mu}\nabla^2_{R_\mu}-\frac{\hbar^2}{2m}\sum_i\nabla^2_{r_i}+V(R_\mu,r_i)\right]\Phi(R_\mu,r_i;t), \tag{2.23}$$

Where,

$$V(R_\mu,r_i)=V_{e-e}+V_{n-n}+V_{e-n} \tag{2.24}$$

$$=\sum_{i,\mu}\frac{Z_Ie^2}{|r_i-R_\mu|}+\frac{1}{2}\sum_{i\neq j}\frac{e^2}{|r_i-r_j|}+\sum_{\mu\neq\nu}\frac{Z_\mu Z_\nu e^2}{|R_\mu-R_\nu|}, \tag{2.25}$$

Here, $r_i=(r_1,r_2,...r_i)$ (electron position) and $R_\mu=(R_1,R_2,...R_i)$ (nuclei position). In shorthand notation, we can write equation (2.25) as

$$\Big(T_n+T_e+V_{e-e}+V_{n-n}+V_{e-n}\Big)\Phi(R_\mu,r;t)=E_n\Phi(R_\mu,r_i;t) \tag{2.26}$$

The Born-Oppenheimer approximation assumes that because nuclei are substantially heavier than electrons (i.e M≫m, for example, the proton (1H), weighs roughly 1800 times more than an electron, and for a typical nucleus such as carbon, the mass ratio well exceeds 20,000), the response of electrons to an external perturbation is much faster than that of nuclei (Stanton, 2001). As a result, the kinetic energy, T_n, is set to zero, and the repulsion term for nuclei, V_{n-n}, enters the total energy as a constant, and the electronic Schrödinger equation is solved using this first approximation.

$$\Big(-\frac{\hbar^2}{2m}\sum_i\nabla^2_{r_i}+V(R_\mu,r_i)\Big)\Psi_{R_\mu}(r)=E(R_\mu)\Psi_{R_\mu}(r) \tag{2.27}$$

This is the famous Born-Oppenheimer approximation or clamped-nuclei approximation.

2.6.2 Hohenberg-Kohn Theorem

The original theorem of Hohenberg-Khon states that an exact representation of the ground state properties of a stationary, non-relativistic many-particle system in terms of the exact ground state density is possible (Martin, 2020; Kohn and Sham, 1965). This is the basis of Density Functional Theory (DFT). The ground-state charge density for N electrons is given by

$$n(r)=N\int|\Psi(r,r_2...r_N)|^2dr_2....dr_N, \tag{2.28}$$

The two theorems are:

Part I. There is a unique potential $V(R,r)$ having n(r) as ground state charge density. Thus, the state energy of the electronic system can be written as a function of the density of electrons.

$$E[n(r)] = F[n(r)] + \int n(r)V(r)dr, \tag{2.29}$$

where $F[n(r)]$ is a universal functional and $V(r)$ is an external nuclear potential and given by

$$V(r) = \frac{Z_\mu e^2}{|r_i - R_\mu|}, \tag{2.30}$$

Part II. A universal functional for the energy, E[n(r)], in terms of the density, n(r), can be defined and valid for any external potential, V(r). The exact ground-state energy of the system is the global minimum of this function and the density that minimizes the functional is the exact ground-state density, $n_o(r)$.

$$E(r) = min_n[F[n(r)] + \int n(r)V(r)dr] \geq E_o, \tag{2.31}$$

Where, $F[n(r)] = \hat{T}_s + \hat{V}_{ee}$, $\hat{T}_s$ is a kinetic energy operator and $\hat{V}_{ee}$ is a potential energy. This indicates that the total energy reaches its minimum if the electron density of the system is the ground electron density (Stanton, 2001). So how do we know that a given density of the electron is a ground electron density? So this question takes us to the Khon-Sham theorem, which is discussed in the following section.

2.6.3 The Khon-Sham Method Equation

Kohn-Sham equation incorporates the correlation of electrons in addition to exchange energy for the non-interacting electron system(Chu and Leung, 2001)

$$E(r) = F_{HK}[n(r)] + \int n(r)V(r)dr \tag{2.32}$$

$$= T_s[n(r)] + E_H[n(r)] + \int n(r)V(r)dr + E_{exc}[n(r)], \tag{2.33}$$

where, $T_s[n(r)]$ is the kinetic energy of the non-interacting system.

$$T_s[n(r)] = -\frac{\hbar^2}{2m}\sum_\mu \int \psi^*(r)\nabla^2\psi(r)dr$$

$$n(r) = \sum_i |\psi_i(r)|^2$$

$$\langle \psi_i(r)|\psi_j(r)\rangle = \delta_{ij},$$

$E_{exc}[n(r)]$ is the exchange-correlation energy (reminiscence in Hartree) but includes all remaining unknown terms. The minimization of energy in equation (2.33) with respect to $\psi_i(r)$ gives the Kohn-Sham equations (Jung et al., 2006).

$$[-\frac{\hbar^2}{2m}\nabla^2 + V_r(r) + V_H(r) + V_{exc}(r)]\psi_i(r) = \varepsilon_i\psi_i(r) \tag{2.34}$$

$$[-\frac{\hbar^2}{2m}\nabla^2 + V_{eff}(r)]\psi_i(r) = \varepsilon_i\psi_i(r) \tag{2.35}$$

where, $V_{eff}(r) = V_r(r) + V_H[n(r)] + V_{xc}[n(r)]$.

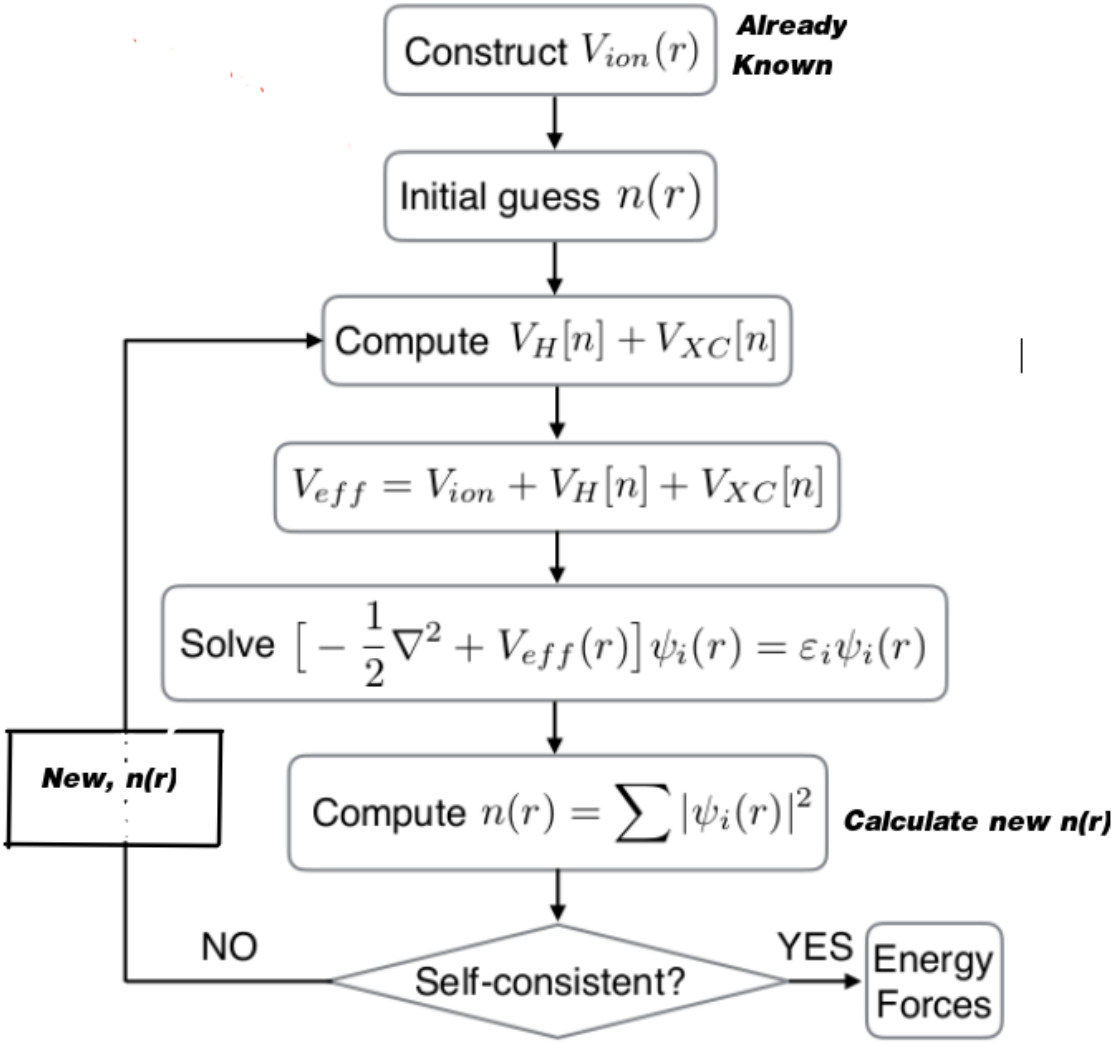

Figure 4: Schematic diagram showing of Khon-Sham equation solving algorithm

The major usual algorithm employed in a quantum espresso package is as indicated in Figure 4

2.7. Exchange Correlational Functions

2.7.1 Local Density Approximation (LDA)

The local density approximation (LDA) is the basis of all approximate exchange-correlation functionals (Perdew and Zunger, 1981; Piela, 2020). At the center of this model is the idea of a uniform electron gas. This is a system in which electrons move on a positive background charge distribution such that the total ensemble is neutral.

$$E_{exc} = \int n(r)\varepsilon_{xc}(n(r))dr. \tag{2.36}$$

Here, $\varepsilon_{xc}(n(r))$ is the exchange correlational energy of a uniform electron gas with density $n(r)$. It can be of two parts: exchange energy, ε_x and correlation energy, ε_c

$$\varepsilon_{xc}(n(r)) = \varepsilon_x(n(r)) + \varepsilon_c(n(r)). \tag{2.37}$$

The exchange of an electron in a uniform gas is

$$\varepsilon_x(n(r)) = -\frac{3}{4}\left(\frac{3n(r)}{\pi}\right)^{\frac{1}{3}} \tag{2.38}$$

Whereas there is no known expression for correlation energy, ε_c part.

2.7.2 General Gradient Approximation (GGA)

These are a category of functionals that consider the local density and local gradient of the electron density (Jung et al., 2006)

$$E_{exc} = \int n(r)\varepsilon_{GGA}(n(r)|\nabla n(r)|)dr. \tag{2.39}$$

There are different types of pseudo-potentials with a GGA correlational functional that can create slightly different results during calculations.

2.8. Pseudo-potentials

Pseudo-potentials are effective potentials that simplify electronic structure calculations in DFT packages by replacing the complex interaction of core electrons and atomic nuclei (Martin, 2020). There are various forms of pseudo-potentials that are used to facilitate electronic computations in DFT systems. Some of these are norm conservative (NC), ultrasoft (USSP), and projector augmented wave (PAW), each with its own set of benefits, drawbacks, limitations, and computing efficiencies. Ultrasoft pseudo-potentials (USSP) can be made smoother with less transferability than normal conservative pseudo-potentials. As a

result, it uses a smaller plane wave basis for its representation, which reduces computational costs during calculations. This smoothness enables more efficient calculations in systems with strongly correlated (localized) orbitals, such as transition metals and heavy elements. Projector augmented wave (PAW) is likewise the most transferable and provides the best approximations to orbitals near the nucleus, but it is difficult to generate and not suitable for particular property computations. On the other hand, norm-conservative pseudo-potentials are transferable outside of a predetermined core radius, making them transferable in varied chemical environments (Martin, 2020). This is also useful for lowering computing costs simply by altering core radii. This is also simple to develop and apply. In this scenario, however, we will only consider ultrasoft pseudo-potentials for electronic structure calculations with GGA and LDA flavors, as well as semi-relativistic norm-conservative pseudo-potentials to consider some core radii in the calculation because PAW is not implemented in the electron-phonon wanner (EPW) version we are currently using.

2.9. Theoretical Basis of Lattice Vibration (Phonon)

In material science and solid state physics, phonon analysis is crucial because it can explain a wide range of properties, including mechanical properties, phase transitions, electrical conductivity, Debye temperatures, specific heats, electron-phonon coupling (a property of superconductivity), and more (Yu et al., 2014; Tanaka, 2020). The frequency of phonon (lattice vibrations) as a function of wave vector or momentum along multiple high symmetry directions in the Brillouin zone is given by phonon dispersion(Togo and Tanaka, 2015). It demonstrates how the energy of the typical modes of vibration varies when the wave vector changes. The dispersion relation can help identify important properties such as the presence of negative frequencies (which indicates the structure's dynamical instability), anharmonic effects on vibrations (observable in the curvature of the branches), and the speed of sound in materials, which is proportional to the slope of the dispersion relation's acoustic branches. Whereas the phonon density of states depicts the distribution of vibration states (normalized per unit volume and energy) across different frequencies. It demonstrates how many vibrational states exist at a given energy and provides information on the contribution of various atomic species to these vibrations (Mermin and N.David, 1976). It is useful in analyzing the thermodynamic properties of materials such as specific heat capacity, thermal expansion, and thermal conductivity (Basak et al., 2012; Togo and Tanaka, 2015). Furthermore, it aids in determining the presence of low-frequency or high-frequency modes, as well as their relative contributions to the material's overall qualities. In general, phonon analysis can provide valuable insights into vibrational characteristics, thermal and mechanical stability, and prospective applications such as thermoelectric materials, superconductors, or optoelectronic devices (Wang et al., 2016b; Challis, 1982).

If there are N atoms per unit cell, there are three acoustic and 3(N-1) optical phonon

modes (branches) of vibrations (Mermin and N.David, 1976). In lattice vibrations of acoustic branches the atoms are moving in phase and phonon dispersion exhibits zero frequency at the Brillouin zone center while in the case of optical branches, the atoms are moving out of phase, and phonon dispersion exhibits non-zero frequency at the Brillouin zone center.

Phonons are quantized lattice vibrations that play an important role in solid behavior, such as thermal conductivity, thermal expansion, electrical conductivity, and superconductivity (Tanaka, 2020). It is a unit of vibration energy that comes from oscillating atoms within a crystal and is also known as a phonon. They are Bosonic quasiparticles with a specific heat displaying a T^3 temperature dependence at low temperatures and saturating to a constant value at temperatures of the order of the Debye temperature (Mermin and N.David, 1976). Understanding the phonon of the material is thus useful for constructing a material with a distinct property such as thermoelectricity, superconductivity, etc.

Consider a crystal composed of an infinite number of unit cells in a space, and each of them is defined by three primitive translation vectors $\overrightarrow{a_1}$, $\overrightarrow{d}_2$ and $\overrightarrow{d}_3$. The position vector of the n^{th} unit cell relative to the origin is given by

$$\overrightarrow{r}_n = l\overrightarrow{a_1} + k\overrightarrow{d}_2 + h\overrightarrow{d}_3 \tag{2.40}$$

where l, k, and h are integers. If there are n atoms in the primitive cell that make up the basis, then the equilibrium position of the n^{th} atom relative to the others can be written as

$$\overrightarrow{r}_m = l\overrightarrow{a_1} + k\overrightarrow{d}_2 + h\overrightarrow{d}_3, \tag{2.41}$$

The relative position of those atoms relative to the origin is

$$\overrightarrow{r}_{nm} = \overrightarrow{r}_n + \overrightarrow{r}_m \tag{2.42}$$

As a result of thermal fluctuation, the atoms vibrate from their equilibrium position by an infinitesimal displacement, $\overrightarrow{u}_i$ (i = x,y,z), the actual position of atoms is

$$\overrightarrow{R}_{nm} = \overrightarrow{r}_{nm} + \overrightarrow{u}_i \tag{2.43}$$

The potential energy, V, in this case, can be assumed to be some function of the instantaneous position of all atoms.

$$V = V(...\overrightarrow{r}_{nm}, \overrightarrow{u}_i....), \tag{2.44}$$

where u_i is the displacement of the atom mn in the direction (i = x, y, z). Expanding the

potential in a Taylor series (Challis, 1982; Wang et al., 1994; Wang et al., 2016b)

$$V[u(R_{nm},t)] = V_o + \sum_i \sum_{R_m} \left(\frac{\partial V}{\partial u_i(R_m,t)} \right)_{eq} + \frac{1}{2} \sum_i \sum_j \sum_{R_n} \sum_{R_m} u_i(R_n,t) \left(\frac{\partial^2 V}{\partial u_i(R_n,t) \partial u_j(R_m,t)} \right)_{eq} u_j(R_m,t) + ... \tag{2.45}$$

We know that the force at equilibrium is zero and can be given in terms of potential.

$$F(R_m,t) = -\left(\frac{\partial V}{\partial u(R_m,t)} \right)_{eq} = 0. \tag{2.46}$$

By considering harmonic approximation (neglecting all terms in a cubic and higher order), we have

$$V(uR_m,t) = V_o + \frac{1}{2} \sum_i \sum_j \sum_{R_n} \sum_{R_m} u_i(R_n,t) \left(\frac{\partial^2 V}{\partial u_i(R_n,t) \partial u_j(R_m,t)} \right)_{eq} u_j(R_m,t). \tag{2.47}$$

Since V_o is the static potential energy of the crystal, independent of the displacement coordinates, we neglect it for the time being. And defining a harmonic matrix

$$D_{ij} = \left(\frac{\partial^2 V}{\partial u_i(R_n) \partial u_j(R_m)} \right)_{eq}. \tag{2.48}$$

Since the kinetic energy of a vibrating crystal is

$$T[\dot{u}_i(R_n)] = \frac{1}{2} \sum_{R_n} M_i \dot{u}_i^2(R_n). \tag{2.49}$$

Thus, the Hamiltonian function for the crystal in harmonic approximation is given by

$$H = \frac{1}{2} \sum_{R_n} M_i \dot{u}_i^2(R_n) + \frac{1}{2} \sum_i \sum_j \sum_{R_n} \sum_{R_m} u_i(R_n) D_{ij} u_j(R_m). \tag{2.50}$$

The equation of motion of atoms can be written using the second law of Newton.

$$M_i \omega^2 u_i(R_n) = \sum_j \sum_{R_m} D_{ij}(R_n,R_m) u_j(R_m). \tag{2.51}$$

Here, M is the nxn square mass matrix with the only diagonal element and $u_j(R_m)$ 1xn column matrix. Since Bloch's theorem is given by

$$u(R_n + R_m) = e^{ik.R_m} u(R_n) \tag{2.52}$$

It can be written as

$$u(R_n) = e^{ik.R_m} u(R_n) \tag{2.53}$$

Then the dynamical matrix is

$$\mathbf{D}(k) = \sum_{R_m} D(R_n, R_m) e^{ik(R_m - R_n)} = \sum_{R_p} D(R_p) e^{-ik.R_p} \tag{2.54}$$

Where, $R_p = R_n - R_m$. This gives the dynamical matrix of

$$\mathbf{D}(k) = \sum_{R_p} \left(\frac{\partial^2 V}{\partial u_i(R_n) \partial u_j(R_m)} \right)_{eq} e^{-ik.R_p} \tag{2.55}$$

The eigenvalues will be

$$M^{-1} D(k) \overrightarrow{\varepsilon} = \omega^2 \overrightarrow{\varepsilon} \tag{2.56}$$

Here, $\overrightarrow{\varepsilon}$ is a polarization vector of the phonon mode labeled by a set qj. From this, we can obtain the dispersion relation for phonon, which depends on the direction of k in the Brillouin zone.

$$\omega = \omega_\sigma(k). \tag{2.57}$$

The phonon density of states is defined by (Tanaka, 2020)

$$g(\omega) = \frac{1}{N} \sum_{kj} \delta(\omega - \omega_{qj}), \tag{2.58}$$

where N is the number of atoms per cell and $\omega_{(qj)}$ is the phonon frequency of the given mode labeled (q,j), q is the phonon wave vector, and j is the phonon band index.

2.10. Isotropic Superconductivity in FeSe

When examining the electric resistance of mercury at low temperatures in 1911, Dutch researcher Heike Kamerlingh Onnes made the first observation of superconductivity. He discovered that mercury's resistivity quickly plummeted to a value near zero, and it turned into a superconductor when the temperature was lowered below T_c = 4.2 K (Sizoo and Onnes, 1925). The search for new superconducting materials led to an increase in the highest known transition temperature, T_c over the decades. In 1987, a mixed oxide of lanthanium, barium, and copper $(La_{1.85}Ba_{0.15}CuO_4)$ with a T_c= 35 K) was discovered by Bednorz and Muller (Bednorz et al., 1987). In 2001, phonon-mediated superconductivity was observed in a MgB_2 with a T_c of 39 K (Nagamatsu et al., 2010). After seven years, iron-based superconductors were discovered in 2008, which are a family of phonon-mediated unconventional high-temperature superconductors next to cuprates. In this group of materials, the iron-based compound LaOFeAs (usually called iron pnictides) was first discovered with a T_c of 26 K (Sato et al., 2008) by Kamihara et al in 2008. Also, the findings in hydrogen sulfide systems raise hope for the prospects of achieving room-temperature superconductivity, which is in line with low-temperature scenarios like BCS theory. In this system, the critical temperature

ranges from 50 K to 235 K (Drozdov et al., 2015; Sato et al., 2008). And it may range up to 195 K at high hydrostatic pressures (141 Gpa) (Drozdov et al., 2015). However, in the history of superconductivity, the photo-chemically synthesized C-S-H system (a compound formed from a mixture of H_2S and CH_4 or hydrogen-rich compounds) becomes superconducting, with its highest critical temperature being T_c= 287.7 $\pm$ 1.2 K at 267 $\pm$ 10 GPa which was reported on October 15, 2020 (Snider and et. al, 2020).

Iron-based superconductors got more attention due to their intriguing properties and high flexibility concerning elemental substitution, leading to the formation of several families of iron-based superconductors. Also, they exhibit unique properties such as multi-band electronic structure, strongly orbital-dependent phenomena, extremely small Fermi energy, electronic nematicity, topological aspects, etc., which give rise to many distinct and fascinating superconducting states (Shibauchi and et.al, 2020). They provide a much wider variety of compounds for research, and they offer the hope of finally discovering the mechanism of room-temperature superconductivity and finding a way to increase Tc. They are also attractive for electrical power and magnetic applications because of their much higher Tc than cuprates and high isotropic critical currents, while the coexistence of magnetism and superconductivity makes them interesting for spintronics. These systems are frequently classified according to the stoichiometries of their parent compounds as 1111 (**RFeAsO**, R=La, Pr, Nd, Pr, Sm, Ce, Gd, Tb, Dy, etc), 122 (AFe_2As_2, and $A = B$ and also doping on the Fe site with Ni, Rh, Ir, and Pd), 111 (**LiFeAs**) and 11 (**FeSe**) systems (David M Uhrig, 2019; Zargar and et.al, 2014; Pustovit and et.al, 2016).

The superconductivity below 8 K in the iron chalcogenide compound was first discovered by Hsu and et.al (Coldea and Watson, 2018). Among iron-based superconductors, iron selenide (11) is the simplest iron-based superconductor. A number of its incarnations reveal several puzzling features that could be key milestones in understanding high-temperature superconductivity, and it hosts one of the richest physics. Superconductivity in FeSe is highly tunable, with the superconducting transition temperature, T_c, ranging from 8 K in bulk single crystals at ambient pressure to almost 4 0K under pressure or in intercalated systems. The combination of both intercalation and pressure results in re-emerging superconductivity at 48 K. The single-layer FeSe films on $SrTiO_3$(STO) substrate push the T_c to about 100 K and maybe even higher, opening a new frontier for superconductivity.

To this end, the prediction of the superconductivity temperature in materials is challenging in contemporary condensed matter physics. The BCS theory is a well-known theory to explain the superconductivity mechanism of conventional superconductors with low critical temperatures (usually $T_c < 30K$) and weak electron-phonon couplings, and it can basically predict the critical temperature from the superconductivity gap equation at zero temperature, i.e., $2\Delta_o = 3.53k_BT_c$. But this theory fails to explain the cases of strong coupling as it was derived based on the assumptions of weak electron coupling (Eliashberg, 1960).

In this work, we present the first principle calculations based on Migdal-Eliashberg formalism to investigate the isotropic superconductivity critical temperature of FeSe (Eliashberg, 1961; Liu et al., 2015; Si et al., 2016). FeSe is one of the known chalcogenide compounds with superconducting behavior. The FeSe has a tetrahedral crystal structure with experimental lattice parameters with values for a = 3.765 $\AA$ and c = 5.518 $\AA$ (Coldea and Watson, 2018). It can undergo a structural phase transition from tetragonal P4/nmm to weakly orthorhombic Cnmma unit cell at $T_s \approx 90K$ (Coldea and Watson, 2018).

For the calculation of the superconducting properties, the EPW (electron-phonon wannier) code is employed as integrated into the Quantum ESPRESSO package. The EPW (Electron-Phonon Coupling Using Wannier Functions) software is a Fortran90 code that employs maximally localized Wannier functions and density-functional perturbation theory to precisely and quickly calculate electron-phonon couplings and associated solid properties. EPW real space in combination with Kohn-Sham electronic eigenstates and phonon modes is provided by the quantum Espresso to calculate electron-phonon matrix elements. So it can give information on electron-phonon interaction self-energies, Fermi surface, electron-phonon spectral functions, Allen-Dyne critical temperatures, superconducting gap parameters, and other anisotropic and isotropic superconductivity parameters (Margine and Giustino, 2013; Margine et al., 2016; Ponci et al., 2016; Giustino et al., 2007).

2.11. Theory and Basic Equations Implemented in the EPW Package

Due to the weak electron-phonon coupling limit of the Bardeen-Cooper-Schrieffer (BCS) theory and Migdal-Eliashberg formalism for the superconducting state have now become the most successful descriptions of a vast amount of superconductors (Ponci et al., 2016; Villa-Cortés and Baquero, 2018; Migdal, 1958) . It is basically a generalization of BCS theory to account for the effects of retardation. The following anisotropic formulas must be calculated practically in order to analyze the superconducting characteristics of anisotropic superconductors like FeSe utilizing the Migdal-Eliashberg formalism (Eliashberg, 1961; Gerbi and Singh, 2019). Those basic anisotropic equations are already derived and the mass renormalization ($Z(\mathbf{k}, i\omega_n)$) and superconducting gap ($\Delta(\mathbf{k}, i\omega_n)$) functions are given by

$$Z(\mathbf{k}, i\omega_n) = 1 + \frac{\pi T}{N_F \omega_n} \sum_{\mathbf{k}', n'} \frac{\omega_{n'}}{\sqrt{\omega_{n'}^2 + \Delta^2(\mathbf{k}', i\omega_{n'})}} \lambda(\mathbf{k}, \mathbf{k}', n - n') \delta(\varepsilon_k), \tag{2.59}$$

$$Z(\mathbf{k}, i\omega_n)\Delta(\mathbf{k}, i\omega_n) = \frac{\pi T}{N_F} \sum_{\mathbf{k}', n'} \frac{\Delta(\mathbf{k}', i\omega_{n'})}{\sqrt{\omega_{n'}^2 + \Delta^2(\mathbf{k}', i\omega_{n'})}} \Big(\lambda(\mathbf{k}, \mathbf{k}', n - n') - N_F V(\mathbf{k} - \mathbf{k}') \Big) \delta(\varepsilon_k), \tag{2.60}$$

$$\lambda(\mathbf{k}, \mathbf{k}', n - n') = \int_0^\infty d\omega \frac{2\omega}{(\omega_n - \omega_{n'})^2 + \omega^2} \alpha^2 F(\mathbf{k}, \mathbf{k}' \omega), \tag{2.61}$$

where ω =(2n +1)πT (n is an integer) is a fermion Matsubara frequency, T is an absolute temperature, N_F is the density of states per spin at the Fermi level, $\lambda(\mathbf{k},\mathbf{k}^{'},n-n^{'})$ is an auxiliary anisotropic electron-phonon coupling and $V(\mathbf{k}-\mathbf{k})$ is the screened coulomb n potential between k and k$^{'}$ electronic states. The anisotropic Eliashberg electron-phonon spectral function is also given by

$$F(\mathbf{k},\mathbf{k}^{'}\omega) = N_F \sum_{v} |g_{kk,v}|^2 \delta(\omega - \omega_{\mathbf{k}-\mathbf{k}^{'},v}), \tag{2.62}$$

where $g_{kk,v}$ is first-order electron-phonon matrix element. The isotropic versions of Eliashberg's equations can be obtained by averaging k over the Fermi surface from equations (2.59) and (2.60)

$$Z(i\omega_n) = 1 + \frac{\pi T}{\omega_n} \sum_{n^{'}} \frac{\omega_{n^{'}}}{\sqrt{\omega_{n^{'}}^2 + \Delta^2(i\omega_{n^{'}})}} \lambda(\omega_n - \omega_{n^{'}}), \tag{2.63}$$

$$Z(i\omega_n)\Delta(i\omega_n) = \pi T \sum_{n^{'}} \frac{\Delta(i\omega_{n^{'}})}{\sqrt{\omega_{n^{'}}^2 + \Delta^2(i\omega_{n^{'}})}} \left(\lambda(\omega_n - \omega_{n^{'}}) - \mu_c^* \right), \tag{2.64}$$

Here, μ_c^* is the Coulomb interaction and given by

$$\mu_c^* = \frac{\mu_c}{1 + \mu_c \ln\left(\frac{E_F}{\omega_c}\right)}, \tag{2.65}$$

where, E_F is Fermi energy, ω_c is maximum cutoff frequency, and μ_c is a dimensionless parameter that describes the density of states at the Fermi level multiplied by the screened Coulomb interaction matrix element to produce the double Fermi surface average.

$$\mu_c = N_F \langle\langle V(\vec{k} - \vec{k^{'}}) \rangle\rangle_{FS}, \tag{2.66}$$

The value of μ_c ranges between 0.05 and 0.2.
In equations (2.63) and (2.64), the isotropic electron-phonon coupling strength, $\lambda(\omega_n)$ is given by(Migdal, 1958)

$$\lambda(\omega_n) = \int_0^\infty d\omega \alpha^2 F(\omega) \frac{2\omega}{\omega_n^2 - \omega^2}, \tag{2.67}$$

where, $\alpha^2 F(\omega)$ the isotropic Eliashberg spectral function and given by (Kanki and Yamada, 1993; Margine and Giustino, 2013)

$$\alpha^2 F(\omega) = \frac{1}{N_F} \sum_{nmv} \int \frac{d\mathbf{q}}{\Omega_{BZ}} \int \frac{d\mathbf{k}}{\Omega_{BZ}} |g_{nmv}(\mathbf{k},\mathbf{q})|^2 \times \delta(\omega - \omega_{\mathbf{q}v}) \delta(\varepsilon(n\mathbf{k}) - \varepsilon_F) \delta(\varepsilon_{m\mathbf{k}+\mathbf{q}} - \varepsilon_f). \tag{2.68}$$

The quasi-particle density of states in the superconducting state, which is employed to predict the presence of gaps in it, is given by (Choi et al., 2003)

$$\frac{N_s(\omega)}{N_F} = R_e\left(\frac{\omega}{\sqrt{\omega^2 - \Delta^2(\omega)}}\right). \tag{2.69}$$

The critical temperature, T_c for superconductivity can be estimated with the help of McMillan empirical formula (Allen and Mitrovi, 1983)

$$T_c = \frac{\omega_{log}}{1.2} exp\left[-\frac{1.04(1+\lambda)}{\lambda(1-0.62\mu_c^*)+\mu_c^*}\right],$$

where,

$$\omega_{log} = exp\left[\frac{2}{\lambda}\int \frac{d\omega}{\omega}\alpha^2 F(\omega)\log\omega\right].$$

The $\mu*$ is an empirical parameter that describes Coulomb screening, with typical values ranging from 0.1 to 0.16.

2.12. Thin Film Synthesis by Chemical Bath Deposition (CBD)

A thin film is a layer or layers of certain atoms with a thickness of nanometers to one micron formed by the condensation of atoms or molecules with unique properties that differ from whether they are thick particles with physical and engineering properties and the appropriate microstructures (Olayinka Oluwatosin Abegunde and Ude, 2019). The thicker layers above 1 micron are referred to as coatings or thick films, which are defined as small, dimensional substances created by a huge accumulation of granules, clusters, ion clusters, and molecular, and atomic types. Thin films, like other materials, have amorphous and polycrystalline structures depending on the preparation conditions and the material type. Thin films are made up of two parts: the layer and the substrate on which they are placed. Nowadays, most technologies are employed to reduce materials to nanosize and nano thickness, resulting in the creation of novel and unique properties of such materials in optical, electrical, optoelectronic, dielectric, and other applications.

A deposition process is regarded as a critical component in the development of thin-film novel materials to address the ever-increasing demand from industries for adaptable and multi-dynamic materials, according to (Olayinka Oluwatosin Abegunde and Ude, 2019). Thin film deposition is the process of generating and depositing thin film coatings onto a substrate material. The growth of film is found to be governed by various factors such as bath composition, pH, deposition time, and deposition temperature (Saha and et.al, 2020). There are different methods that can be used to synthesize thin films. Mainly, those methods of thin film deposition are classified into two categories: physical and chemical methods 5.

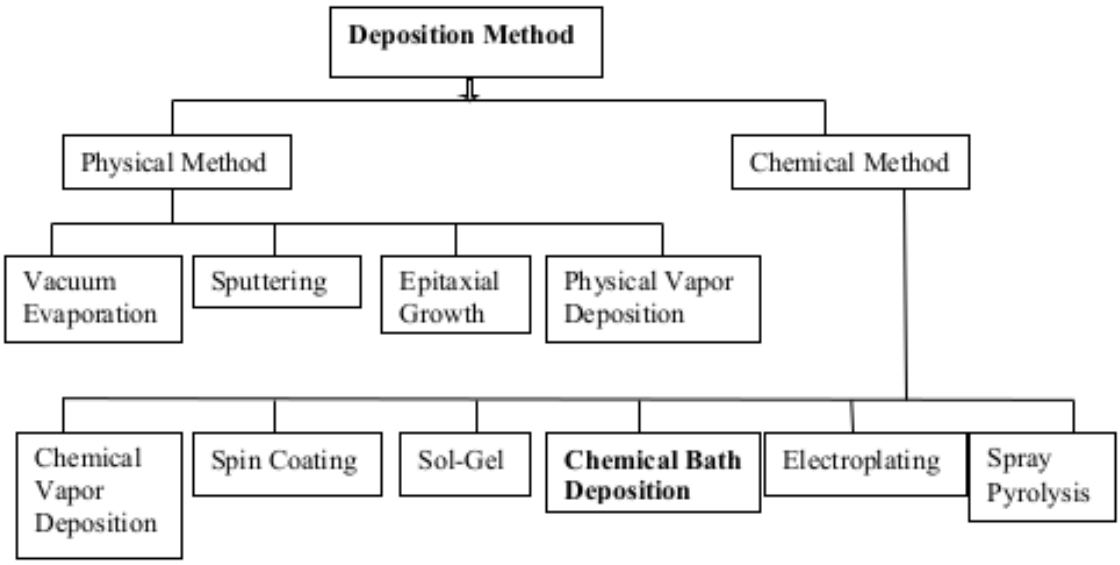

Figure 5: The classification of thin film deposition techniques

Furthermore, based on the methodology and techniques used, physical methods of thin film deposition can be classified as vacuum evaporation and sputtering. The vacuum evaporation method is a physical procedure in which material is evaporated in a vacuum chamber and condensed on a substrate to form a thin film. This technique includes resistivity heating, flash evaporation, electron beam evaporation, arc evaporation, and radio frequency (RF) heating. Sputtering, on the other hand, is the process by which energetic ions or inert gases are bombarded into the target solid material and then collide with the target material, dislodging the atoms or molecules from that target and condensing those atoms or molecules in the substrate to form a thin film. This process incorporates many techniques, such as glow discharge DC sputtering, triode, getter, radio frequency, magnetron, face target, ion beam, and alternate current (AC) sputtering.

Similarly, chemical methods of thin film synthesis can be divided into two types: gas phase and liquid phase (solution growth method). The gas phase is a technique that uses vapor phases and consists of processes such as transferring, reacting, and deposition of gas phase precursors on the surface of a substrate to generate a solid-state thin film. Other methods included in this method include chemical vapor, laser chemical vapor, photo-chemical vapor, plasma-enhanced chemical vapor, metal-organic chemical vapor depositions, and so on. Thin liquid-phase film synthesis is a chemical method for creating thin films that involve liquid-phase precursors. Other sub-methods of this method include chemical bath deposition, electrodeposition, spray pyrolsis, sol-gel, successive ionic layer so on.

Chemical bath deposition is also known as solution growth or controlled precipitation. In this procedure, the substrate of choice is immersed in a solution containing all of the necessary soluble compounds of the desired elements, complexing agents, and other additions. This process has numerous advantages over other types of film synthesis methods

due to its inexpensive cost and lack of the need for specialized and high-precision equipment. It is also possible to deposit efficient thin films in mass production and uniform coating with a low bath temperature. Another key consideration is that this procedure is environmentally friendly, in contrast to other synthesis methods such as vapor deposition techniques. High crystallinity can also be achieved by easily adjusting the composition, stoichiometry, and thickness of the film by varying the precursor concentrations, deposition time and temperature, PH, and other parameters.

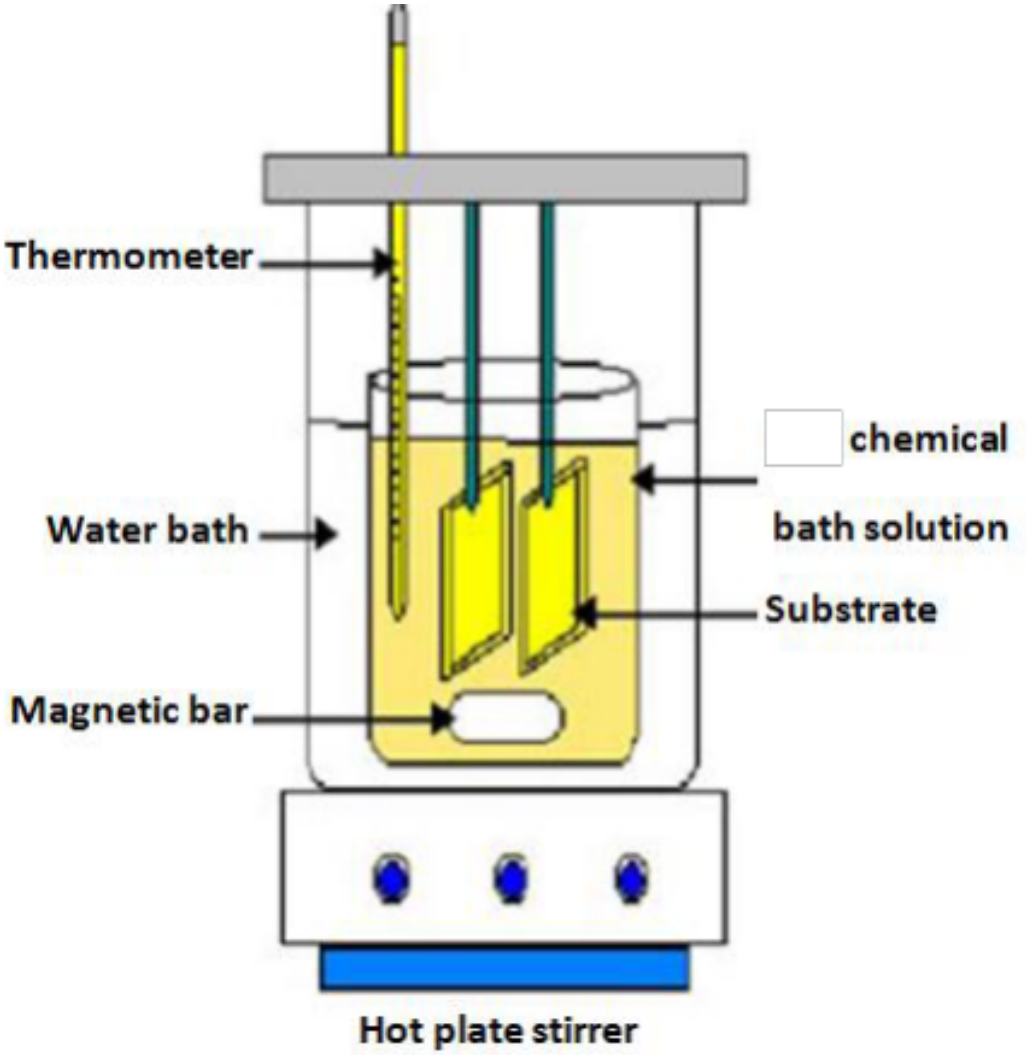

Figure 6: The schematic diagram of the chemical bath deposition (CBD) system

Despite these advantages, chemical bath deposition (CBD) has some drawbacks, including the fact that it is only applicable to a restricted number of materials (compounds), has a low deposition rate, and has a significant probability of impurity inclusion. It is the most often used process for producing chalcogenide and metal oxide films. For example, in the synthesis of ZnTe, thin-film TeO_2 and $ZnCl_2$ were utilized as telluride and zinc sources, respectively, while HCl was used as a complexing agent for an 80 min deposition period and bathing temperature of $70C^o$ (Mehmood et al., 2019; N. Kamoun Allouchea, 2010). This

method can be used to deposit different transition metal-doped zinc chalcogenide thin films for different applications.

2.13. Characterization Techniques

2.13.1 X-Ray Powder Diffraction

X-ray diffraction (XRD) is the most important and widely used non-contact and non-destructive method for determining the structural properties of materials. It can be used to determine lattice parameters and sample texture, such as atomic planes, phase identification, lattice spacing, individual diffraction intensity, preferred orientation, and crystallite size. The X-rays are scattered at a specific angle by each set of lattice planes, and the scattered intensity depends on how the atoms are arranged in the crystal. The scattering from all of the different planes produces a pattern that is unique to the crystal structure of a given molecule (Cullity, 1956).

The structure of thin film can be studied by X-ray diffraction using a diffractometer equipped with CuK_α radiation at a diffraction angle between 2θ = 0 and 80. The lattice constant a, unit cell volume V, and crystal size L will be derived from XRD data using the following equations:

A. Calculation of Lattice Constant (a)

The value of a required for the diffraction of a particular x-ray wavelength λ from planes of spacing d is given by Bragg's law (Cullity, 1956; Sharma et al., 2018).

$$\lambda = 2d_{hkl}\sin\theta, \tag{2.70}$$

where, interplanar spacing, d_{hkl} is given by (Khalfi et al., 2023)

$$\frac{1}{d_{hkl}^2} = \frac{h^2}{a^2} + \frac{k^2}{b^2} + \frac{l^2}{c^2}, \tag{2.71}$$

where, a, b, c are lattice constants and h, k, and l are integers. For a simple cubic structure ($a = b = c$) , the lattice constant becomes

$$a = d_{hkl}\sqrt{h^2 + k^2 + l^2}, \tag{2.72}$$

B. Particle Size and FWHM

For the samples, to calculate crystal size (D), the Scherrer formula and the Joint Committee on Power Diffraction Standards (JCPDS) or the International Centre for Diffraction Data

(ICDD) will be referred to (Sagadevan and Das, 2017)

$$D = \frac{K\lambda}{\beta \cos\theta}, \tag{2.73}$$

where $\lambda$is the wavelength of radiation (for x-ray, CuK_α, λ = 1.5406A^o), β is the line broadening at full-width half maxima (FWHM) and 2θ is the diffraction angle of the peak (in degrees). The value of FWHM is obtained from the plot, i.e., reading for each 2θ value, K is the Scherrer constant; usually, it is 0.9 for spherical and cubic samples.

The microstrain, which is the root mean square variations in the lattice parameters across the sample (in this case, thin films), can be estimated using

$$\varepsilon = \frac{\beta}{4\tan\theta}. \tag{2.74}$$

In cases where both crystalline size and microstrain are irregularly varying with 2θ then the Williamson-Hall plot will be used to find both crystalline size and microstrain (Sharma et al., 2018).

$$\beta\cos\theta = 4\varepsilon\sin\theta + \frac{K\lambda}{D}. \tag{2.75}$$

This gives the form of a linear equation: $y = mx + b$ with $y = \beta\cos\theta$, $m = 4\varepsilon, x = \sin\theta$ and $b = \frac{K\lambda}{D}$.

The dislocation density is the measure of the number of dislocations in a unit volume of crystalline materials and is estimated by

$$\delta = \frac{1}{D^2}. \tag{2.76}$$

2.13.2 UV- Vis Spectroscopy

UV-Vis spectroscopy is a technique for determining the optical properties of an optical material. The absorbance, transmittance, and reflectance of light incident on an optical medium are examples of such optical properties. The UV-V spectrometer can scan a wavelength range between (200-380) nm in the near-ultraviolet and (380–750) nm in the visible regions. The relationship between the incident beam intensity (I_o) and the transmitted beam intensity (I) on the sample under study can be described as follows ():

$$I(d) = I_o e^{-\alpha d}, \tag{2.77}$$

Where α is an absorption coefficient and d is the thickness of the film. The ratio of the incident beam intensity (I_o) to the transmitted beam intensity (I) is the transmittance (T) of the sample under investigation.

$$T = \frac{I}{Io}. \tag{2.78}$$

The relationship between the transmittance (T) and absorbance (A_{abs}) of the sample under investigation is given by

$$A_{abs} = \log\left(\frac{I_o}{I}\right) = \log\left(\frac{1}{T}\right), \tag{2.79}$$

A. Band Gap Measurement

Chalcogenide materials' absorbance is substantially concentrated in the visible part of the electromagnetic spectrum, with absorption coefficients on the order of $10^4 cm^{-1}$. The absorption coefficient (α) is computed using transmission curves in order to determine the optical band gap (E_g)(Ba-sabiah and Seyam, 2017). Using equation (2.77) we can obtain the absorbance coefficient (Giannozzi et al., 2020a).

$$\alpha = \frac{2.302}{d}\log\left(\frac{1}{T}\right), \tag{2.80}$$

Where d and T are the thickness of the film and transmittance, respectively.
The optical band gap values will be obtained from the optical absorption spectra by using Tauc's relation (Pankove, 1975).

$$\alpha h\upsilon = A(h\upsilon - E_g)^r, \tag{2.81}$$

Where, α=$\frac{4\pi k}{\lambda}$ (λ is the wavelength and k is an extinction coefficient) is the linear absorption coefficient of the sample, A is an energy-independent constant, (hυ) is the incident photon energy, E_g is the optical bandgap of the material, and the exponent n depends upon the type of transition. For example, r is the index with values 2, 3, $\frac{1}{2}$ and $\frac{3}{2}$ for allowed indirect transitions, forbidden indirect transitions, allowed direct transitions and forbidden direct transitions respectively.
For the allowed direct transition, the energy-independent constant A is in an equation (2.81) given by (Pankove, 1975; Singh et al., 2017; Makula et al., 2018)

$$A = \left(\frac{e^2}{nch^2 m_e^*}\right)\left(2m_r\right)^{\frac{3}{2}}, \tag{2.82}$$

Where c is the speed of light, n is the refractive index, m_e^* and m_r are the effective and reduced masses of charge carriers, respectively.
Since in our case, the thin films are direct band gap materials, the equation (2.82) can be written as (Singh et al., 2017)

$$\alpha h\upsilon = A(h\upsilon - E_g)^{\frac{1}{2}}, \tag{2.83}$$

The band gap of the thin film can be estimated from $(\alpha h\upsilon)^2$ versus $h\upsilon$ plots by extrapolating the straight line portion of curves to $h\upsilon$ axis.

B. Refractive Index

The refractive index is a complex quantity that can be written as (Swanepoel, 1983; Hasaneen et al., 2020a)

$$N^{'} = n + ik, \tag{2.84}$$

where n is a real part and k is an imaginary part of the refractive index, called the extinction coefficient of the absorption index.

The Swaneopeol envelope method is generally applied to find the real refractive index (n) using interference minima and maxima observed at certain wavelengths from the transmission (Swanepoel, 1983)

$$n = \left[N + (N^2 - n_s^2)^{\frac{1}{2}}\right]^{\frac{1}{2}}, \tag{2.85}$$

Where,

$$N = \frac{n_s^2 + 1}{s} + \frac{2n_s(T_{max} - T_{min})}{T_{max}T_{min}}, \tag{2.86}$$

and

$$k = \frac{\alpha\lambda}{4\pi}, \tag{2.87}$$

Here, T_{min} and T_{max} are the minimum and maximum transmittance of the fringes, respectively. The n_s is the refractive index of the substrate, and it is obtained from the transmission data of clean substrates by using the well-known equation

$$n_s = \frac{1}{T} + \left(\frac{1}{T^2} - 1\right)^{\frac{1}{2}}, \tag{2.88}$$

where, $T = 10^{-A_{abs}} * 100$ is a percent transmittance or simply transmittance, and A_{abs} is absorbance.

The reflectance (R) of the thin films can be obtained from (Giannozzi et al., 2020a; Hasaneen et al., 2020a)

$$R = \frac{(n-1)^2}{(n+1)^2} \tag{2.89}$$

The graphical data can be analyzed by plotting R versus wavelength.

C. Dielectric Constant

The complex dielectric constant can also be obtained in this case (Chowdhury et al., 2017).

$$\varepsilon = \varepsilon_1 + i\varepsilon_2 \tag{2.90}$$

$$= (n^2 - k^2) + i2nk, \tag{2.91}$$

where, $\varepsilon = N^{'2}$. The data of each ε_1 and ε_2 versus λ can be plotted. The probable loss in energy of any fast-moving electron traveling through the material can be estimated by volume and surface energy loss functions, which are obtained from (Singh et al., 2017)

$$V_{elf} = \frac{\varepsilon_2}{\varepsilon_1^2 + \varepsilon_2^2}; \qquad S_{elf} = \frac{\varepsilon_2}{(\varepsilon_1 + 1)^2 + \varepsilon_2^2}, \tag{2.92}$$

The volume energy loss function (V_{elf}) and surface energy loss function of (S_{elf}) of thin films with wavelengths can be plotted. Also, we can estimate the dissipation of electromagnetic energy in these materials through

$$\tan\delta = \frac{\varepsilon_2}{\varepsilon_1}. \tag{2.93}$$

Similarly, $\tan\delta$ versus λ can be plotted, and results will be deduced.

D. Optical Conductivity

The optical conductivity of thin films is given by (Khalfi et al., 2023; Chowdhury et al., 2017)

$$\sigma_{op} = \frac{\alpha nc}{4\pi}, \tag{2.94}$$

where, $c = 299792454 m/s$ is the speed of light. The graph of σ_{op} vs wavelength will be piloted in a similar way.

3. MATERIALS AND METHODS

3.1. Materials

The chemicals we utilized for the synthesis of iron-doped ZnSe thin films are ferrous sulfate heptahydrate, $FeSO_4.7H_2O$ with a molar weight of 277.908 gm (sd fine-chem limited, China), zinc acetate, $(CH_3COO)_2Zn.2H_2O$ with a molar weight of 219.49 gm(Guangdong Guanghua Sci-Tech Co-Tech Ltd, China), selenium powder black (Se) with a molar weight of 78.96 (LOBA Chem, China), sodium hydroxide pellets, NaOH (HiMedia Laboratories Pvt. Ltd, India), sodium sulfite anhydrous, Na_2SO_3(Guangdong Guanghua Sci-Tech Co-Tech Ltd, China) and 80% hydrazine hydrate (H_6N_2O). The zinc acetate precursor is a source for Zn^{2+}, Na_2SeSO_3 solution is for Se^{2-} and ferrous sulfate heptahydrate acts as a source for Fe^{2+}, while hydrazine hydrate (H_6N_2O) is a complexing agent and sodium hydroxide is a PH adjuster.

3.2. Methods

3.2.1 Computational Method

For the $Zn_{(1-x)}Fe_xSe$, the calculations were performed based on spin-polarized and non-spin-polarized DFT as employed in the Quantum Espresso package to analyze its electronic structural, phonon, and magnetic properties for x = 0, 0.0625, 0.125, 0.25, and 0.5 (Giannozzi et al., 2020b). The pseudo-potential type used for those structures was the ultrasoft pseudo-potential (USPP) with the GGA Perdew-Burke-Ernzerhof (PBE-Sol) functional type (Perdew et al., 1996). The calculation is performed by both GGA and GGA+U approximations. For the phonon analysis, the GGA with 0.25% substitution of iron instead of zinc is compared with the ZnSe phonon dispersion. The supercell with the sizes $1 \times 1 \times 2$ and $1 \times 2 \times 2$ was formed in which 25%, 12.5%, and 6.5% of iron are substituted for Zn at the cation site and prepared for calculation as in Fig. 8. Based on the convergence test, a mesh point (9x9x9) was picked in the first irreducible Brillouin zone of the structure ZnSe. Lastly, using the Broyden-Fletcher-Goldfarb-Shanno (BFGS) technique, variable cell relaxation is used to derive the minimal ground state energy lattice parameter and atomic position. The density of states was calculated using the (18x18x18) k-points and 302 crystal k-points for band calculation. The plane wave basis cutoff energy is 60 Ry, and the charge density cutoff energy is 480 Ry. The force and electron convergence thresholds of 10^{-5} and 10^{-8}, respectively, were considered in this calculation.

Also, we calculated those by switching from the pseudo-potential type used in the previous study to the ultrasoft pseudo-potential (USPP) with LDA functionality. Calculations performed based on DFT with the help of a similar package to analyze the

electronic and magnetic properties of $Zn_{(1-x)}Tm_xSe$ (Tm = V, Fe) for x = 0, 0.083, 0.125, 0.25, and 0.5 (Giannozzi et al., 2020b). The supercell with the sizes 1x1x2, 1x2x2, and 3x2x1 was formed in which 25%, 12.5%, and 8.3% of vanadium and iron are substituted instead of Zn and prepared for calculation as in Figure 8 and 9.

For the system of quaternary alloy, $Zn_{(1-x)}Fe_xSe_yTe_{(1-y)}$ (for x = 0, 0.5, 0.25, and 0.125, and y = 0, 0.25, 0.125, and 6.25, we employ the ultrasoft pseudopotential (USPP) with the local density approximation (LDA) functional type to investigate its structural, electronic, and lattice vibration magnetic properties (Perdew and Zunger, 1981). In this case, both LDA and LDA+U approximations are used in the calculations, with U being the Hubbard parameter for the sake of computation cost (Kohn and Sham, 1965; Cococcioni and De Gironcoli, 2005; Timrov et al., 2018). Phonon analysis is performed for the LDA with a 25% substitution of zinc with iron, and the results are compared to the ZnTe phonon dispersion. Also, the 25% substitution of selenium instead of telluride is considered. The investigated crystal structures, with optimal atomic locations, are presented in Figure 11. The XCrySDen program is utilized for crystal structure visualization (Kokalj, 1999). For this study, we create supercells to incorporate the desired percentage of dopant atoms, as depicted in Figure 11. Supercells with dimensions of 1x2x1 and 2x2x1 are constructed to accommodate the required dopant atom percentages within the structure. In these supercells, selenium atoms replace tellurium atoms to create 50%, 25%, 12.5%, and 6.25% Se-doped ZnTe structures. The LDA and LDA+U approximations are then used to explore the effect of selenium doping on structural and electrical properties in the absence of iron. Non-spin-polarized computations consider the following structures: Zn_4SeTe_3, $Zn_4Se_2Te_2$, Zn_8SeTe_7, and $Zn_{16}SeTe_{15}$. We exclude the combination of zinc substitution with iron, as it causes the system to become metallic and does not align with our research interests. Finally, we replace two iron atoms with zinc to further examine the electrical and magnetic properties of the quaternary structure.

For the calculation of superconductivity properties such as the superconducting gap parameter, Fermi surface, relative particle density, electron-phonon coupling, etc., we use PBE approximations to density functional theory (DFT) as implemented in the EPW code, which is incorporated in the Quantum ESPRESSO package. The semi-relativistic norm and conservative pseudo-potentials are used to consider the core valence interactions. We considered the optimized crystal structure in our calculations, as seen in Figure 14. The convergence test for k-points and cutoff was performed. We used 8x8x6 k-points from optimized findings for non-reducible Brillouin zone integration representation. We employed 128 crystal k-points for the band structure and 24x24x18 dense K-points for non-self-consistent function calculations. The energy cutoff employed is 80 Ry. Moreover, we used other supportive packages such as Phonopy, Xcrysden, Vesta, Xmgrace, and Gnuplot for supercell creation, structural visualization and study, graphical analysis, editing, and plotting purposes in this dissertation.

3.2.2 Experimental Method

A. Sodium Selenosulfite Synthesis

Because sodium selenosulfite is an unstable molecule, its product is not commercially available. So, it can be made by combining elemental selenium powder and sodium sulfite anhydrous (Na_2SO_3) in the proper molar ratio (typically 1:3 to 1:6) with the proper heating conditions.

$$Na_2SO_3(s) + Se(s) + H_2O \xrightarrow{heat} Na_2SeSO_3(aq)$$

To do this, 10 g of selenium powder and 30 gm of Na_2SeSO_3 were prepared prior to beginning thin film deposition. By mixing 10 gm of selenium powder black and 30 gm of Na_2SO_3 in 400 mL of double-distilled water in a 500 ml flask. Although selenium black is insoluble in water, it dissolved after 10 hours of refluxing at 80°C with constant stirring. After properly sealing it with aluminum foil and keeping the produced sodium selenosulfite Na_2SeSO_3) solution overnight, the clear colorless solution is obtained, and the little selenium stays up on the cooling and is filtered. Since this solution is not stable, we used up the solution prepared in 3-4 days because, after these days, black sludge will be created in the solution which may affect the quality.

B. Precursors preparation

The weight of 9.3697 gm of zinc acetate was used to form 45 ml of 1M zinc acetate solution in a 150 ml beaker. After a few seconds of a continuous string (200 rev/s), a clear, transparent solution is formed. The stock solution of 2M NaOH is formed in a separate flask by weighing 8.28 gm of NaOH and mixing it with 100 ml of double-distilled water. The 1M of prepared Na$_2$4$SeSO$4$_3$ by refluxing is used in this thin film synthesis as described above. The molar (x M) for a required percent (1, 2, 3 and 4 % of dopant i.e, $FeSO_4.7H_2O$)is calculated by

$$xM = \frac{[1M \times Required\%]}{100\%}$$

Then the amount of zinc acetate in molar (y M) is obtained by

$$yM = 1 - xM$$

The molars (xM and yM) are changed to mass (in gm), let us say the mass of zinc acetate (Z gm) and that of iron heptahydrate (F gm) according to the following equation

$$Zgm = [yM \times Volume\ (L) \times Molar\ Weight \times Purity]$$
$$Fgm = [xM \times Volume\ (L) \times Molar\ Weight \times Purity]$$

By this method, solutions are formed, and the percentages of dopants are adjusted to contain the appropriate proportion of atoms in the solution.

C. Substrate Cleaning

The commercial non-conductive glass substrate was submerged in HCl for an entire night in order to clean the surface of any unwanted contaminants. After that, it is cleaned using detergent and running water. Then it was cleaned with an ultrasonic cleaner for 10 minutes with 96 percent ethanol, followed by double-distilled water made in a laboratory. Before use, it finally dried in the air for four hours.

D. Iron-doped ZnSe Thin Film Synthesis Procedures

45 ml of 1M zinc acetate is poured into a beaker of 150 ml capacity with a constant string. Then 2 ml of 80% of hydrazine hydrate is slowly added to the zinc acetate solution. Sodium hydroxide (NaOH) is added until the PH of the solution becomes 10.8–11. Then 45 ml of Na_2SeSO_3 is slowly added to the solution (not more than 2 minutes), and the solution color changes to orange. At this stage, the solution is transferred to a water bath, and the temperature of the solution is increased up to 75 C^o, This is to facilitate the formation of ZnSe by providing additional energy to the solution. Immediately, the prepared glass substrate is inserted into the solution, and the deposition process lasts for 2 hours. After 2 hours, the deposited thin film is removed from the solution, rinsed with deionized water, and dried in the air. Similarly, 1, 2, 3, and 4 % of 0.5 M of $FeSO_4.7H_2O$ is added before the addition of sodium selenosulfite solution, and all deposition processes are completed in this manner. Finally, to increase the quality of crystalline thin films, all thin films are annealed at 300°C for only 15 min in a furnace. The reports indicated that annealing ZnSe thin films for an extended time may cause phase changes as well as introduce associated oxides like zinc oxides into them (Cosar et al., 2017).

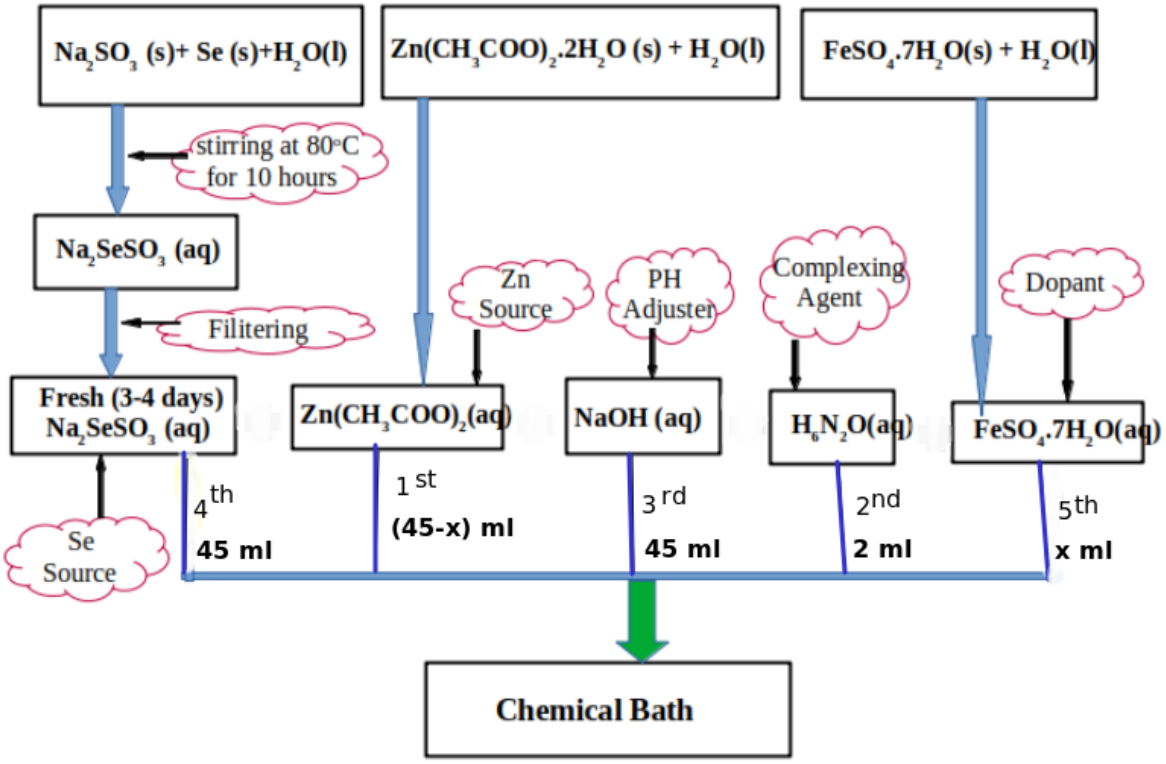

Figure 7: The schematic flow chart of the reaction processes of iron-doped ZnSe thin film synthesis

E. Characterization Techniques

The characterization techniques used in this work are X-ray diffraction (XRD), UV-Vis spectroscopy, and photoluminescence. For the structural (lattice) constant and crystallinity, the X-ray diffractometer (Shimadzu-7000) with the radiation wavelength of KCuα of 1.5046 A^o was used. For the XRD characterization, quality film samples were made and intensity versus 2θ data was collected. The UV-Vis spectroscopy measurements are also performed for the investigation of the electrical properties of synthesized thin films. For this Shimadzu UV-3600 Plus UV-Vis-NIR Spectrophotometer(UV-Vis),) measurement wavelength range of 300-800 nm was used using a slit width of 5 nm. Similarly, to study the quenching, electron-hole recombination, and other luminescence property measurements we used the Photoluminescence spectrometer with the model HORIBA FlouroMax-4 Spectroflourometer with an excitation wavelength of 245 nm and with the slit width of 5 nm to measure the emission spectra of the thin films.

4. RESULTS AND DISCUSSION

4.1. Structural Properties of $Zn_{(1-x)}Fe_xSe_yTe_{(1-y)}$ System

A. Unit Cell Parameter Determination $Zn_{(1-x)}$(Fe, V)$_x$Se System

The calculated lattice parameter used in this study is 5.636$\mathring{A}$ which is almost consistent with the experimental value (Kabita and Indrajit Sharma, 2017). The optimized position of the crystal structure of $Zn_{(1-x)}Fe_xSe$ is as shown in Figure 8. A mesh point ($9 \times 9 \times 9$) was taken in the first irreducible Brillouin zone of the structure ZnSe (Morkoç et al., 1994). The plane wave basis cutoff energy of 60 Ry was used after performing the convergence test, as shown in Figure 10. Since zinc (Zn: [Ar]$3d^{10}4s^2$). iron (Fe:[Ar] $3d^6 4s^2$) and vanadium (V: [Ar]$3d^3 4s^2$) have d-orbital electrons in their electronic structure configuration, so we need to consider the Hubbard parameter, U, in the calculations. Hence, it is estimated for iron via calculation, from which we obtained 6.4580 eV, and for zinc, it is calculated by iteration, when U = 3 eV (E_g = 1.3351 eV) and for U = 6 eV (E_g = 1.376 eV), as well as from previously reported literature of closely related structures (Yaakob et al., 2014; Yadav et al., 2015). Still, the band gap of ZnSe has deviated from the experimental band gap (E_g = 2.7 eV), but usage of U improves the band gap, which is almost similar to the previously reported findings (Yadav et al., 2015; Yang et al., 2009; Radevici et al., 2016) and hence we decided to use iron U = 6.4580 eV and zinc U = 6 eV in our calculations (Timrov et al., 2018; Cococcioni and De Gironcoli, 2005; Rachidi et al., 2016).

Up on the LDA approximation, the calculated lattice parameter used in this study is 5.59$\mathring{A}$ which is almost consistent with experimental as well as reported values (Bilal et al., 2014; Kabita and Indrajit Sharma, 2017). A mesh point ($7 \times 7 \times 7$) was taken in the first irreducible Brillouin zone of the structure ZnSe (Morkoç et al., 1994; Yadav and Pandey, 2012). The plane wave basis cutoff energy of 60 Ry was used after performing the convergence test, as shown in Figure 10. Figure 8 and 9, the optimized position of the crystal, shows that there are four nearest Se atoms to the dopant iron and vanadium atoms. The bond length between the iron and selenide atoms is about 2.4097 $\mathring{A}$ with the bond angle (Se-Fe-Se) of 105.719^o. On the other hand, the bond length between vanadium and selenide in a V: ZnSe is 2.3876 $\mathring{A}$ with a bond angle (Se-V-Se) of 102.339^o which agrees with the experimental results and previously reported findings. The Zn-Se bonding is about 2.4405 $\mathring{A}$ which is close to the reported value (Yadav and Pandey, 2012; Pike et al., 2022). From the calculations, we observed that Fe: ZnSe systems have a minimum total energy as compared to V: ZnSe systems in all concentrations. Thus, iron-doped zinc selenide is relatively more stable than vanadium-doped zinc selenide. This is because Fe: ZnSe systems have a minimum total energy as compared to V: ZnSe systems. For example 50% doped systems, Fe: ZnSe, total energy (E_T) = -915.5 Ry and V: ZnSe, total energy (E_T) = -698.197 Ry.

For the LDA approximation, the Hubbard parameter is estimated for iron and vanadium via calculation, for which we obtained 6.4919 eV and 5.0267 eV, respectively. Still, the band gap of ZnSe has deviated from the experimental band gap (E_g=2.7 eV) but usage of U improves the band gap, which is almost similar to the previously reported findings (Yadav and Pandey, 2012; Yahyaoui et al., 2020) and hence we decided to use the Hubbard parameter of 6.4919 eV, 5.0267 eV, and 6 eV for iron, vanadium, and zinc, respectively, in our LDA calculations (Timrov et al., 2018; Cococcioni and De Gironcoli, 2005; Rachidi et al., 2016).

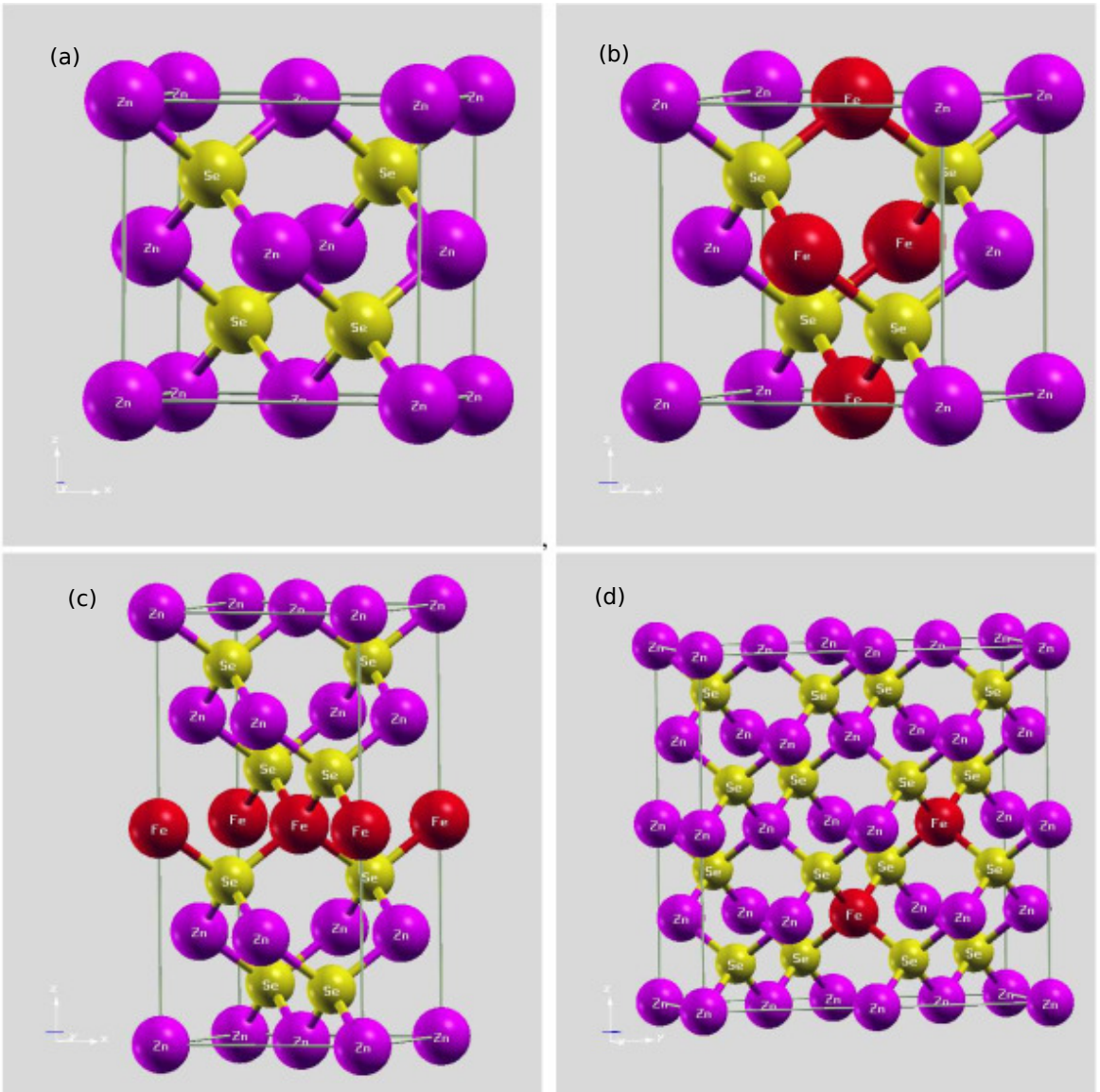

Figure 8: Optimized position crystal structure of a) ZnSe b) $Zn_{0.5}Fe_{0.5}Se$ c) $Zn_{0.75}Fe_{0.25}Se$ d) $Zn_{0.875}Fe_{0.125}Se$

Figure 8 i.e., the optimized position of the crystal, shows that there are four nearest Se atoms to the dopant iron atom. The bond length between the iron and selenide atoms is about 2.4395 $\AA$ with a bond angle of 109.471^o which agrees with the experimental results and previously reported findings (Setyawan and Curtarolo, 2010).

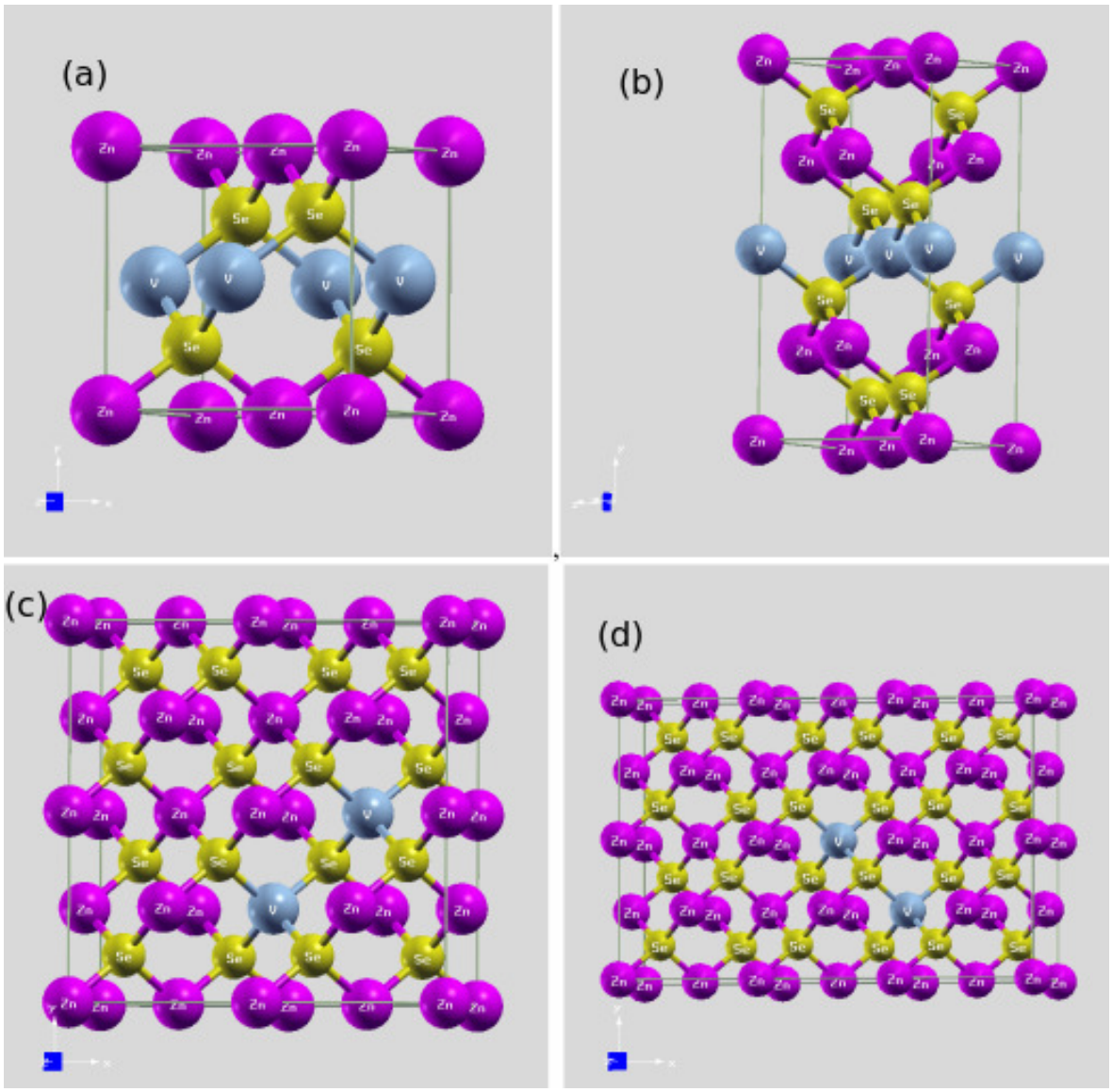

Figure 9: Optimized position crystal structure of a) $Zn_{0.5}V_{0.5}Se$ b) $Zn_{0.75}V_{0.25}Se$ c) $Zn_{0.875}V_{0.125}Se$ and d) $Zn_{0.917}V_{0.083}Se$

The optimized crystal structure of the V: ZnSe system is shown in Figure 9. The concentration of 50, 25, 12.5, and 8.3% of a vanadium atom is doped in a cation site of the ZnSe system. Then these systems' electrical, magnetic properties and phonon are calculated and discussed in the following sections.

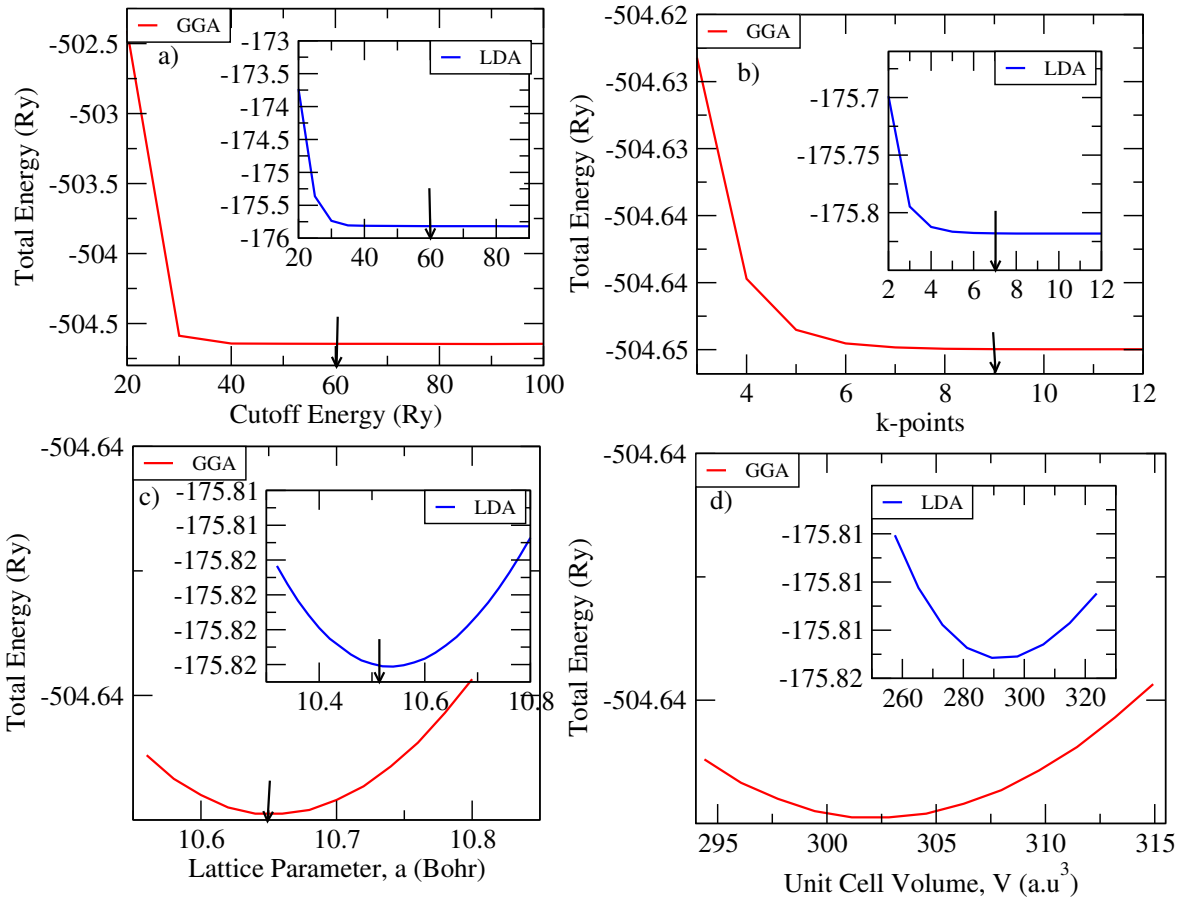

Figure 10: Convergence test for ZnSe, the total energy (Ry) versus a) cutoff energy (Ry) b) K-points c) Lattice parameter (Bohr) d) Volume ($a.u^3$) using GGA and LDA approximations

B. Unit Cell Parameter Determination $Zn_{(1-x)}Fe_xSe_yTe_{(1-y)}$ System

The pseudo-potentials of elements in the alloy used in this study are iron (Fe: [Ar]$3d^6 4s^2$) and zinc (Zn: [Ar]$3d^{10}4s^2$); selenide (Se: [Ar] $3d^{10}4s^2 4p^4$) and telluride (Te:[Kr] $4d^{10}5s^2 5p^4$). In this case, zinc and iron have 3d-orbital electrons in their electronic structure configurations, so it is crucial to account for the U parameter in the calculations. We obtain a U parameter value of 6.3170 eV for iron through calculations, and for zinc, the U parameter was calculated by taking the permissible values of U as 1 eV (E_g = 1.2668 eV) and 6 eV (E_g = 1.3618 eV), which significantly increases the bandgap of ZnTe (Cococcioni and De Gironcoli, 2005). Additionally, the U parameter values of Zn in closely related structures were revised and compared (Habura et al., 2023; Yaakob et al., 2014). Having this evidence, the U parameter is set at 6.3170 eV and 6 eV, respectively, for iron and zinc 3d orbitals (Mann et al., 2016). Prior to performing significant electronic structure computations on the systems, equilibrium parameters were optimized, beginning with the proven empirical lattice parameter of ZnTe, a = b = c = 6.089$\AA$ (Guo et al., 2011). In this study, the computed lattice parameter is 5.972$\AA$ and 6.008$\AA$ using LDA and LDA+U, respectively, which is in line with the experimental value as well as previous reports as in

Figure 12. Based on the convergence test, we selected a mesh point (8x8x8) in the first irreducible Brillouin zone of the structure ZnTe (Hu et al., 2019). Lastly, using the Broyden-Fletcher-Goldfarb-Shanno (BFGS) technique, variable cell relaxation is used to derive the minimal ground state energy lattice parameter and atomic position. The density of states was calculated using the (10x10x10) k points. The optimized crystal structure is shown in Figure 11. The two iron atom is doped in the cation site (Zn position) in optimized ZnTe supercells.

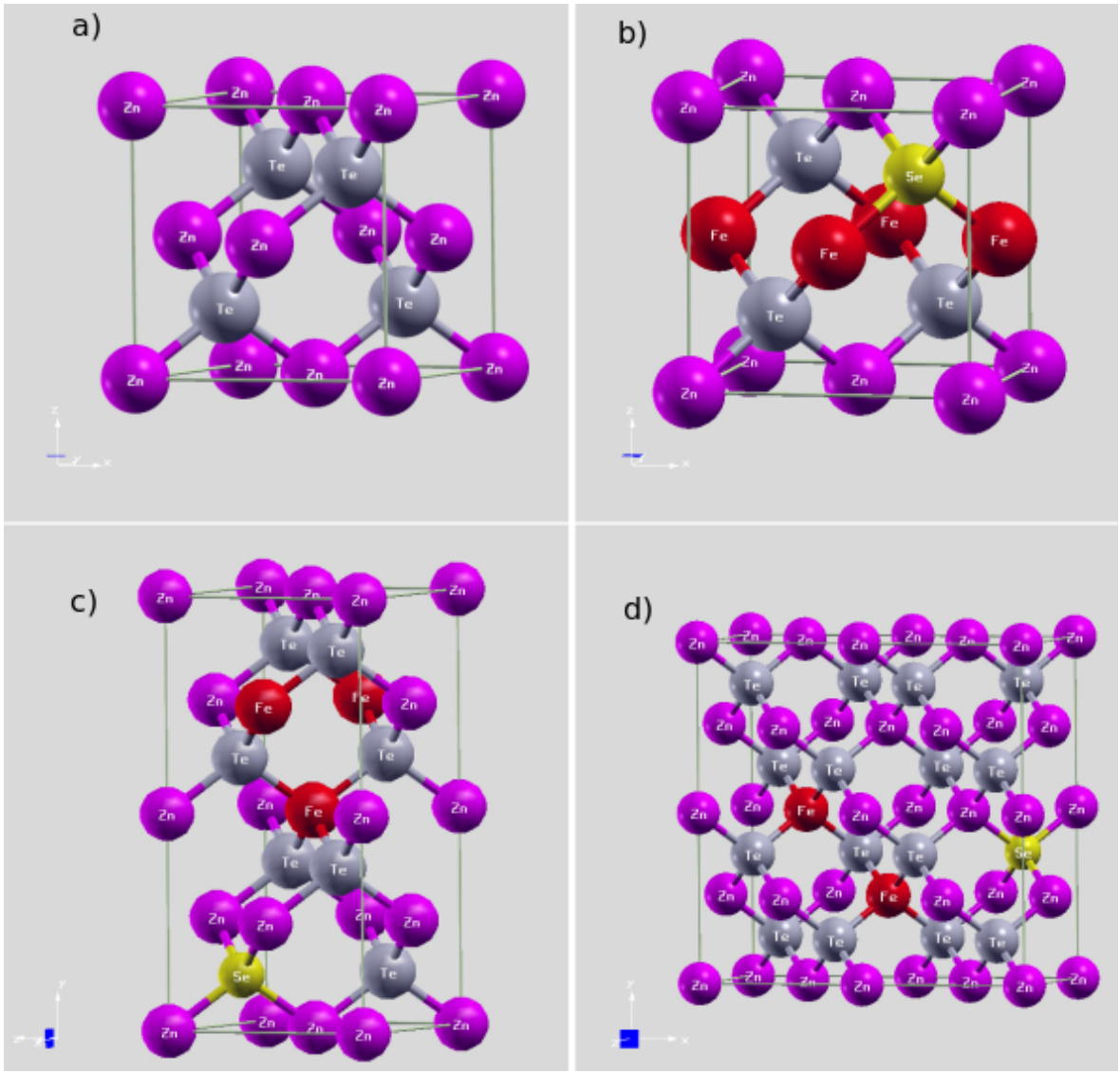

Figure 11: The equilibrium crystal structure of a) ZnTe b) $Zn_{0.5}Fe_{0.5}Se_{0.25}Te_{0.75}$ c) $Zn_{0.75}Fe_{0.25}Se_{0.125}Te_{0.875}$ and d) $Zn_{0.75}Fe_{0.125}Se_{0.0625}Te_{0.9375}$

The cutoff energy for a plane wave basis is 45 Ry, and a charge density cutoff energy of 360 Ry was employed throughout this investigation, which is based on the convergence test shown in Figure 12. The ionic radius of all the elements Zn^{2+}, Fe^{2+}, Se^{2-}, and Te^{2-} is 0.074, 0.076, 0.184, and 0.221 nm respectively, according to (Shannon, 1976; Habura et al., 2023). As a result, the decrease in the lattice constant in selenide-doped ZnTe is already

expected because the ionic radii of the dopant atom are less than those of the host atom. Iron doping in ZnTe, on the other hand, will not cause a decrease in the lattice constant because their ionic radii are comparable.

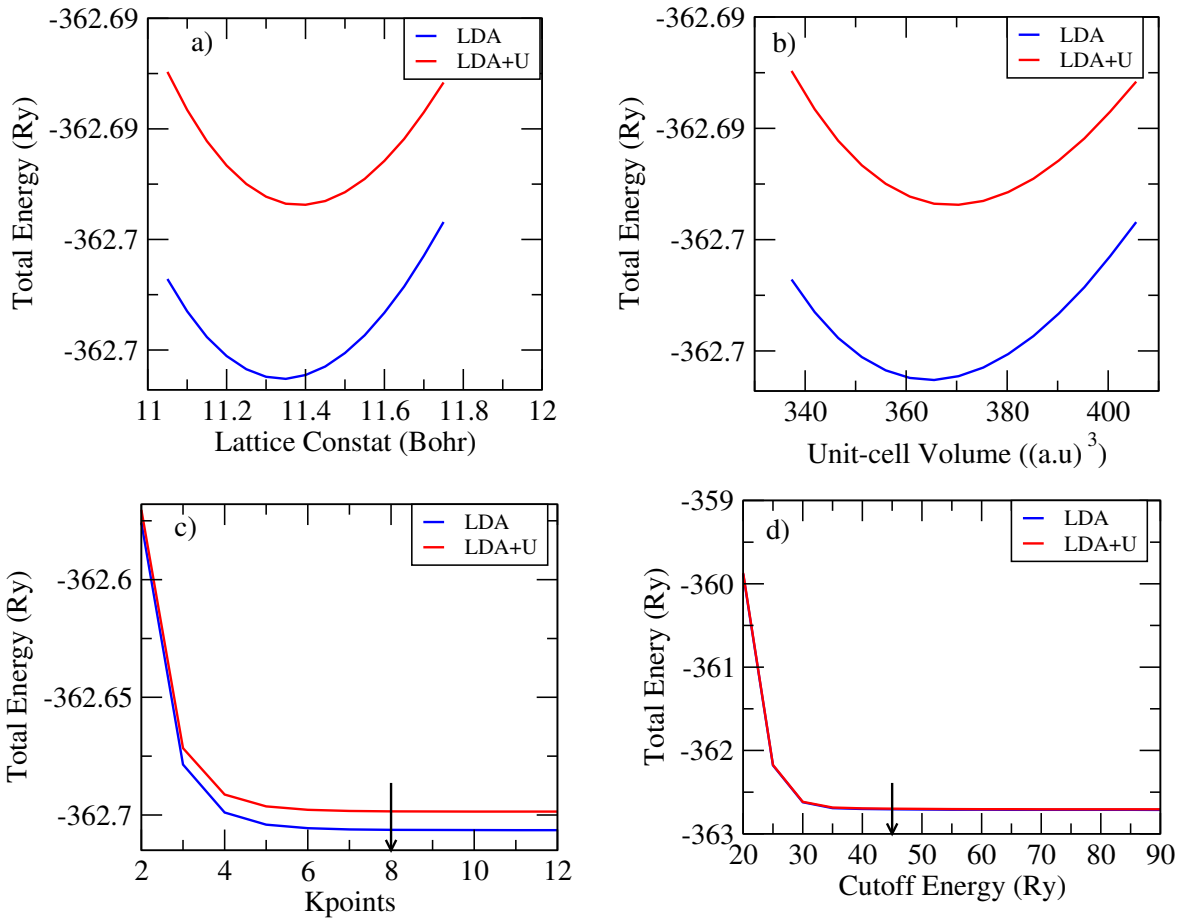

Figure 12: Total Energy versus a) Lattice constant, b) Unit cell volume, c) K-points, and d) Cutoff Energy using the LDA and LDA+U approximations: convergence test for Pristine ZnTe

C. Unit Cell Parameter Determination for FeSe

Before starting the serious calculation of the superconducting properties, the optimization was performed for all required parameters with the help of the confirmed empirical lattice constant of FeSe (i.e., a = 3.765 $\mathring{A}$, c = 5.518 $\mathring{A}$) and the distance between the iron and selenide layers was set to $z_{Se} = 0.2343\mathring{A}$ according to the previous reports (Yaakob et al., 2014). In this case, the calculated lattice parameter for FeSe is a =3.678 $\mathring{A}$ and c = 5.39 $\mathring{A}$ which is close to the experimental value and previous reports. Also, the calculated chalcogenide height considered in this calculation is 0.2538 $\mathring{A}$, as indicated in Figure 14. The FeSe has two structures: tetragonal and orthorombic. In this case, we consider only the tetragonal structure, and its unit cell contains two FeSe molecules. In the optimized primitive unit cell of FeSe, the atomic positions of Fe are (0, 0, 0), $(\frac{1}{2},\frac{1}{2},0)$ and Se $(0,\frac{1}{2},$ 0.74617), $(\frac{1}{2},0,z_{se})$ respectively as show in Figure 14. We used the Xcrysden visualizer and Vesta to study and visualize the crystal structure of FeSe.

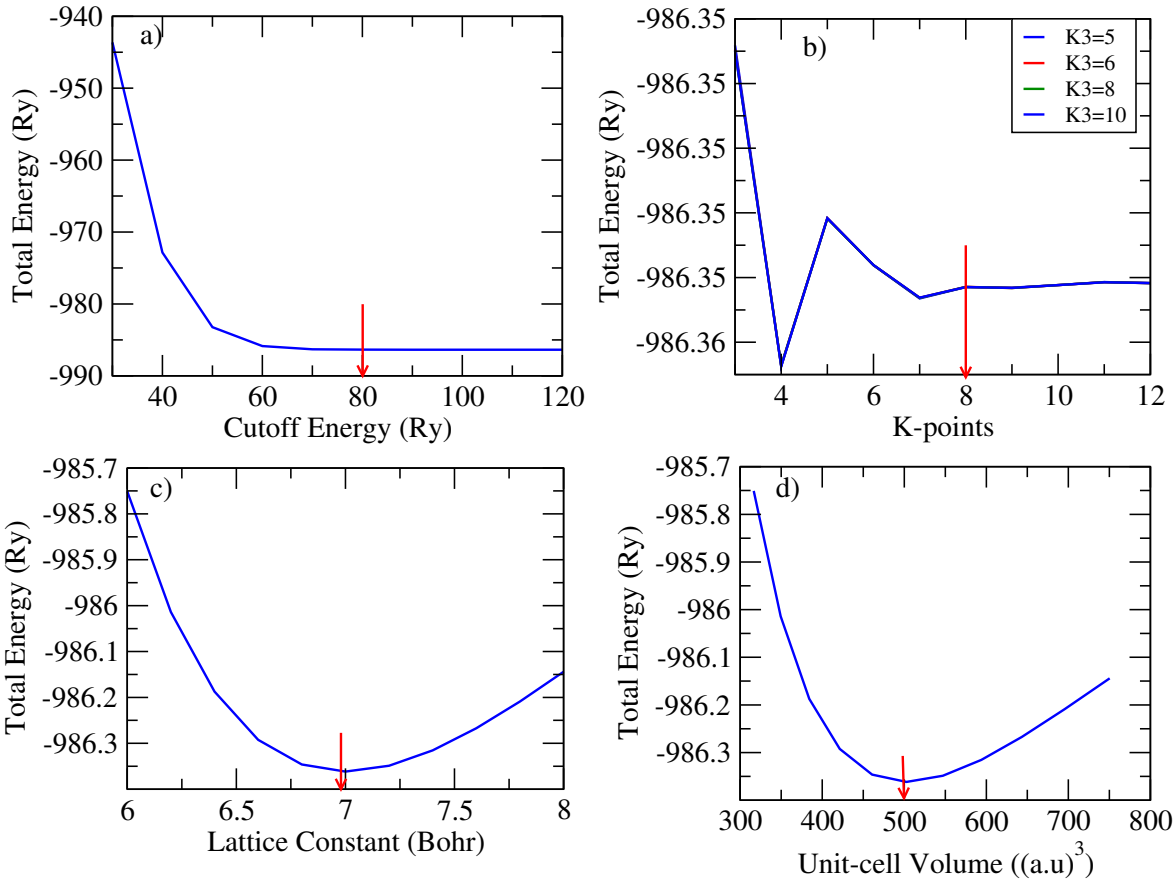

Figure 13: Convergence test for FeSe: Total Energy versus a) Cutoff Energy b) K-points c)Lattice parameter d) Unit cell volume

The iron chalcogenides (FeSe) superconductor is the simplest in a structure among iron-based superconductors, which consists of two-dimensional sheets held by van der Waals interaction, as shown in Figure 14.

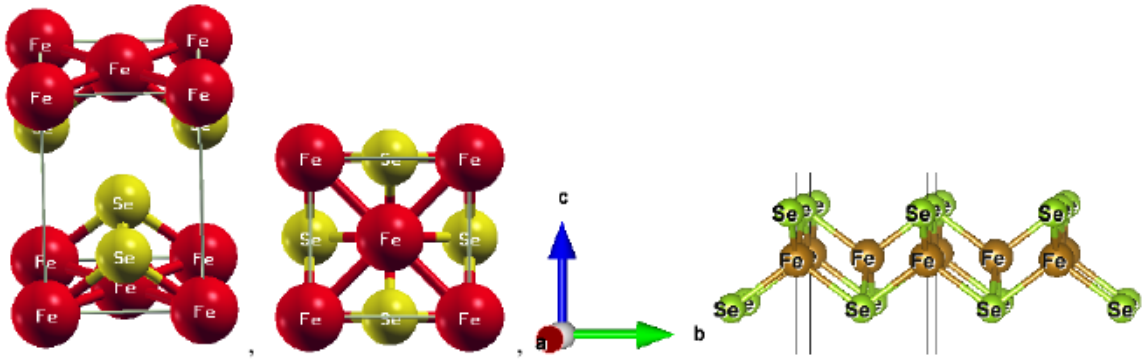

Figure 14: Crystal structure of a) side view, b) top view, and c) two-dimensional crystal structure of FeSe

D. Formation Energy $Zn_{(1-x)}$(Fe, V)$_x$Se System

The energy of formation E_{form} is the energy required to combine two identical transition metal dopants in a ZnSe system (Liu and Zhang, 2017; Yang et al., 2019). The dopants

can be combined with the ZnSe system more easily as the formation energy is lowered. It serves as a direct indicator of how stable the doped ZnSe system is compared to pristine. The stability of transition metal-doped zinc chalcogenide compounds can be determined by the defect formation energy (E_F), and given by

$$E_{form} = E_{Fe/V:ZnSe} - E_{ZnSe} + \sum_{n=1}^{i} n(\mu_{Zn} - \mu_{Fe}), \tag{4.1}$$

where, $E_{Fe:ZnSe}$ and E_{ZnSe} are the total energies of the iron-doped ZnSe and ZnSe supercells, respectively. And also, μ_{Zn} is the chemical potentials of Zn, μ_{Fe} is of the iron atom, and n is the number of the dopant metallic transition element; in this case, there are two iron or vanadium atoms are considered.

Table 1: The calculated formation energy of Fe and V-doped zinc selenide ($Zn_{(1-x)}Fe_xSe$) configurations using GGA and LDA functionals

Functional	**Composition**, x	**Conf.**	Se-rich, E_{form} (Ry)	Zn-rich, E_{form} (Ry)
GGA (Fe-doped)	0.5	N	-0.2949	172.37
	0.25	N	-0.3019	172.35
		NN	-0.1650	172.3082
	0.125	N	-0.3457	172.302
		NN	-0.1696	172.2926
LDA (Fe-doped)	0.5	N	-0.2970	54.62
	0.25	N	-0.32748	54.57
		NN	-0.2241	54.55
	0.125	N	-0.3331	54.56
		NN	-0.2236	54.53
	0.083	N	-0.3696	54.54
LDA (V-doped)	0.5	N	-291.25	-236.53
	0.25	N	-291.26	-236.56
		NN	-291.29	-236.68
	0.125	N	-291.29	-236.69
		N	-291.30	-236.72
	0.083	N	-286.18	-231.58

The formation energy for the $Zn_{(1-x)}$(Fe, V)$_x$Se system is calculated by doping the metallic dopants in symmetric atomic positions in both Zn- and Se-rich conditions, as indicated in Table 1. Accordingly, the formation energy for the selenium-rich condition is more negative than that of the Zn-rich condition in all cases; hence, the selenium-rich condition is energetically more favorable than that of the Zn-rich condition. The negative energies

indicate that both Fe and V doping in ZnSe are bearing the stability by creating stronger bonds (in the case of Se-rich) with the host. So, in this study, the Se-rich condition is considered for further electrical and magnetic property investigations.

Similarly, the stability of the iron and selenium-doped zinc telluride system can be determined by using

$$E_{form} = E_{(Fe,Se:ZnTe)} - E_{ZnTe} + \sum_{n=1}^{i} n(\mu_{Zn} - \mu_{Fe}) + \sum_{m=1}^{i} m(\mu_{Te} - \mu_{Se}), \qquad (4.2)$$

where, $E_{(Fe,Se:ZnTe)}$ and E_{ZnTe} are the total energies of the iron and selenium co-doped ZnTe system and ZnTe supercell, respectively. Also, μ_{Te} is the chemical potential of tellurium, and μ_{Se} is of the selenide atom.

4.2. Electronic Structure of $Zn_{(1-x)}(Fe, V)_xSe_yTe_{(1-y)}$ Systems

A. Electronic Structure of $Zn_{(1-x)}(Fe, V)_xSe$ Systems

The non-magnetic band structure of zinc selenide with iron concentrations of 50%, 25%, 12.5%, and 6.25% is considered in this calculation with both GGA and GGA+U approximations. The band structure of ZnSe and iron-doped ZnSe was calculated based on the k-point path selection Γ-X-W-L-Γ-K-X high symmetry points of the zinc blend structure of ZnSe (Bechiri et al., 2009; Setyawan and Curtarolo, 2010). However, as the doping concentration of iron increases, Fermi energy decreases, and the system becomes fully metallic with no clear band gaps. Hence, iron doping significantly changes the electronic properties of zinc selenide. Specifically, the bandgap energy of cubic zinc-blend ZnSe at Γ point is 1.229 eV when we use the GGA approximation in Figure 15. However, in this case, the energy bandgap obtained is less than that of the average experimental value of 2.7 eV because of the discontinuity of the exchange-correlation function. Still, the bandgap energy obtained in this calculation is in agreement with the previously reported bandgap energy of cubic zinc-blend ZnSe with a similar pseudo-potential (Wang et al., 2016a). Moreover, the band gap and lattice parameter of the structure are enhanced as a result of the GGA+U approximation, as shown in Table 2. For 6.25% substitution of iron, there are gaps created above and below the Fermi level, and certain d-orbitals of iron and zinc are coupled near the Fermi level (Figure 15). From Figures 15 (2a and 2b), we see that the material clearly tends to be n-type semiconducting, as x = 0.0625 with a band gap of 0.5996 eV for GGA and 1.4784 eV for GGA+U approximations, respectively. As the amount of dopant iron atoms decreased to 6.25 percent, two localized states (near Fermi level and slightly below Fermi level) were created in the band gap as a result of the GGA approximation. When the approximation was switched to GGA+U, the localized state between the Fermi level and the top of the valance band was eliminated. This localization in

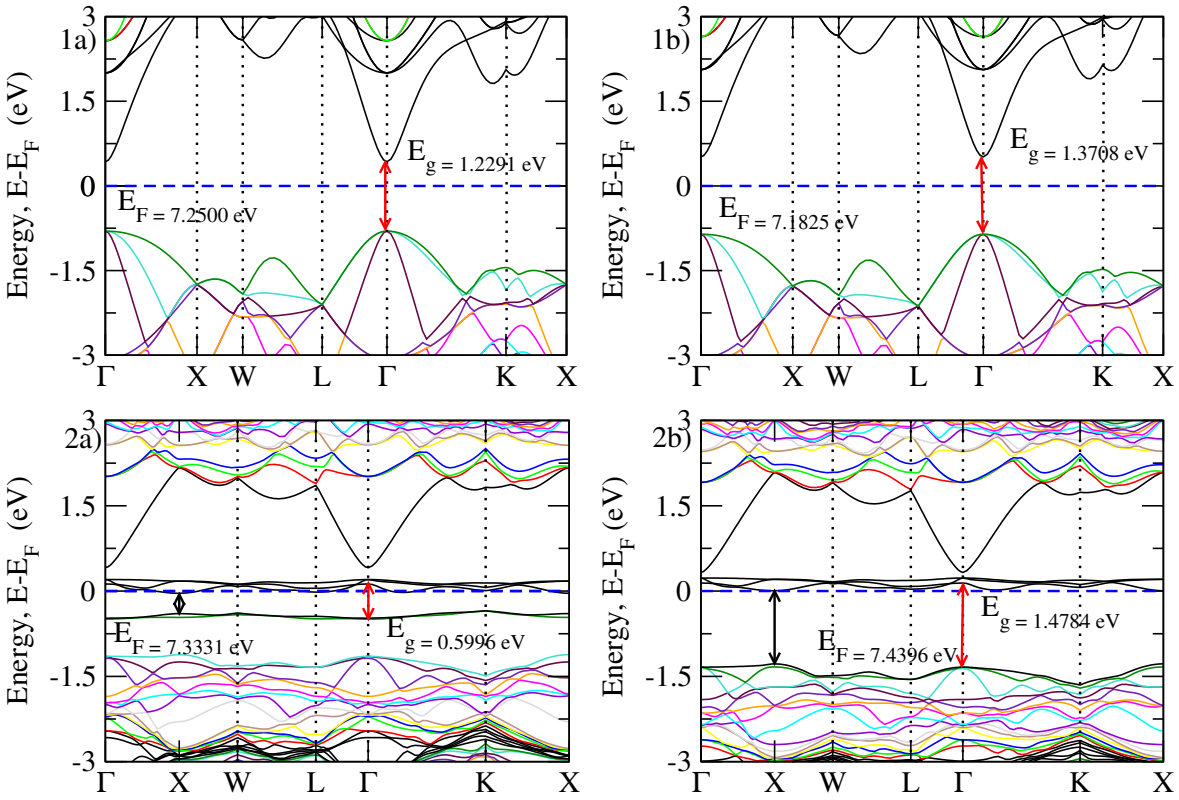

Figure 15: Band structure of 1) ZnSe 2) $Zn_{0.9375}Fe_{0.0625}Se$ with using a) GGA and b) GGA+U approximations respectively.

the material is caused by the interaction of the 3d states of the iron atom and the p-orbitals of the selenide atom. Also, a non-magnetic calculation is performed for zinc selenide using

Table 2: The computed E_g (eV), and lattice constant, a ($\mathring{A}$) for pure zinc selenide and 6.25% Fe-doped zinc selenide using GGA and GGA+U functional. The * indicates this work.

System	**GGA**		**GGA+U**		**Reported**		**Exp.**		**Ref.**
	a	E_g	a	E_g	a	E_g	a	E_g	
ZnSe	5.636*	1.2291*	5.65*	1.3708*	5.640[b]	1.3[c]	5.66[d]	2.73[e]	b (Basak et al., 2012)
Fe: ZnSe	5.63*	0.5996*		1.4784*					c(Yu et al., 2014)
									d(Gromboni and Mascaro, 2016)
									e(Sharma et al., 2018)

both functionals: LDA and LDA+U, as indicated in Figure 16. It is a direct band-gap material. The LDA+U approximation increases the band gap while decreasing the Fermi level (see Figures 16 a and b). The calculated band gap is comparable to the reported values in both cases, as indicated in Table 3. The lattice parameter decreases in both cases because the atomic radii of the dopants (V and Fe) are smaller than those of the parent atom displaced (Zn). Since the atomic radii of Fe, V, and Zn are 1.26 $\mathring{A}$, 1.34 $\mathring{A}$ and 1.42 $\mathring{A}$, respectively, it is already expected that a V and Fe-doped ZnSe system will experience a drop in the lattice constant (Mermin and N.David, 1976; Mahi and Bouhafs, 2012).

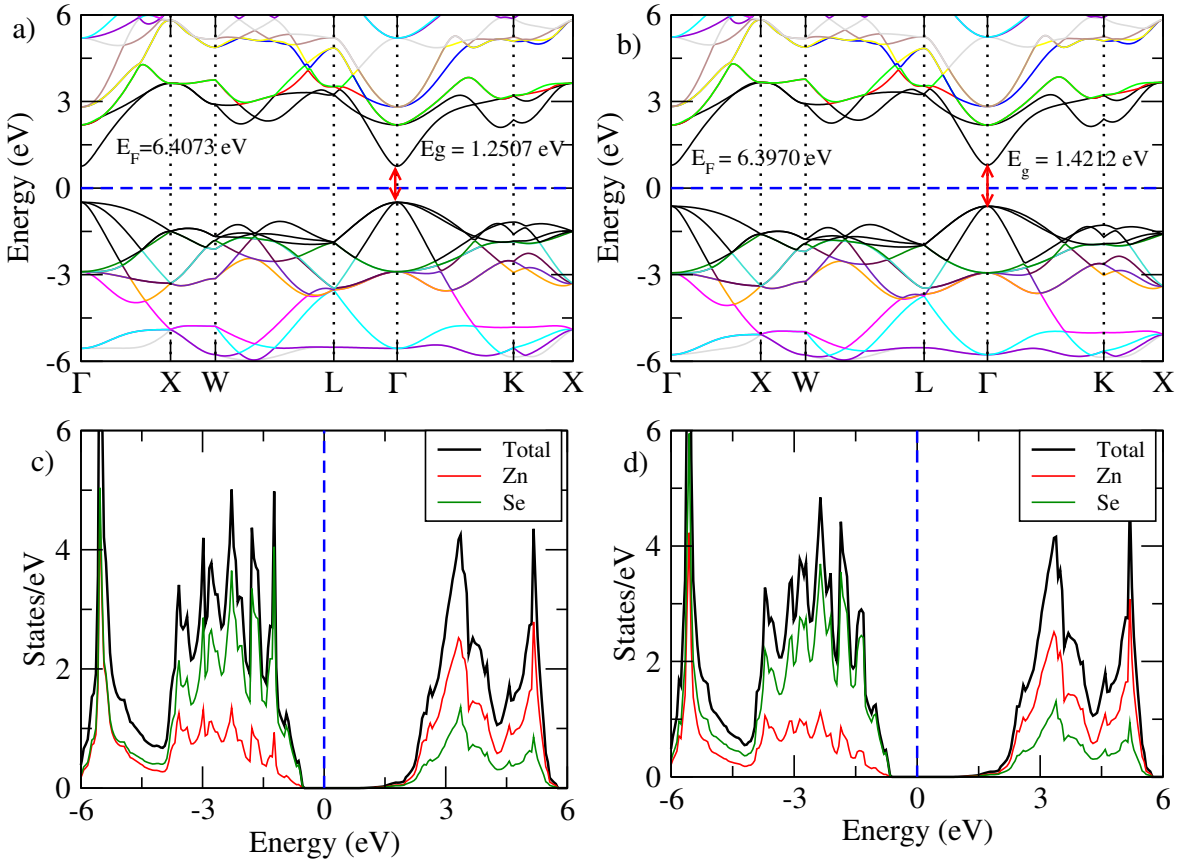

Figure 16: The band structure using a) LDA b) LDA+U and density of state of ZnSe using c) LDA and d) LDA+U approximation, respectively

Table 3: The computed E_g (eV), and lattice constant, a ($\mathring{A}$) for pure zinc selenide, 25% V, and Fe-doped zinc selenide using LDA and LDA+U functional. The * indicates this work

System	LDA		LDA+U		Reported		Exp		References
	a	E_g	a	E_g	a	E_g	a	E_g	
ZnSe	5.57*	1.25*	5.58*	1.42*	5.59[b]	1.3[c]	5.66[d]	2.73[e]	b(Adetunji et al., 2012)
Fe:ZnSe	5.48*		5.539*		5.61(GGA)[f]		5.612[c]		c(Bechiri et al., 2009)
V:ZnSe	5.57*		5.64*		5.6(GGA)[f]				d(Hasaneen et al., 2020b)
									e(Behloul et al., 2016)
									f(Pike et al., 2022)

The non-magnetic densities of state for four systems are investigated, namely: non-doped ZnSe, 50 % doped, 25% doped, 12.5% doped, and 6.25% iron-doped zinc selenide, which are calculated by both GGA and GGA+U approximations. From Figure 17, the result indicates the density of the state is dominated by zinc d-orbitals in a valence band and by selenide p-orbitals in the conduction band. As iron concentration decreases, the Fermi energies of the doped systems increase. The density of states in the doped systems is going to be in three regions: below -2 eV (the region where selenium p-orbitals dominate the density of states), between -2 eV and 2 eV (the iron d-orbitals dominate), and above 2 eV (zinc d-orbitals dominate). There is a better hybridization of iron d-orbitals and selenium p-orbitals near the Fermi level. As iron atom concentration decreases, the density of the state graph

becomes thinner and sharper near the Fermi level and tends to open energy gaps near this region (above and below the Fermi level, see 5a and 5b). In these systems, the bandgap and Fermi energies are improved as compared to GGA approximations.

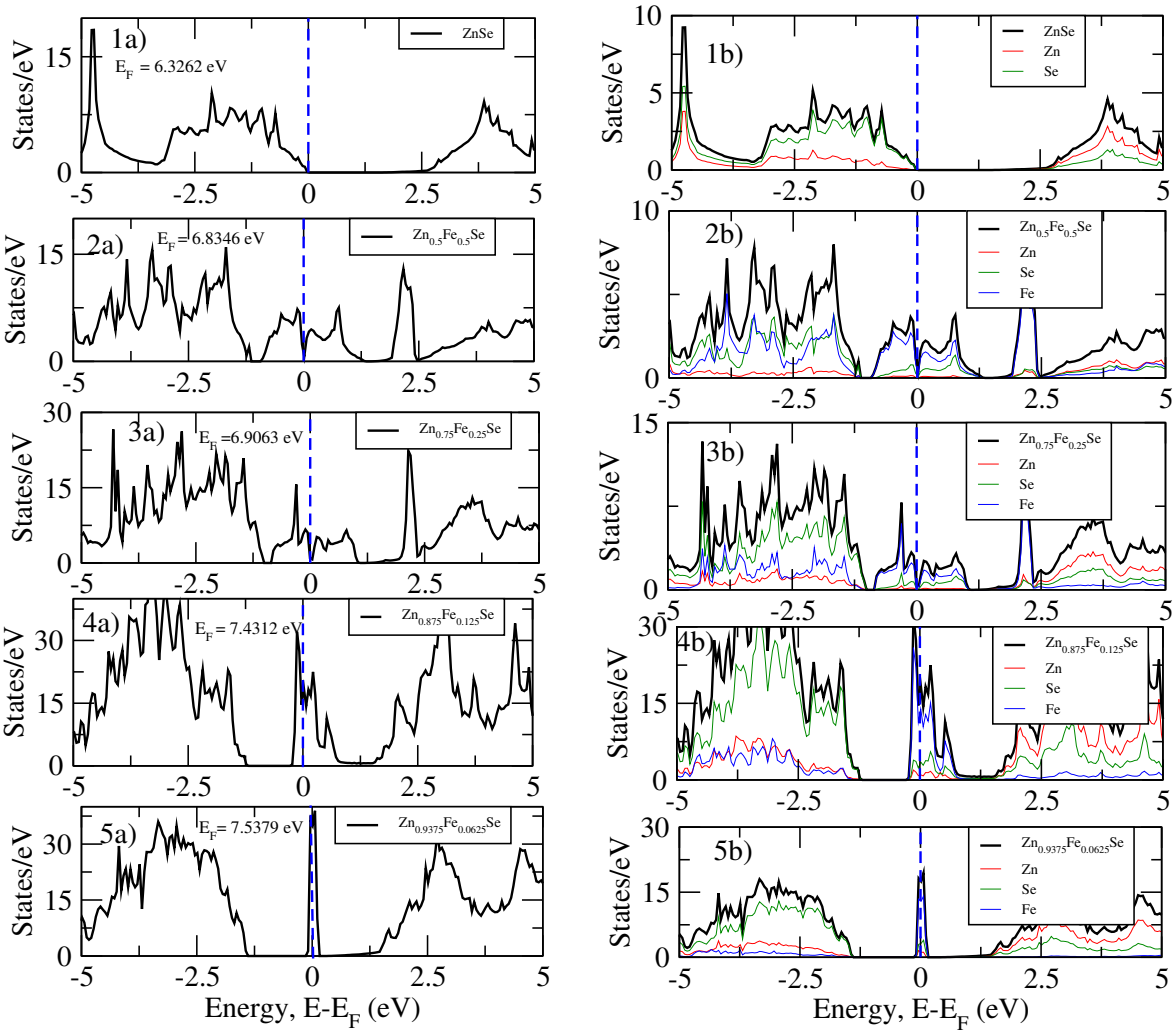

Figure 17: Total a) and partial b) density of state of 1) ZnSe 2) $Zn_{0.5}Fe_{0.5}Se$ and 3) $Zn_{0.75}Fe_{0.25}Se$ 4) $Zn_{0.875}Fe_{0.125}Se$ and 5) $Zn_{0.9375}Fe_{0.0625}Se$ using GGA+U approximation

B. Electronic Properties of $\mathbf{Zn_{(1-x)}Fe_xSe}_yTe_{(1-y)}$ System

As seen from Figures 18 a) and b) and Table 4, the band gap of the $ZnSe_yTe_{(1-y)}$ decreases as the selenide concentration increases up on using both LDA and LDA+U functionals. This is due to an increase in the Se p-orbital overlapping contribution at the top of the valance band in the ZnTe semiconductor without distorting its band gap. The LDA+U approximation enhances the band gap as compared to the LDA approximation. Similarly, the Fermi energy of the systems decreased as the concentration of selenide increased, using both approximations. In this case, the LDA+U approximation inhibits the Fermi energy of the systems as compared to the LDA approximation (see Figure 18 b)

The non-magnetic band structure of Fe- and Se-doped ZnTe is computed and plotted in the range -5 eV to 5 eV, as shown in Figure 19. Due to the dominance of the iron in ZnTe, it does not give rise to a bandgap when doped with Fe, while the band gap decreases when Se is doped instead of telluride.

Table 4: The computed band gap, E_g (eV), and lattice constant, a ($\AA$) of $Zn_{(1-x)}Fe_xSe_yTe_{(1-y)}$ using the LDA and LDA+U functionals. The * indicates this work

x, y	**LDA**		**LDA+U**		**Reported**		**Exp.**		References
	a	E_g	a	E_g	a)	E_g	a	E_g	
0, 0	5.9*	1.33*	6.01*	1.36*	6.0[b]	1.3[c]	6.1[d]	2.26[e]	b(Khenata et al., 2006)
0, 0.0625	5.947*	1.2577*	5.98*	1.38*					c(Yu et al., 2014)
0, 0.125	5.924*	1.1815*	5.958*	1.2228*					d(Singh et al., 2018)
0, 0.25	5.872*	1.03*	5.908*	1.0776*					e(Singh et al., 2019)
0, 0.5	5.775*	0.8204*	5.812*	0.8695*					

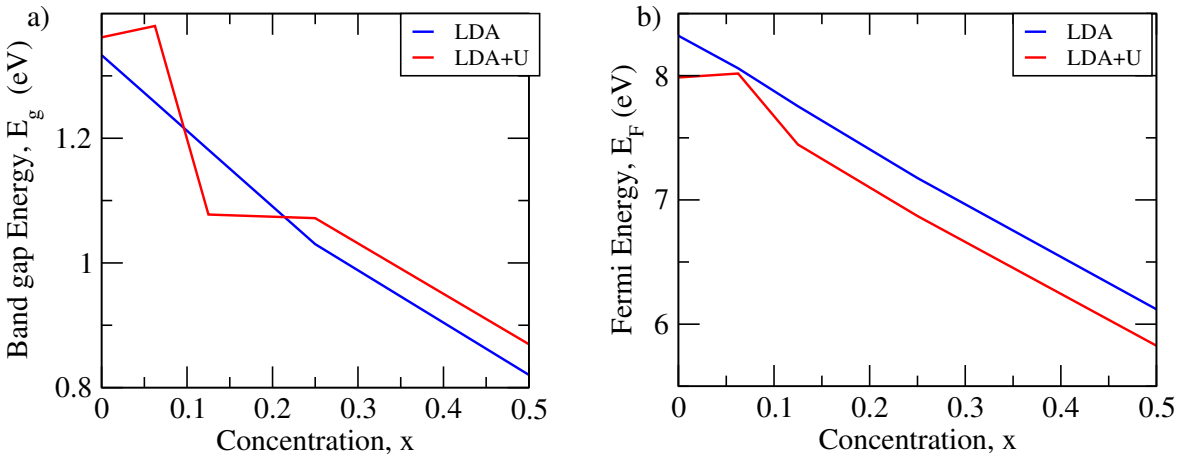

Figure 18: The band gap energy (a) and Fermi energy (b) versus the concentration of alloy $Zn_{(1-x)}Fe_xSe_yTe_{(1-y)}$ (with x = 0 and y = 0.0625, 0.125, and 0.5) utilizing LDA and LDA+U approximations

The band structure of pristine, Fe-, and Se-doped ZnTe was computed using the k-point path selection method, Γ -X-W-K-Γ-L-U of the symmetric point of the cubic crystal (Setyawan and Curtarolo, 2010). Figure 19 shows how the Fermi energy of doped systems differs from that of pristine systems. As a result, the iron and selenide doping significantly alters the electrical characteristics of zinc telluride. As seen from Table 4, the band gap of pristine and Se-doped ZnTe systems is enhanced upon consideration of the Hubbard parameter, U, while the Fermi energy is decreased. The Fermi energy and band gap in a ZnTe structure decreases as the concentration of Se atoms increases, as shown in Figure 19 (1-3) and Table 4. This suggests that the concentration of Se can help control the band gap to the desired value, enabling the material to be tunably employed for various electronic device fabrications. This narrowing in the band gap of Se-doped ZnTe is due to the overlap of the splittings from selenium 4p orbitals on the top of the valance band edge in the ZnTe

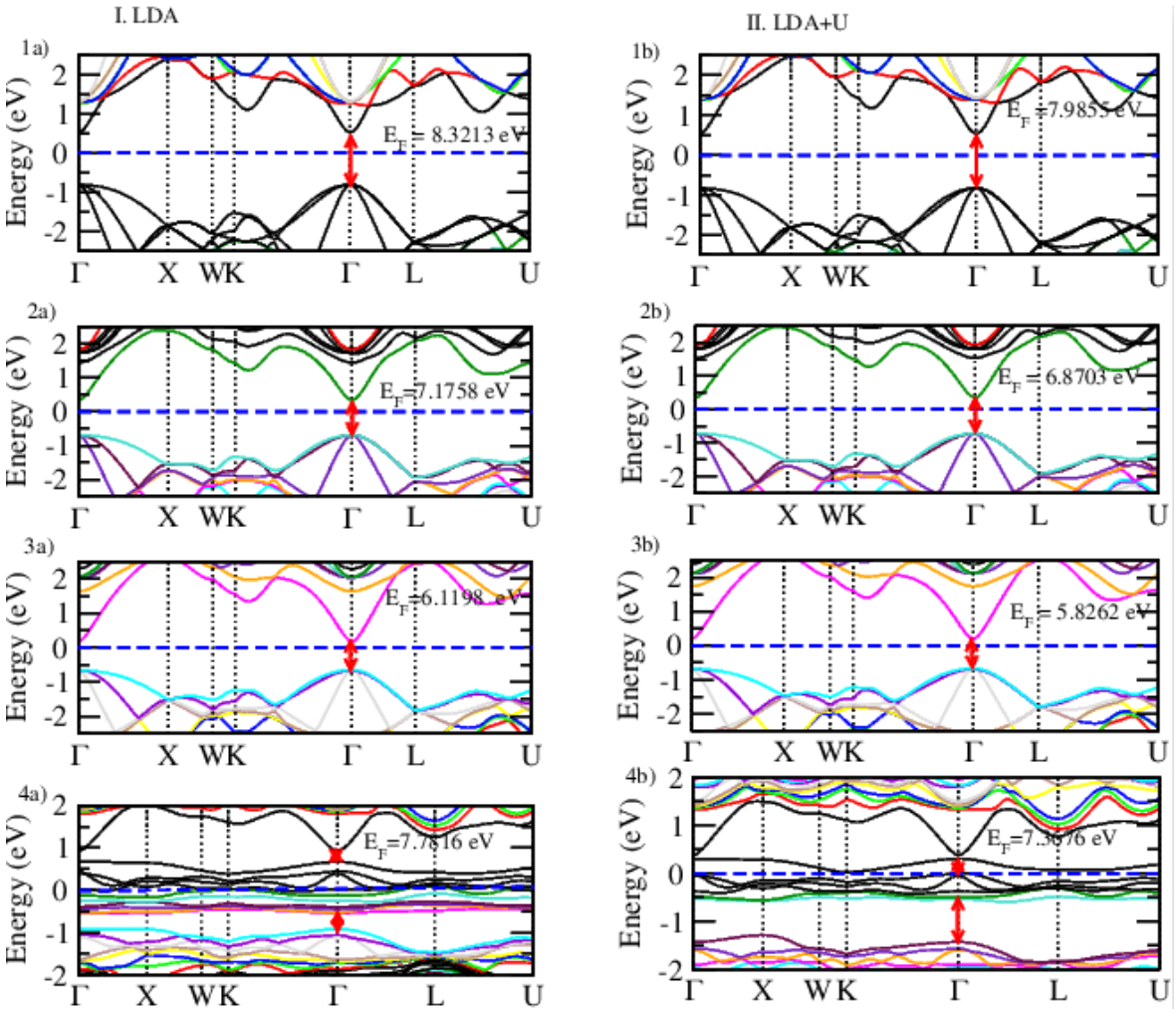

Figure 19: The electrical band structure of 1) Pristine 2) $ZnSe_{0.25}Te_{0.75}$ 3) $ZnSe_{0.5}Te_{0.5}$ and 4) $Zn_{0.875}Fe_{0}.125Se_{0.0625}Te_{0.9375}$ utilizing LDA (I) and LDA+U (II) approximations

semiconductor without distorting the band structure in it. Similar to ZnTe, all Se-doped ZnTe structures are n-type direct band gap semiconductors. However, intermediate and lower concentrations of tellurium in $ZnSe_yTe_{(1-y)}$ can enhance p-type doping (Faschinger et al., 1994b). However, in this study, there is a higher concentration of Te and a lower concentration of Se, which creates the n-type system. Considering the Hubbard parameter in this context, $ZnSe_yTe_{(1-y)}$ enhances the electronic band gap, while the Fermi energy decreases compared to the corresponding calculations in the absence of the Hubbard parameter (Faschinger et al., 1994b).

The non-magnetic calculations of $Zn_{(1-x)}Fe_xSe_yTe_{(1-y)}$ reveal metallic properties in the presence of high concentrations of iron atoms, with no observable band gaps. Conversely, at lower iron concentrations, the structure exhibits a propensity to form localized states in close proximity to the Fermi level, as depicted in Figure 20 (refer to 4a and 4b) and via Figure 21. The breadth of these localized states narrows in conjunction with decreasing iron concentrations. This phenomenon can be attributed to the splitting of iron 3d orbitals, which subsequently gives rise to the creation of localized states. Moreover, this effect contributes

to the luminescent properties of materials containing low concentrations of iron.

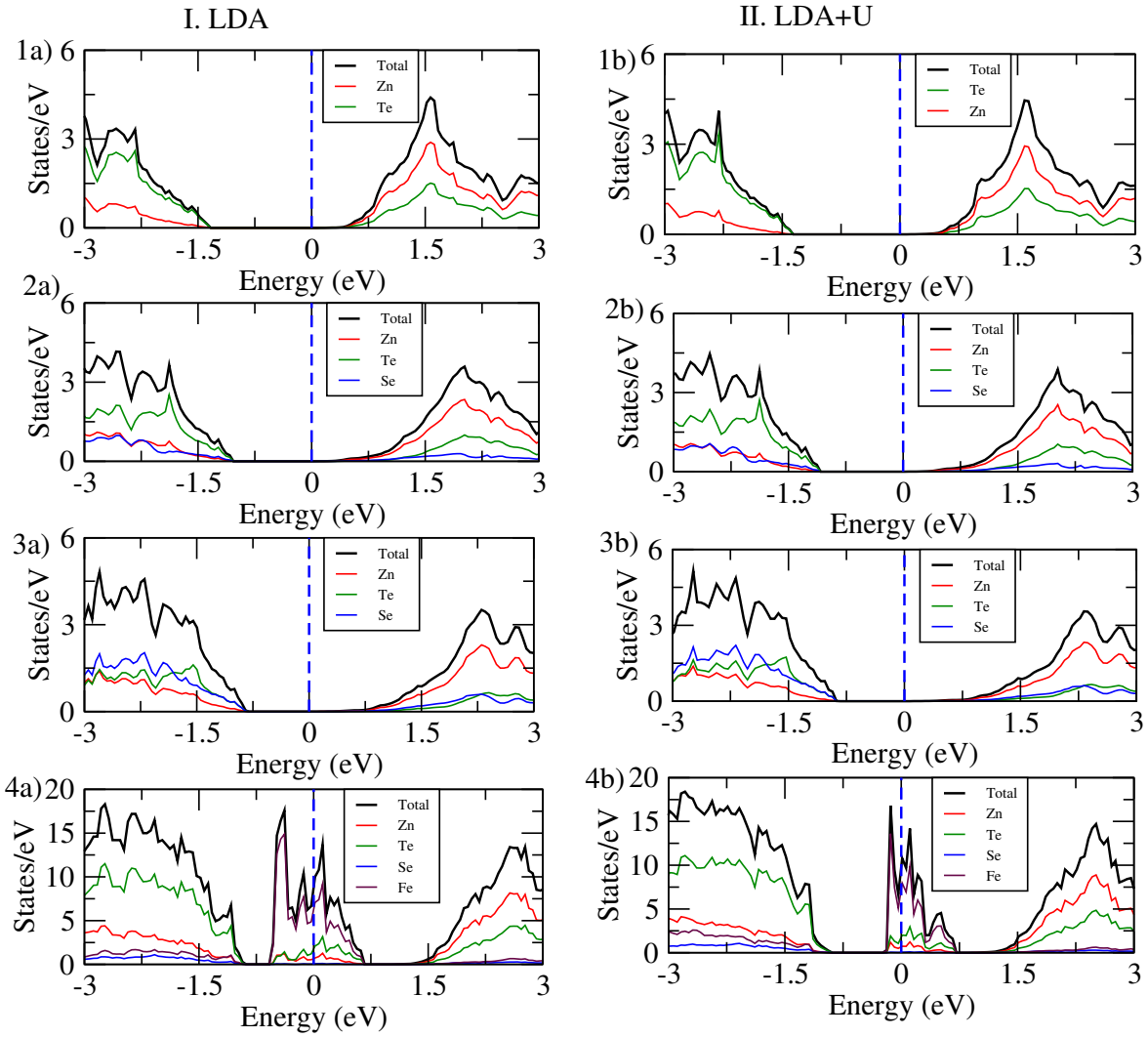

Figure 20: The partial density of states of 1) Pristine 2)$ZnSe_{0.25}Te_{0.75}$ 3) $ZnSe_{0.5}Te_{0.5}$ and 4)$Zn_{0.875}Fe_{0.125}Se_{0.0625}Te_{0.9375}$ utilizing the LDA (I) and LDA+U (II) approximations

The density of states was calculated for $ZnSe_yTe_{(1-y)}$ (i.e., when x=0) and plotted the results in the range of -3 eV to 3 eV, as depicted in Figure 20 (1, 2, and 3). Our results show that the Fermi level, E_F is close to the conduction band, implying that the materials are n-type semiconductors. It demonstrates that broad-band II-VI semiconductors can be easily doped with n-type but refuse to act with p-type doping. On the other hand, ZnTe is easily p-type doped while refusing to be n-type doped due to self-compensation (Faschinger et al., 1994b; Ogawa et al., 1994). According to certain publications, it is also possible to accomplish n-type doping through experimental work (Ogawa et al., 1994; Soykan and Kart, 2012). This investigation indicated that, theoretically, it can be n-type doped for up on the pseudo-potential we used (Adachi, 1999). For lower concentrations of selenide, the density in the valence band is dominated by telluride 5p orbitals, while zinc 3d orbitals dominate above the Fermi level in the conduction band. As the concentration of selenide increases, the

selenide 4p orbitals contribute more to the total density of states in this compound, especially at valance band edges, which is responsible for the reduction of forbidden bandwidth as compared to pristine (see Figures 20 3a and 3b).

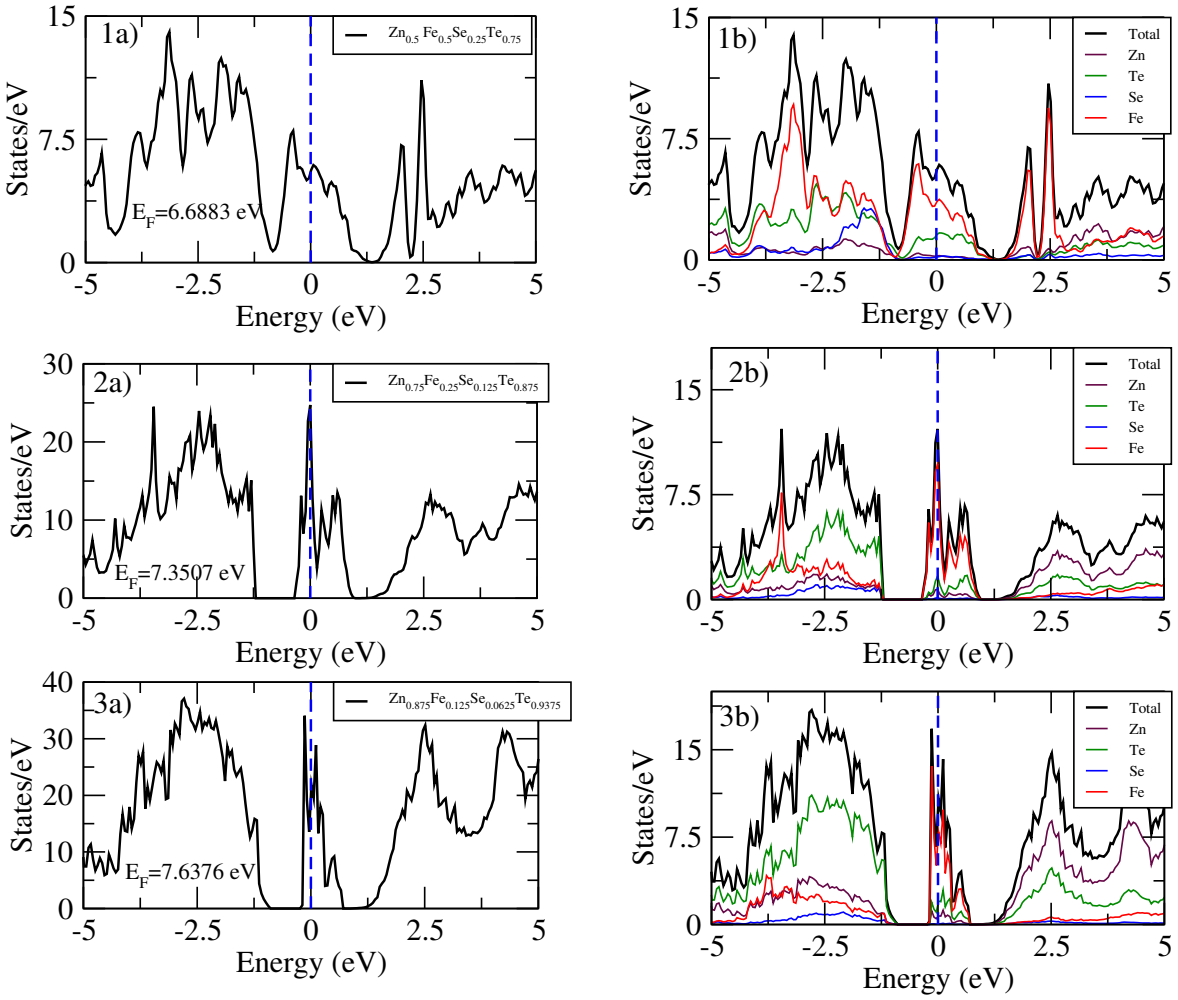

Figure 21: The total (a) and partial (b) density of states of 1) $Zn_{0.5}Fe_{0.5}Se_{0.25}Te_{0.75}$ 2) $Zn_{0.75}Fe_{0.25}Se_{0.125}Te_{0.875}$ and 3) $Zn_{0.875}Fe_{0.125}Se_{0.0625}Te_{0.9375}$ calculated using the LDA+U approximation

Furthermore, we calculated the partial and total density of states (DOS) for the nonmagnetic quaternary alloy of $ZnSe_yTe_{(1-y)}$ for various x and y concentrations, as shown in Figure 21 (1-3). The density is plotted in the range of -5 eV to 5 eV for these structures, as displayed in Figure 21 (1-3). The density of state calculations reveals that the systems are metallic with localized states near the E_F. The width of these localized states decreases as the iron concentration diminishes. This implies that the iron 3d orbitals split over the bandgap of $ZnSe_yTe_{(1-y)}$, making the iron 3d orbitals accountable for the formation of these localized states near the Fermi level. Consequently, the density of the state of iron 3d orbitals dominates in this vicinity. However, at deeper levels within the valence band (around -2.5 eV), telluride 4p orbitals are dominant, while zinc 3d orbitals are the major contributor in the upper bands (at 2.5 eV). The Fermi energy increases as the concentration of iron atoms

decreases. Notably, iron doping transforms the system into a metallic system.

C. Electronic Properties of FeSe

The band structure of non-magnetic FeSe is calculated and plotted in the range -6 eV to 9 eV, as shown in Figure 23. Due to the dominance of the iron in FeSe, it does not give rise to a bandgap. Thus, it confirms that the material is not an insulator. The Fermi level for FeSe of total and partial density of state for bulk is 11.8439 eV. The density of states is dominated by the iron density of states near the Fermi level, while it is dominated by selenide at lower bands (below -3 eV). The density of states of iron decreases and that of selenide increases as we move from the left to the right vicinity of the Fermi level. From Figure 22, we can clearly see that iron dominates the density of states near the Fermi level, while selenide contributes at lower bands. The Fe 3d orbital and the Se-p orbital significantly play roles in the density of states in FeSe. Similarly, the band structure of FeSe confirms that it is metallic, with the occupied states crossing the Fermi level.

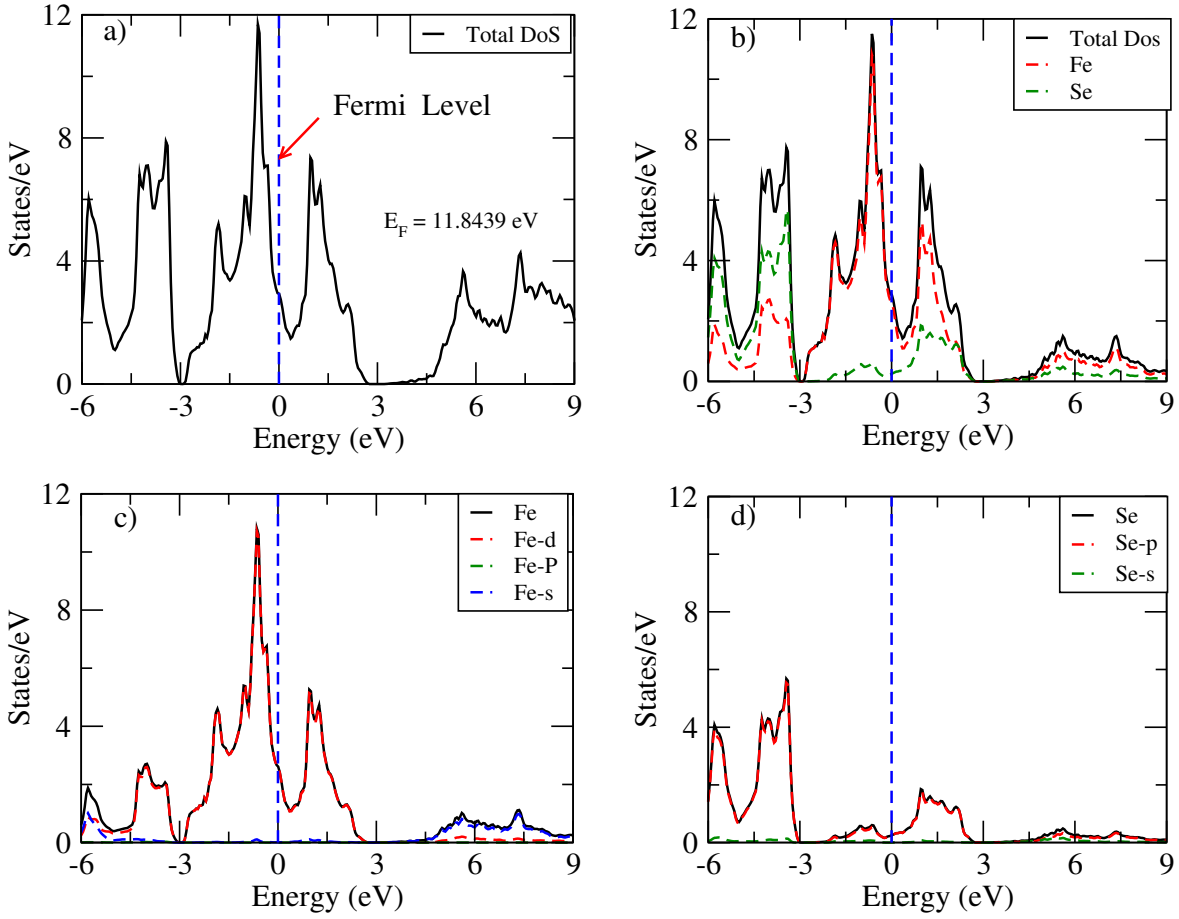

Figure 22: a) Total density of states (TDoS) of FeSe; b) Partial density of states (PDoS) of FeSe; c) Partial density of states (TDoS) of Fe; d) Partial density of states (PDoS) of Se using conservative PBE

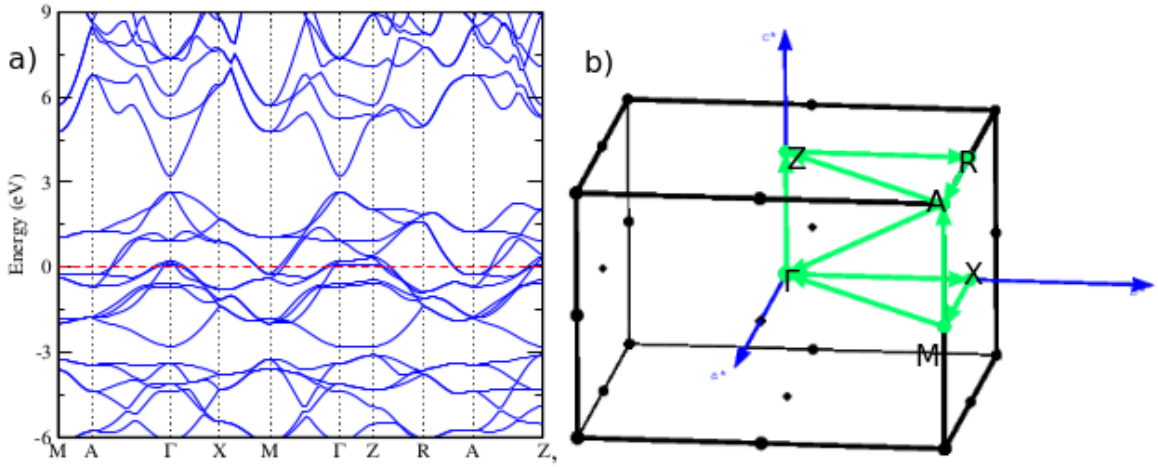

Figure 23: a) The calculated band structure of FeSe; b) k-point path selection of FeSe in a first Brillouin zone

4.3. Spin Polarized Calculations of $Zn_{(1-x)}(Fe,V)_xSe_yTe_{(1-y)}$ System

A. Spin-Polarized Band Structure of $Zn_{(1-x)}(Fe,V)_xSe$ System

The magnetic band structure of the iron-doped zinc selenide system $Zn_{0.5}Fe_{0.5}Se$, $Zn_{0.75}Fe_{0.25}Se$ and $Zn_{0.875}Fe_{0.125}Se$ are calculated both for spin-polarized systems by using both GGA and GGA+U approximations. In both approximations, the spin-polarized band structure leads to the insulating states in one of the spin channels. The GGA approximation leads to degeneracy with n-type behaviors in spin-down channels. In addition, for the minority spin channel the p-type degeneracy is observed as the dopant concentration of 50% meanwhile it becomes semiconducting as the concentration of the impurity atom decreases. As a result of the spin-polarized magnetic band structure calculation, the direct band gap is observed for both spin-up and spin-down channels. In general, this approximation revealed that the half-metallic property in $Zn_{0.5}Fe_{0.5}Se$, $Zn_{0.75}Fe_{0.25}Se$ and $Zn_{0.875}Fe_{0.125}Se$ materials.

On the other hand, the spin-polarized band structure calculation using GGA+U was performed and plotted in the energy range from -3 eV to 3 eV for both spins (down) and spin (up) systems, as shown in Figure 24. In this case, the finding shows that there are two distinct bands with wider gaps in the materials. This is due to the splitting of iron atoms' 3d degenerate states without distortion of the semiconducting behavior in ZnSe. Moreover, as the dopant concentration lowered to 12.5%, the Fermi energy remained in the valance band, and the materials again became degenerate p-type semiconductors. In this case, with a majority spin channel, the overlapping from iron 3d states rises beyond the top of the valance band of ZnSe, resulting in the formation of an indirect band gap in the system. The band gap changes in these systems are due to the hybridization of band electrons and localized 3d electrons in iron atoms. In the case of 12.5% concentration in the majority spin channel, the

exchange interaction between the 3d states of iron atoms and the selenide p-orbitals form localized states in the band gap (at the Fermi level). The comparison of Fermi energies and band gaps of these materials is summarized in Table 5.

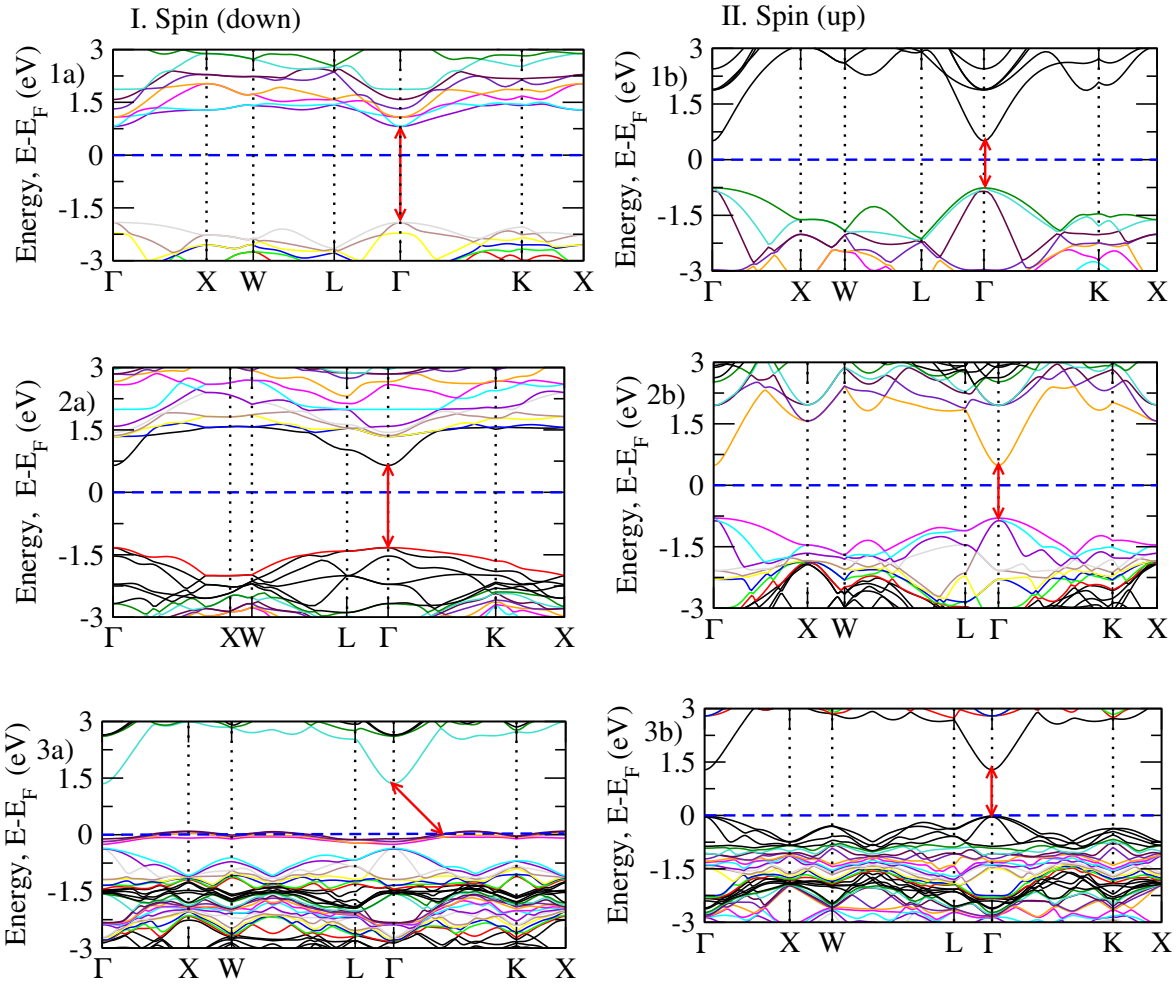

Figure 24: The spin-polarized band structure of the spin-down (majority spin) (a) and spin-up (minority) (b) systems 1) $Zn_{0.5}Fe_{0.5}Se$ 2)$Zn_{0.75}Fe_{0.25}Se$ and 3)$Zn_{0.875}Fe_{0.125}Se$ respectively, using the GGA+U approximation

The spin-polarized band structure of the vanadium and iron-doped zinc selenide systems was computed using the LDA and LDA+U approximations, as illustrated in Figures 25, 26, 27 and 28. The selection of high symmetric k-points path is Γ-X-W-L-Γ-K-X for the zinc blend structure of ZnSe (Bechiri et al., 2009; Rachidi et al., 2016; Setyawan and Curtarolo, 2010). From Figure 25 the spin-polarized band structure of iron-doped ZnSe was calculated using LDA approximation. In contrast to spin-down channels around the Fermi level, where the distinct band gap is not visible, direct band-gap p-type semiconducting characteristics are seen in spin-up channels. Consequently, the LDA approximation reveals that the materials $Zn_{0.5}Fe_{0.5}Se$, $Zn_{0.75}Fe_{0.25}Se$, $Zn_{0.875}Fe_{0.125}Se$ and $Zn_{0.917}Fe_{0.083}Se$ are half-metallic. This property is due to the interaction of iron atoms 3d states with the Se p state being responsible. As shown in Figure 26, both channels exhibit distinct band gaps,

Table 5: The spin-polarized band gap (E_g) at Γ point and Fermi energy (E_F) for the different spin-polarized iron-doped ZnSe systems with different configurations (conf.)

Functional	**System**	**Conf.**	E_F (eV)	**Spin(dn)**,E_g (eV)	**Spin(up)**,E_g (eV)
GGA	$Zn_{0.5}Fe_{0.5}Se$	N	7.28	1.5	0.75
	$Zn_{0.75}Fe_{0.25}Se$	N	7.26	1.06	0.78
		NN	7.30	1.3	0.93
	$Zn_{0.875}Fe_{0.125}Se$	N	7.30	0.97	0.94
GGA+U	$Zn_{0.5}Fe_{0.5}Se$	N	7.74	2.72	1.26
	$Zn_{0.75}Fe_{0.25}Se$	N	7.47	1.97	1.28
		NN	6.5	1.55	1.39
	$Zn_{0.875}Fe_{0.125}Se$	N	6.54	1.46	1.29

according to the calculation performed using the LDA+U approximation. It indicates that the materials have semiconducting and magnetic properties. The materials: $Zn_{0.5}Fe_{0.5}Se$ and $Zn_{0.75}Fe_{0.25}Se$ tends to behave as an n-type semiconducting, while $Zn_{0.875}Fe_{0.125}Se$ and $Zn_{0.917}Fe_{0.083}Se$ are p-type since their Fermi level is near valance band edge. Similarly, the spin-polarized band structure is calculated for vanadium-doped ZnSe, but it exhibits entirely different electrical and magnetic properties, as seen in Figures 27 and 28. From Figure 27, the LDA approximation reveals that the minority spin channel (spin down) is a degenerate n-type semiconductor, while the majority channel is entirely metallic. Thus, our result for the LDA approximation confirms that the vanadium-doped ZnSe is metallic for x = 0.5, 0.25, 0.125, and 0.083. Moreover, the localized states are observed in the 12.5% and 8.3% substitution of vanadium instead of zinc atoms. The calculations using the LDA+U approximation revealed that the spin-down channel has n-type semiconducting behavior with a clear band gap, while the majority spin channel indicates the material is metallic with no localized states observed. The band gap of materials is enhanced in minority channels both in a Fe and V-doped ZnSe system, as described in Table 6.

Table 6: The spin-polarized band gap, (E_g) at Γ point and Fermi energy, (E_F) for $Zn_{1-x}Fe_xSe$ systems using LDA and LDA+U approximation

Functional	x	Fe-doped			V-doped		
		$E_F(eV)$	**dn**,E_g (eV)	**up**,E_g (eV)	$E_F(eV)$	**dn**,E_g (eV)	**up**,E_g (eV)
LDA	0.5	7.07	-	0.63	8.13	2.4	-
	0.25	6.88	-	0.79	7.74	1.78	-
	0.125	6.78	-	0.86	7.59	1.70	-
	0.083		-		7.02	1.38	
LDA+U	0.5	7.53	2.62	1.28	7.78	2.73	-
	0.25	7.14	2.05	1.31	7.35	2.01	-
	0.125	6.06	1.54	0.85	7.41	1.80	

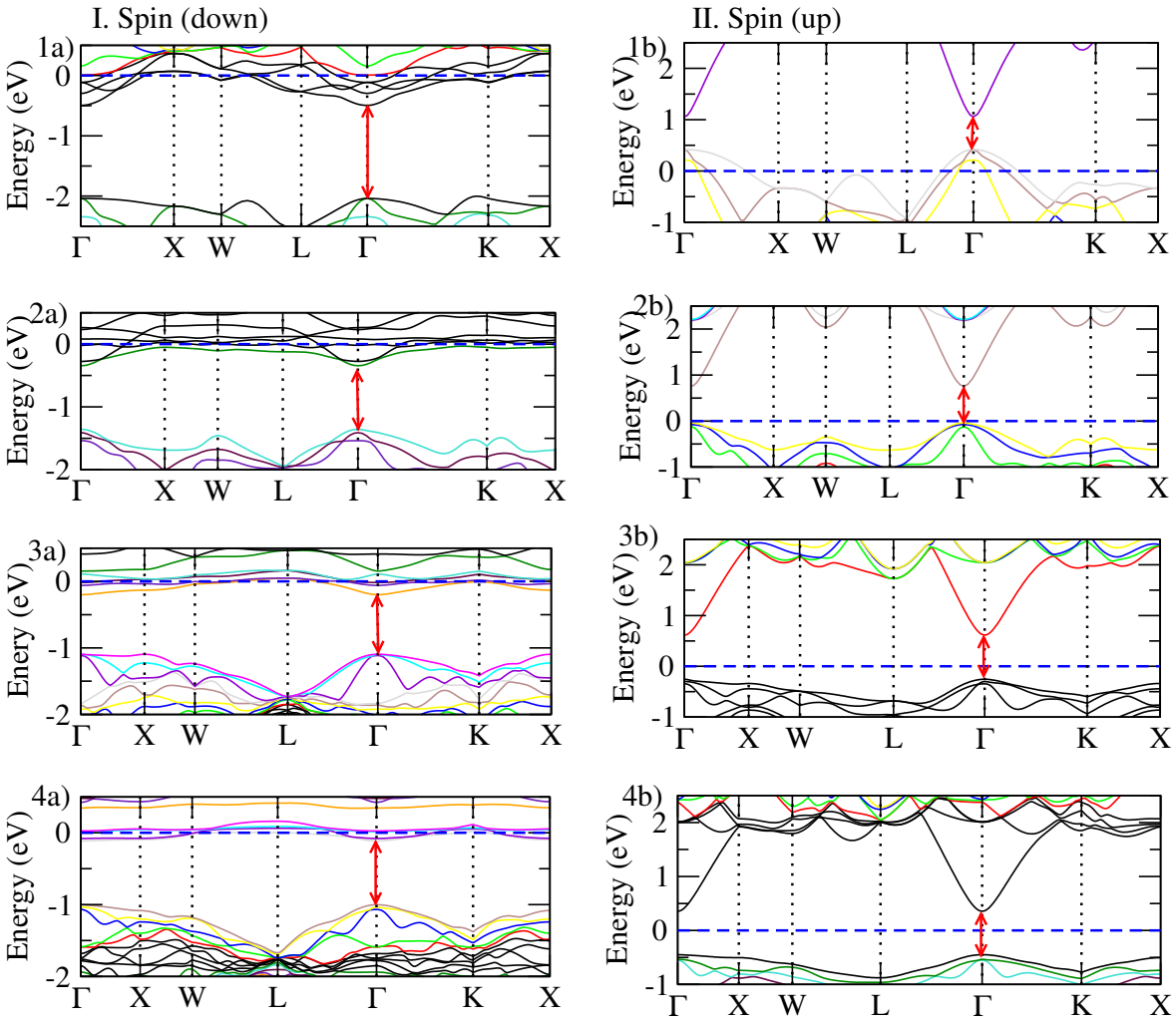

Figure 25: The spin-polarized band structure of the spin-down (majority spin) (I) and spin-up (minority) (II) systems 1) $Zn_{0.5}Fe_{0.5}Se$ 2) $Zn_{0.75}Fe_{0.25}Se$, 3) $Zn_{0.875}Fe_{0.125}Se$ and 4) $Zn_{0.917}Fe_{0.083}Se$ respectively using LDA approximation

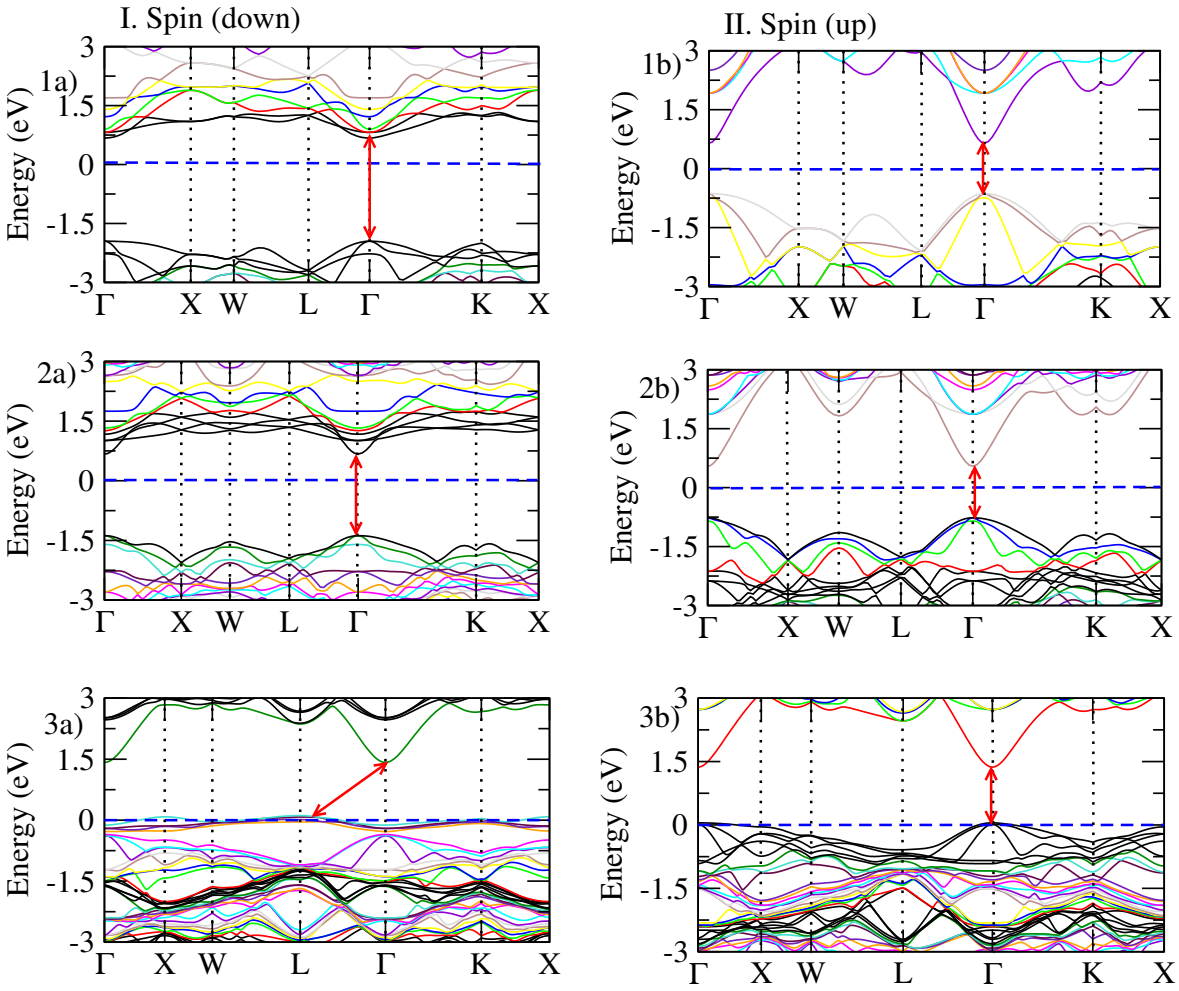

Figure 26: The spin-polarized band structure of spin down (majority spin) (I) and spin up (minority spin) (II) systems 1) $Zn_{0.5}Fe_{0.5}Se$ 2) $Zn_{0.75}Fe_{0.25}Se$ and 3) $Zn_{0.875}Fe_{0.125}Se$ respectively using LDA+U approximation

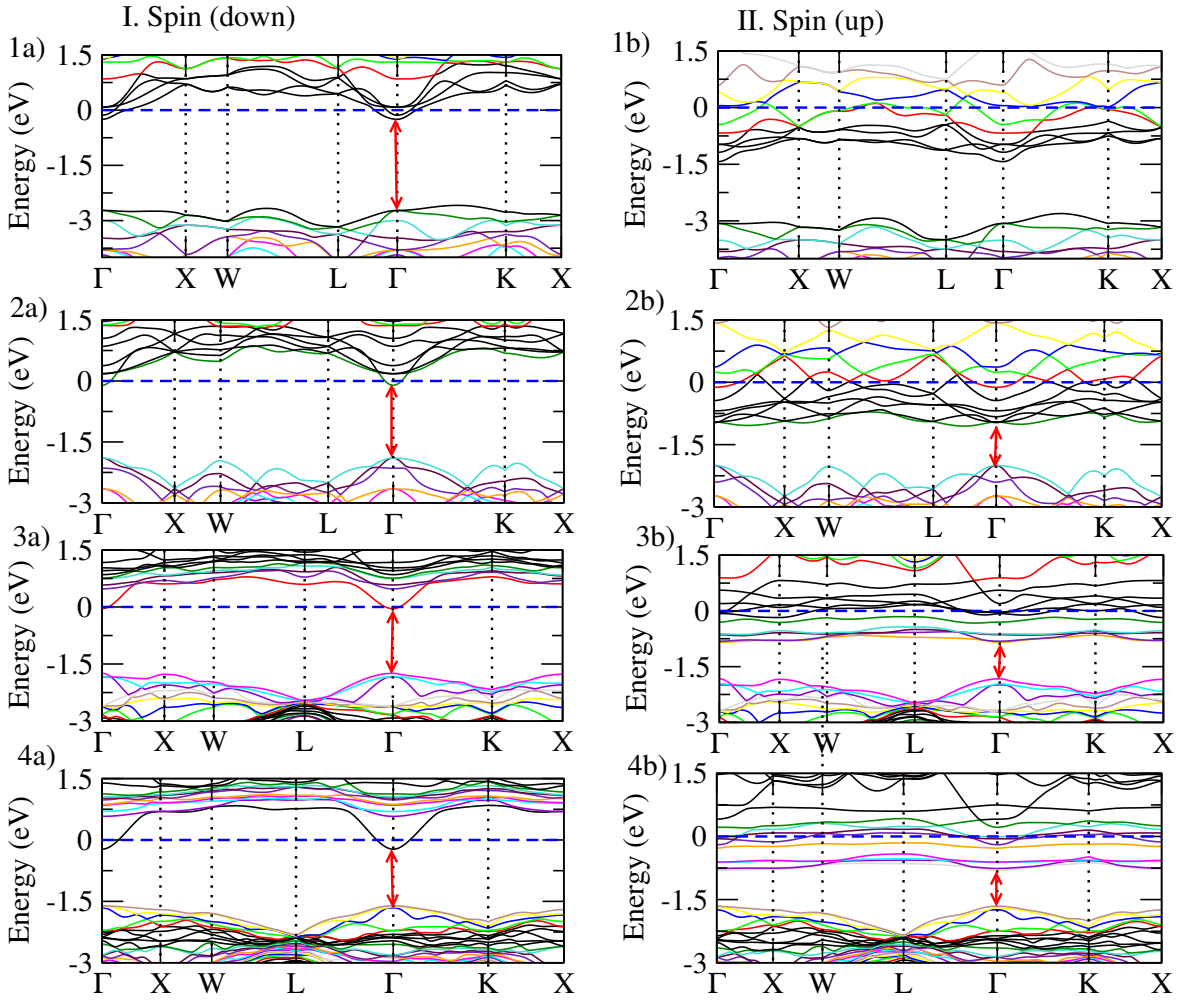

Figure 27: The spin-polarized band structure of spin down (minority spin) (I) and spin up (majority) (II) systems 1) $Zn_{0.5}V_{0.5}Se$ 2) $Zn_{0.75}V_{0.25}Se$, 3) $Zn_{0.875}V_{0.125}Se$ and 4) $Zn_{0.917}V_{0.083}Se$ respectively using LDA approximation

B. Spin-Polarized Density of States $Zn_{(1-x)}(Fe,V)_xSe$ Systems

The total density of state ferromagnetic (FM) and antiferromagnetic (AFM) systems is computed independently for $Zn_{0.5}Fe_{0.5}Se$, $Zn_{0.75}Fe_{0.25}Se$, and $Zn_{0.875}Fe_{0.125}Se$ using GGA and GGA+U approximations. The computation clearly revealed that there is a substantial difference between the majority (spin down) and minority (spin up) states, both in magnitude and in the number of added peaks near the Fermi level, for Fe-doped ZnSe systems with concentrations of 12.5%, 25 % and 50%. In the ferromagnetic case, the majority channel (spin down) and minority channel (spin up) are anti-symmetric, confirming that they have magnetic properties. However, in Figure 29 (see 1b, 2b, and 3b), the spin polarization is symmetric, which indicates that the antiferromagnetic (AFM) system has non-magnetic properties or does not show double exchange coupling behavior. Furthermore, the materials have a relatively higher effective mass, and the Fermi level is near the valence band. All materials are p-type semiconductors as a result of the GGA+U

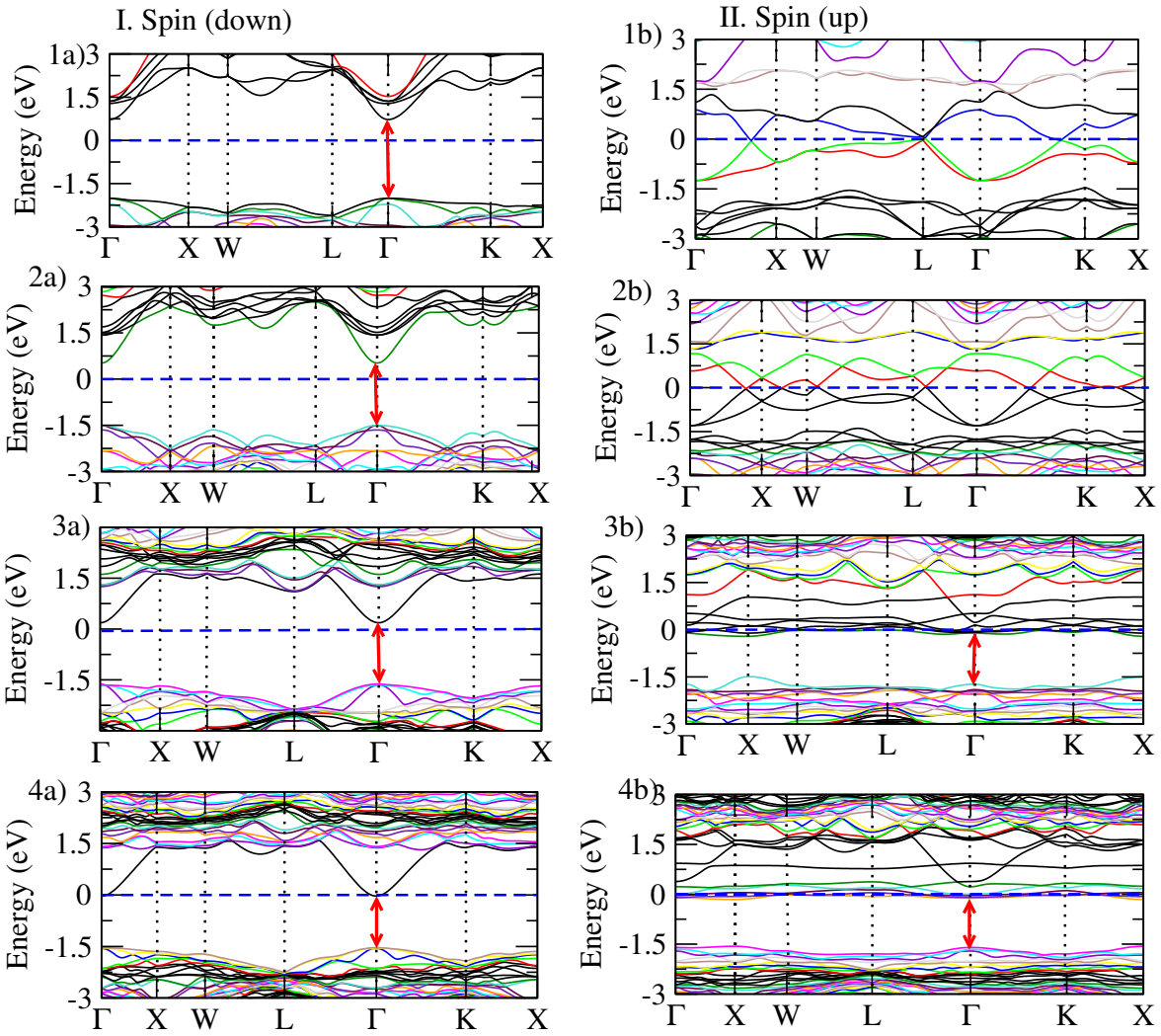

Figure 28: The spin-polarized band structure of spin down (minority spin) (I) and spin up (majority) (II) systems 1) $Zn_{0.5}V_{0.5}Se$ 2) $Zn_{0.75}V_{0.25}Se$, 3) $Zn_{0.875}V_{0.125}Se$ and 4) $Zn_{0.917}V_{0.083}Se$ respectively using LDA+U approximation

approximation for both spin channels. In the case of 12.5% doping of an impurity atom in ZnSe, the degeneracy is clearly observed in a majority spin channel. From Figure 30, the second nearest neighbor configuration calculation of the density of states also reveals that the magnetic property persists only in ferromagnetic systems. The overlapping of iron atoms 3d states on the top of the valance band is clearly observed in the case of 25% doping. Since the Fermi level moves deeper into the valance band, the system degenerates, and it is metallic for both channels. On the other hand, we can see that at 12.5% the Fermi level scratches the top of the valance band for minority spin channels while it lies in the valance band for majority spin channels. As a result, the material in this instance can be thought of as having half-metallic characteristics. The total density of the state ferromagnetic spin-polarized system is computed for $Zn_{(1-x)}Tm_xSe$ (Tm = Fe, V) as shown in Figure 31, 32, 33 and 34 using LDA and LDA+U approximations. In Figure 31, we used the LDA approximation to calculate the total density of states (TDOS) for both ferromagnetic and

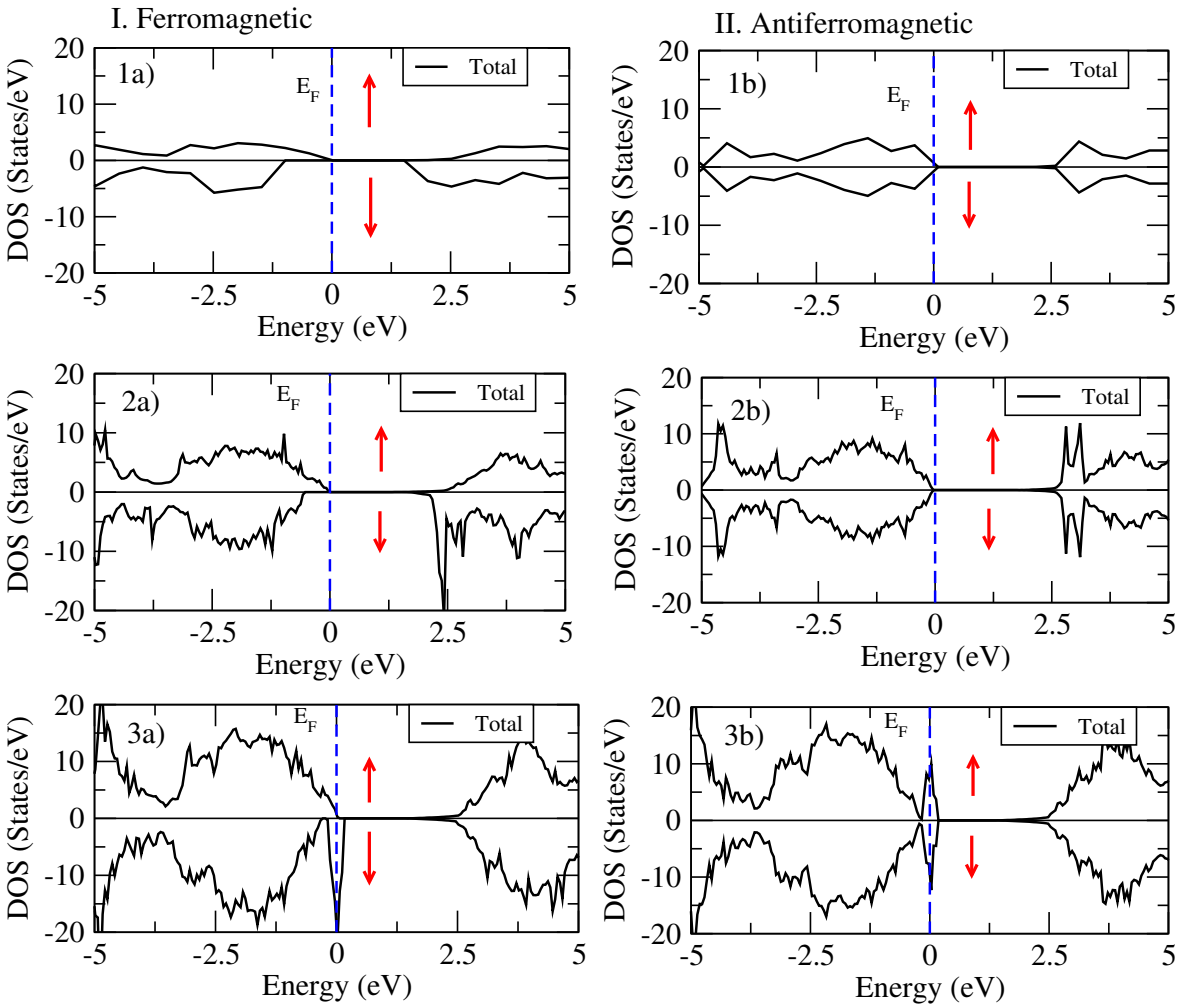

Figure 29: Total density of states of ferromagnetic systems a) and antiferromagnetic systems b) 1) $Zn_{0.5}Fe_{0.5}Se$ 2) $Zn_{0.75}Fe_{0.25}Se$ 3) $Zn_{0.875}Fe_{0.125}Se$ respectively, using the GGA+U approximation

antiferromagnetic systems as indicated in column(I) and column(II), respectively. The computation clearly showed that there is a substantial difference between the majority spin (spin down) and minority spin (spin up) states both in magnitude and number of added peaks near the Fermi level. The anti-symmetric properties in ferromagnetic systems (see Figure 31 1a,2a,3a,4a) confirm that the materials have magnetic properties while null spin polarization and symmetric spin channels in antiferromagnetic systems (see Figure 31 1b,2b,3b,4b) indicate that the material has no magnetic properties. Furthermore, these materials have half-metallic electronic properties with antiferromagnetic behavior.

Figure 32, the LDA+U approximation is used to calculate the total density of states in both systems. In this case, the ferromagnetic system calculation significantly reveals the magnetic properties of the materials. Both the majority and minority spin channels exhibit semiconducting properties with clear band gaps. Hence, the LDA +U approximation confirms that materials: $Zn_{0.5}Fe_{0.5}Se$ and $Zn_{0.75}Fe_{0.25}Se$ are semiconducting materials with antiferromagnetic properties, while $Zn_{0.875}Fe_{0.125}Se$ is a half-metallic with localized states formed due to overlapping of iron atom 3d states at the top of the valance band in a spin

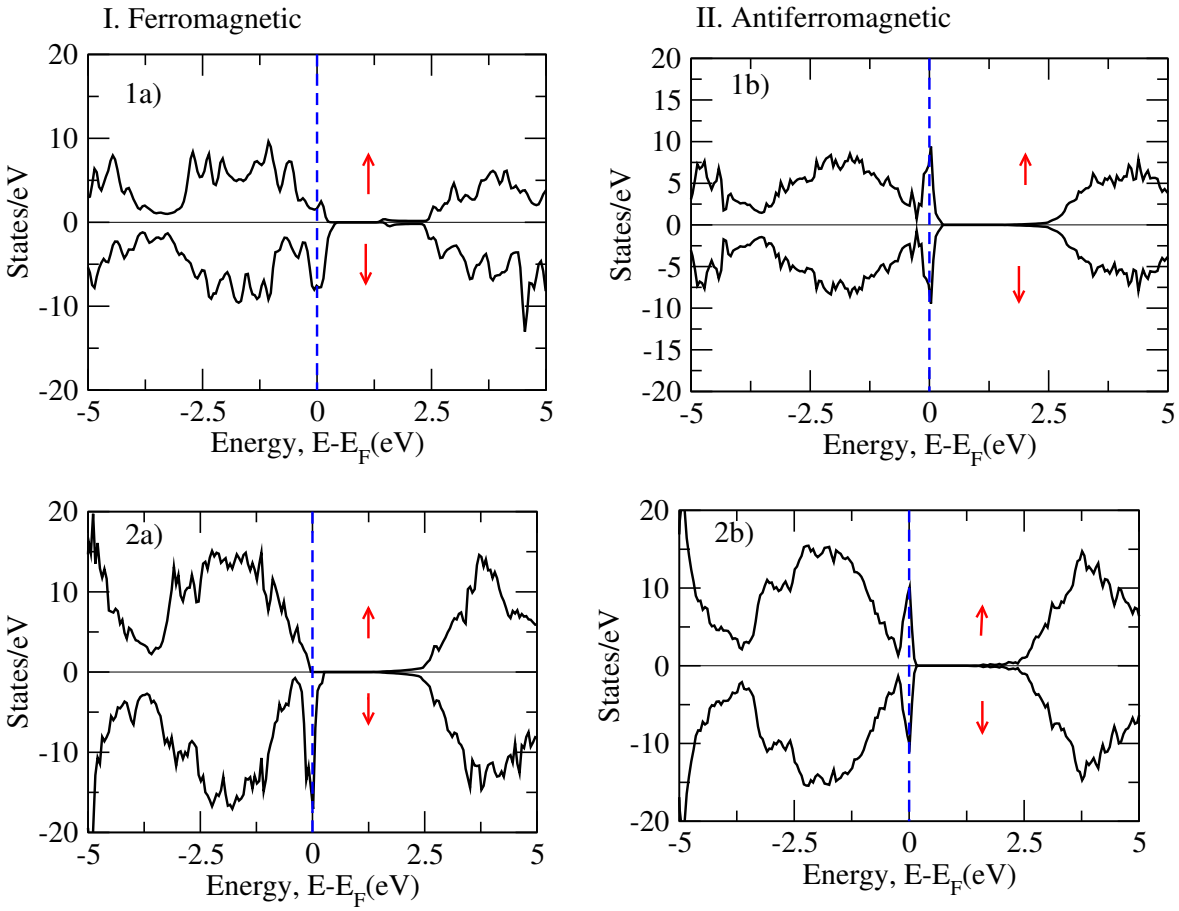

Figure 30: Total density of states of ferromagnetic system a) and antiferromagnetic system b) 1) $Zn_{0.75}Fe_{0.25}Se$ 2) $Zn_{0.875}Fe_{0.125}Se$, respectively, with the second nearest neighbor configuration (NN) of dopant atoms using the GGA+U approximation

majority channels.

On the other hand, as illustrated in Figure 33, the LDA approximation is used to calculate the ferromagnetic and antiferromagnetic total density of states (TDoS), $N(E)/eV$ for vanadium-doped ZnSe systems. The calculation of the ferromagnetic system revealed that the vanadium-doped ZnSe materials have magnetic properties, while the null spin polarization in an antiferromagnetic plot shows that it does not give the magnetic properties of the materials. Figure 33 a), shows that all the minority spin channels are n-type semiconductors while the majority spin channels are metallic; hence, materials are half-metallic with ferromagnetic properties, which also agrees with reports (Behloul et al., 2016).

From Figure 34, it is confirmed that the ferromagnetic arrangements display large changes in minority and majority channel densities of states, both in number of peaks and magnitude near the Fermi level (See Figure 34 1a, 2a, 3a, and 4a). In this scenario, however, as shown in Figure 34 1a, 2a, 3a, and 4b, the anti-ferromagnetic arrangement of the sample results in a symmetric density of states in both channels which indicates there is no magnetic property is observed in this arrangement. Hence, the LDA+U calculation of the

ferromagnetic system confirms the material has magnetic properties. Still, it shows the materials are half metal with an enhanced band gap in a minority spin channel.

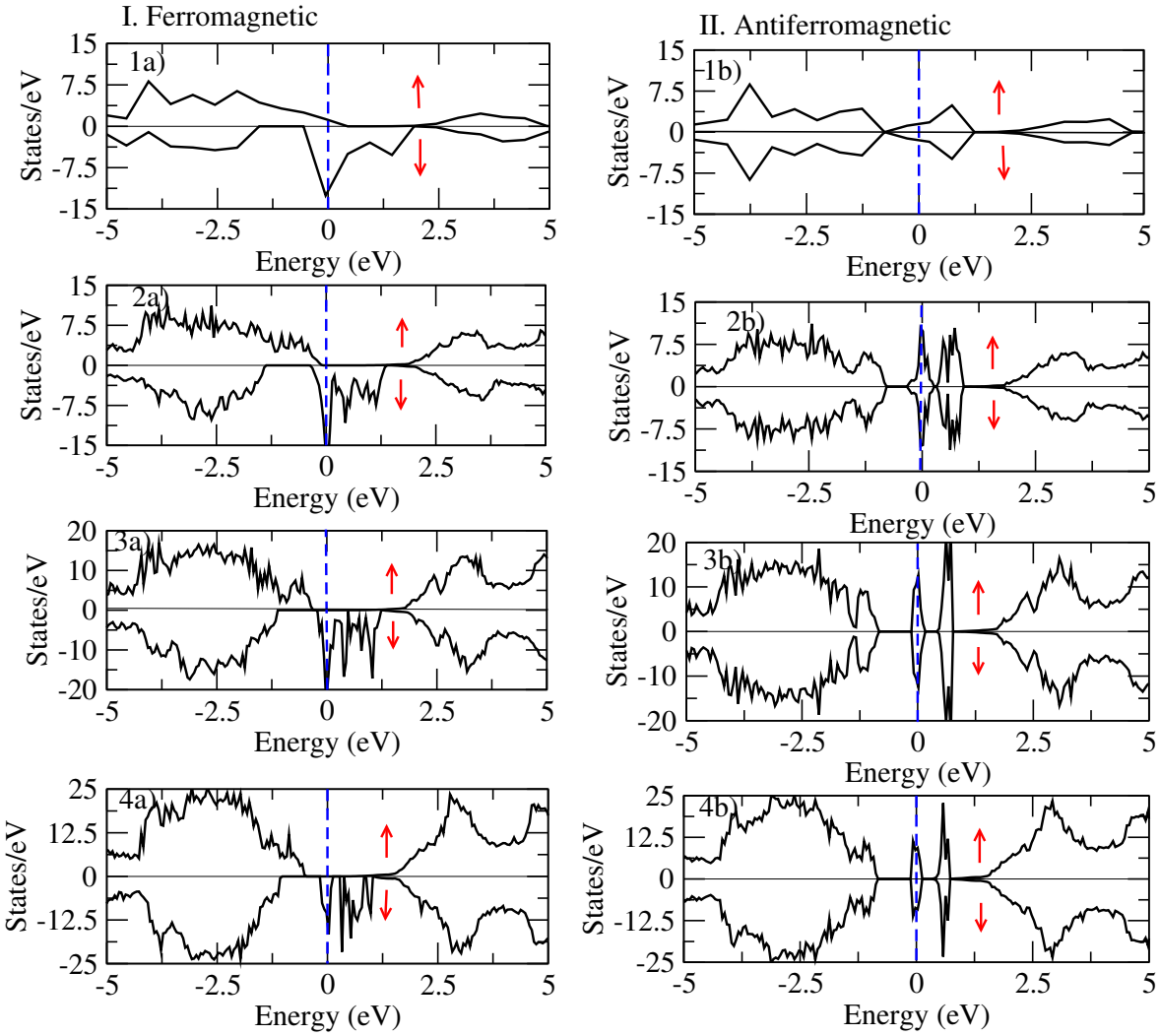

Figure 31: Total density of states of ferromagnetic system I) and antiferromagnetic system II) of 1) $Zn_{0.5}Fe_{0.5}Se$ 2) $Zn_{0.75}Fe_{0.25}Se$, 3) $Zn_{0.875}Fe_{0.125}Se$ and 4) $Zn_{0.9375}Fe_{0.0625}Se$ respectively, using LDA approximation

C. Spin-Polarized Band Structures of $Zn_{(1-x)}Fe_xSe_yTe_{(1-y)}$ System

In this section, we calculated the spin-polarized band structure of $Zn_{(1-x)}Fe_xSe_yTe_{(1-y)}$ (for x = 0.5, 0.25, 0.125, and y = 0.25, 0.125, and 0.0625, respectively) to investigate its electronic and magnetic properties. A spin-polarized structure provides summary information on the energy levels of electrons in a material, as well as their dispersion, or change in energy, as a function of the wave vector for electrons with opposite spins. The band gaps for spin-up and spin-down (majority spin channel) bands differ, as illustrated in Figure 35 (1-3), demonstrating that the magnetic behaviors in this alloy are clearly visible. The material's magnetic characteristics are demonstrated by an imbalance between the spin-up and spin-down populations. Furthermore, the material is n-type degenerate based on the band structure

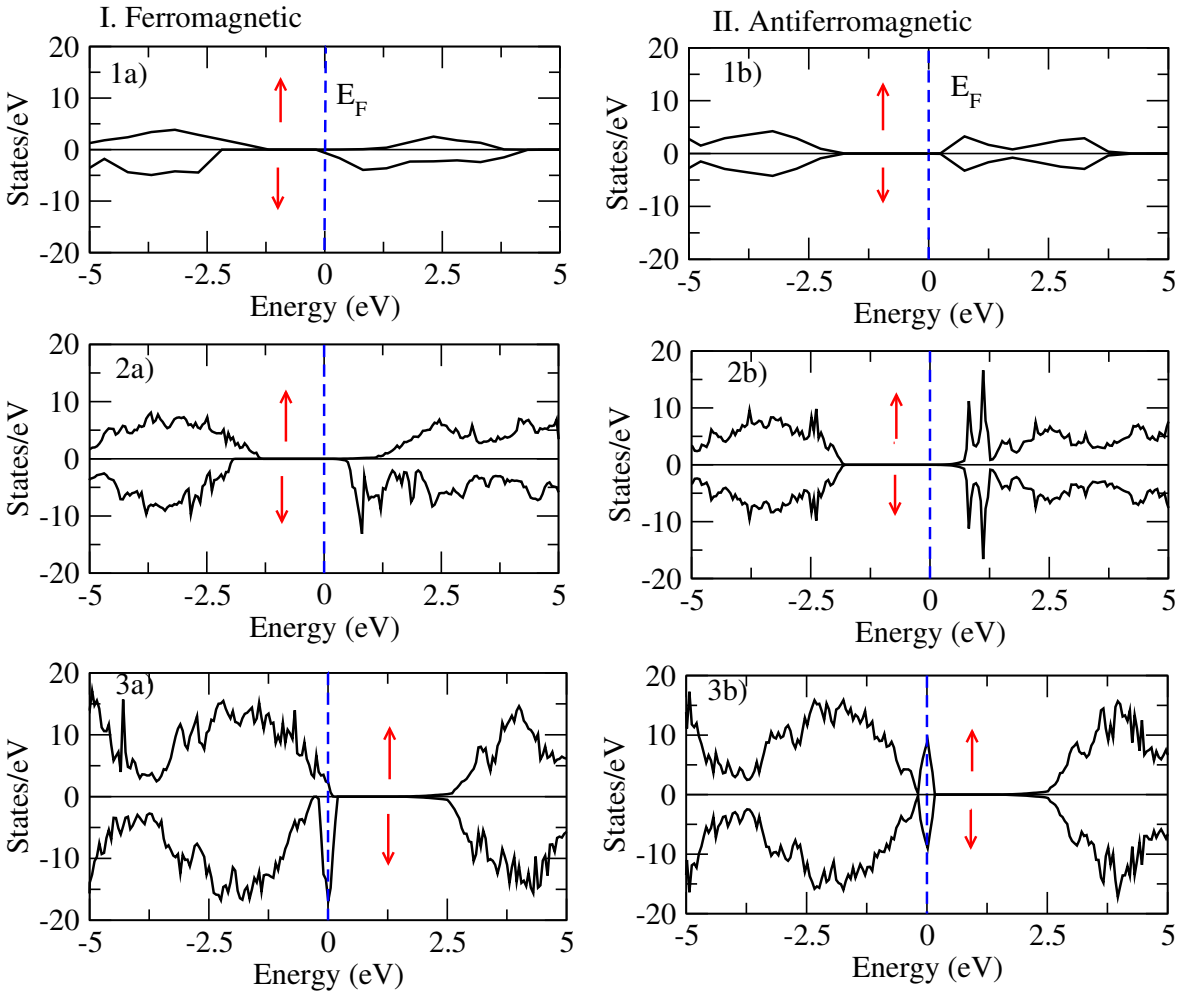

Figure 32: Total density of states of ferromagnetic system I) and antiferromagnetic system II) 1) $Zn_{0.5}Fe_{0.5}Se$ 2) $Zn_{0.75}Fe_{0.25}Se$ 3) $Zn_{0.875}Fe_{0.125}Se$, respectively using LDA+U approximation

of the majority of spin channels. When the iron concentration is high enough, up to 50% of the majority spin channel exhibits an n-type degenerate indirect band structure with metallic characteristics. When the iron content declines, the Fermi level gradually decreases to the conduction band edge (see Figure 35, I). In the case of minority spin channels, the material exhibits a p-type degenerate direct band gap when the iron concentration surpasses 50%, but it transforms into a p-type direct band gap semiconductor with clear band gaps between the valance and conduction bands (see Figure 35 II).

In Figure 36, the LDA+U approximation revealed that the difference in the position of Fermi level and band structure is clearly observed. When x = 0.5 and y = 0.25, the majority of the spin channel is n-type, while the spin-up system is a p-type semiconductor. For x = 0.25 and y = 0.125, both channels are turned into metallic with the spin-up system, which is a p-type degenerate system. As x = 0.125 and y = 0.065, both channels become p-type systems, with the Fermi level deeper in the valance band in the majority spin channel than in the spin-up system.

The spin-polarized band structure calculation for the next nearest neighbor (NN)

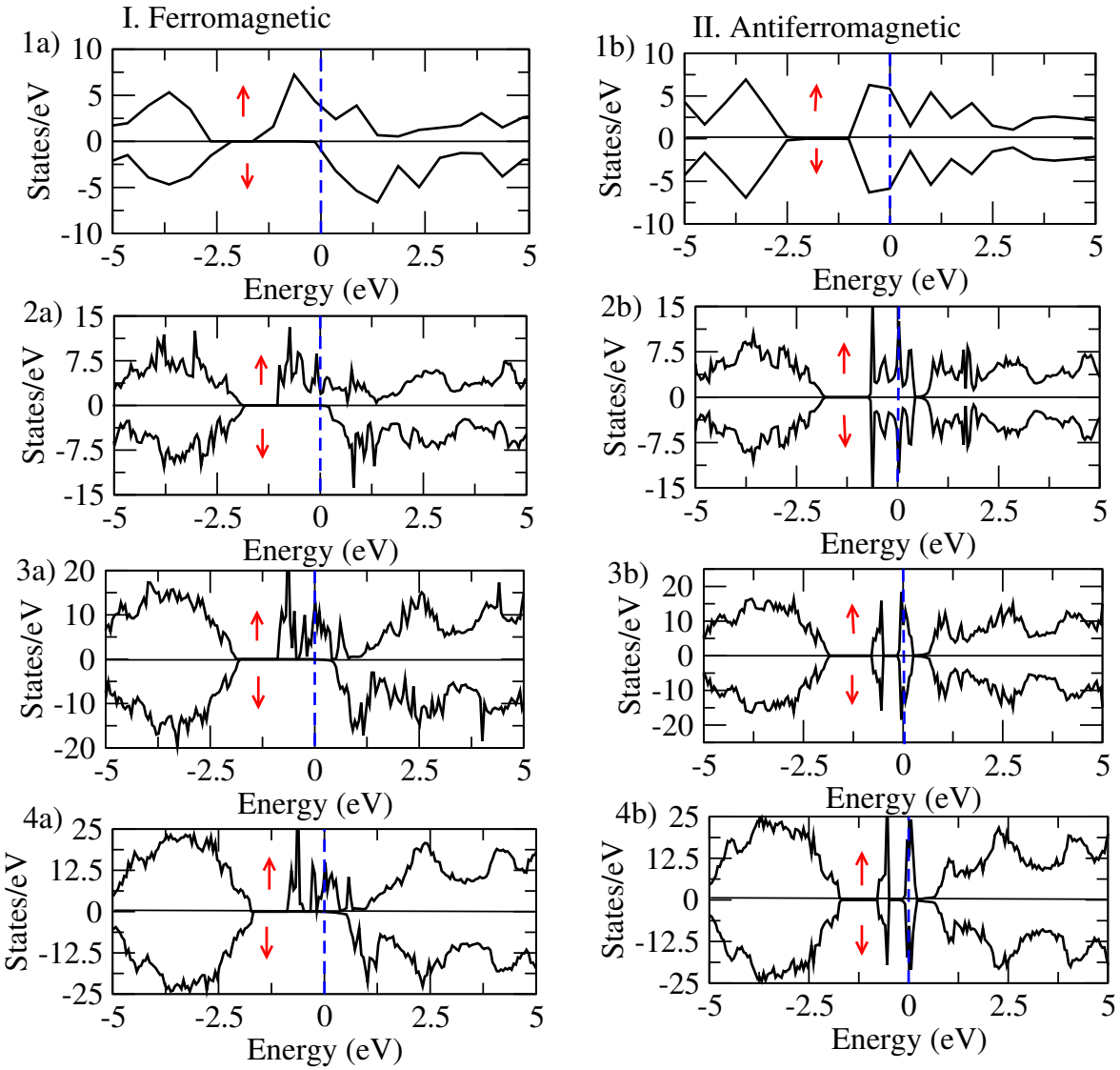

Figure 33: Total density of states of ferromagnetic system I) and antiferromagnetic system II) 1) $Zn_{0.5}V_{0.5}Se$, 2) $Zn_{0.75}V_{0.25}Se$, 3) $Zn_{0.875}V_{0.125}Se$ and 4) $Zn_{0.917}V_{0.083}Se$, respectively using LDA approximation

configuration of the magnetic atom in the $Zn_{0.75}Fe_{0.25}Se_{0.125}Te_{0.875}$ system revealed remarkable results in both LDA and LDA+U approximations, as illustrated in Figure 37. The LDA approximation (see Figures 37 1a and 1b) indicates that the system is metallic; the Fermi level is at localized states in a spin-down system, whereas p-type degeneracy is observed in a minority spin channel. In the case of the LDA+U approximation, the material clearly exhibits half-metal ferromagnetic behavior, which is a remarkable result that this material has the possibility of applicability in spintronics devices.

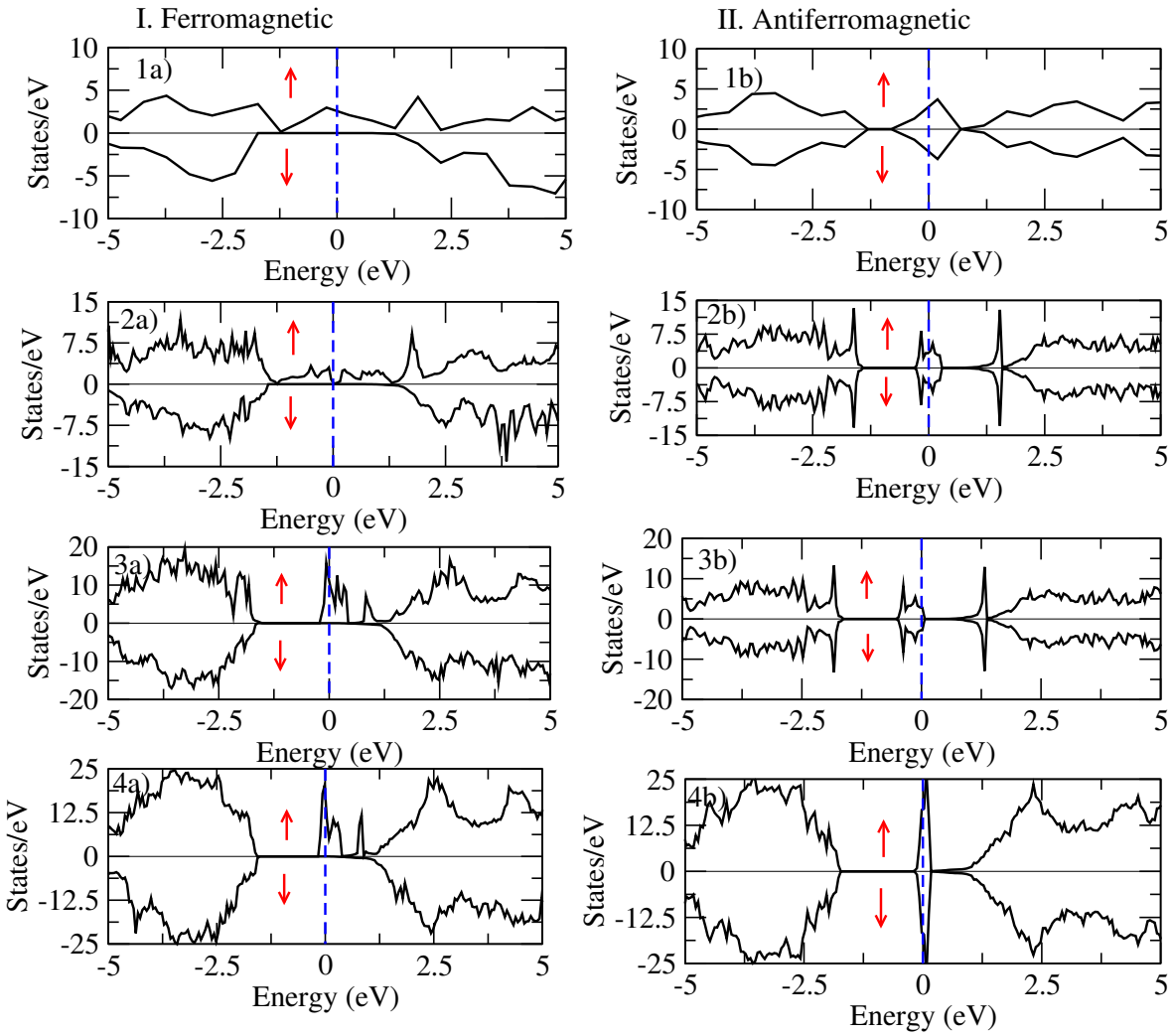

Figure 34: Total density of states of ferromagnetic system I) and antiferromagnetic system II) 1) $Zn_{0.5}V_{0.5}Se$, 2) $Zn_{0.75}V_{0.25}Se$, 3) $Zn_{0.875}V_{0.125}Se$ and 4) $Zn_{0.917}V_{0.083}Se$ respectively using LDA+U approximation

Table 7: The spin polarized band gap (E_g) and Fermi energy (E_F) for various spin polarized $Zn_{(1-x)}Fe_xSe_yTe_{(1-y)}$ systems using the LDA and LDA+U approximations.

Functional	x, y	**Conf.**	$E_F(eV)$	**Spin(dn)**,E_g (eV)	**Spin(up)**,E_g (eV)
	0.5, 0.25	N	7.2769	0.9312	0.641
LDA	0.25, 0.125	N	7.5476	0.6717	0.8485
		NN	7.5710		
	0.125, 0.0625	N	7.7343	0.5825	0.9875
		NN	7.7388		
	0.5, 0.25	N	7.4765	2.0437	1.131
LDA+U	0.25, 0.125	N	7.0145		1.0671

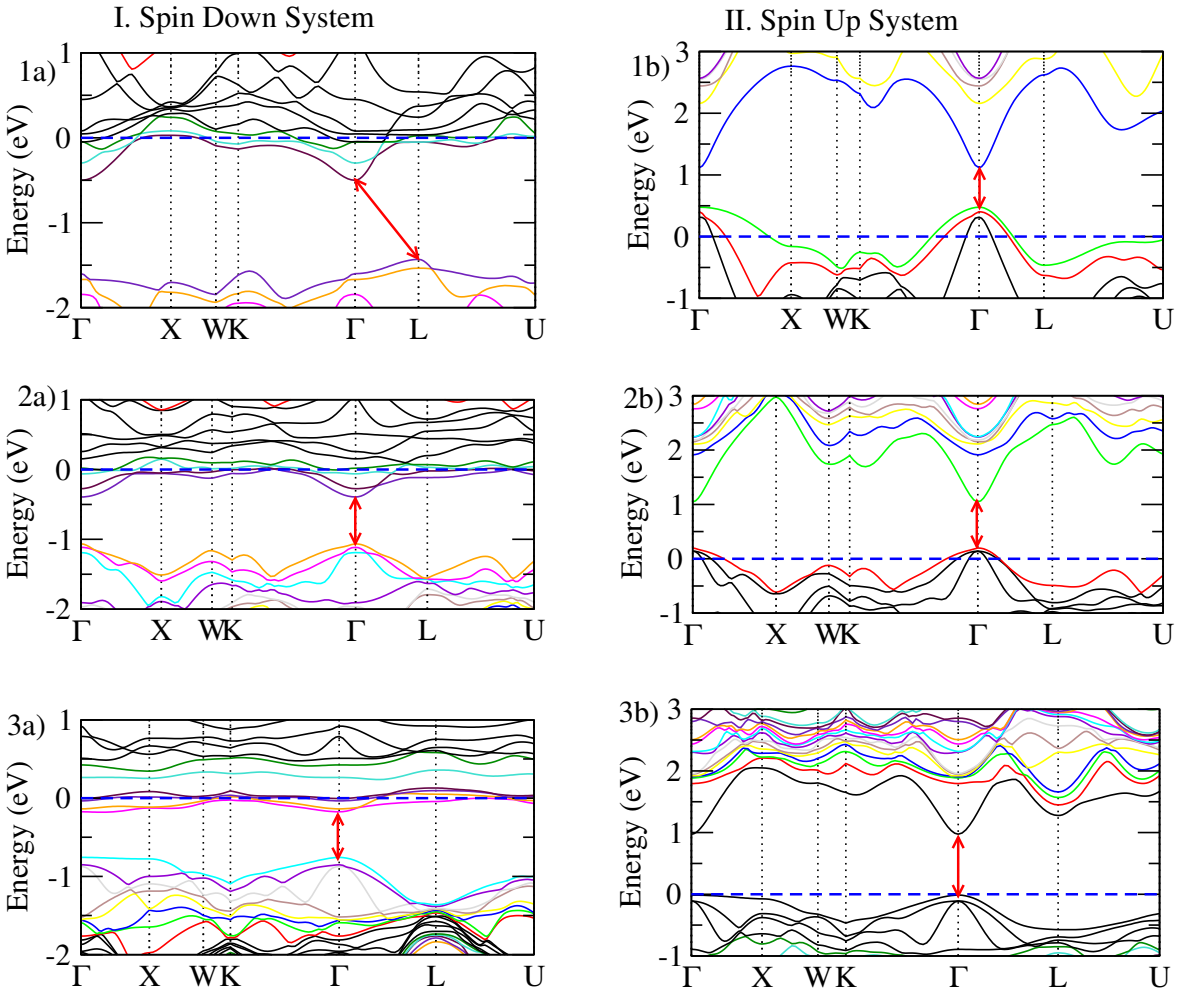

Figure 35: The spin-polarized band structure of both channels, spin down (majority channel) (I) and spin up (minority channel) (II), 1) $Zn_{0.5}Fe_{0.5}Se_{0.25}Te_{0.75}$ 2) $Zn_{0.75}Fe_{0.25}Se_{0.125}Te_{0.875}$ and 3) $Zn_{0.875}Fe_{0.125}Se_{0.0625}Te_{0.9375}$ using LDA approximations

D. Spin-Polarized Density of States of $Zn_{(1-x)}Fe_xSe_yTe_{(1-y)}$ System

In this section, we performed the spin-polarized density of states calculations for $Zn_{(1-x)}Fe_xSe_yTe_{(1-y)}$ (for x = 0.5, 0.25, 0.125, and y = 0.25, 0.125, and 0.0625, respectively) to observe the effect of iron on $ZnSe_yTe_{(1-y)}$ electronic and magnetic properties using LDA and LDA+U approximations. As seen in Figure 39, the partial density of states is plotted in the energy range of -5 eV to 5 eV using LDA approximation. From Figure 39 a) (1-3), we clearly see that there is a significant difference in number and magnitude in the density of states of minority and majority spin channels for the iron concentrations of 12.5%, 25%, and 50%. This anti-symmetric property of their density of states confirms that these systems can exhibit magnetic properties when their spins are ordered in a ferromagnetic arrangement. So, systems exhibit relatively strong magnetic properties. However, from Figure 39b) (1-3), the density of states in both channels is symmetric, and this confirms that anti-ferromagnetic arrangements of spins in the system do not give any magnetic properties and do not show double exchange coupling behavior. We

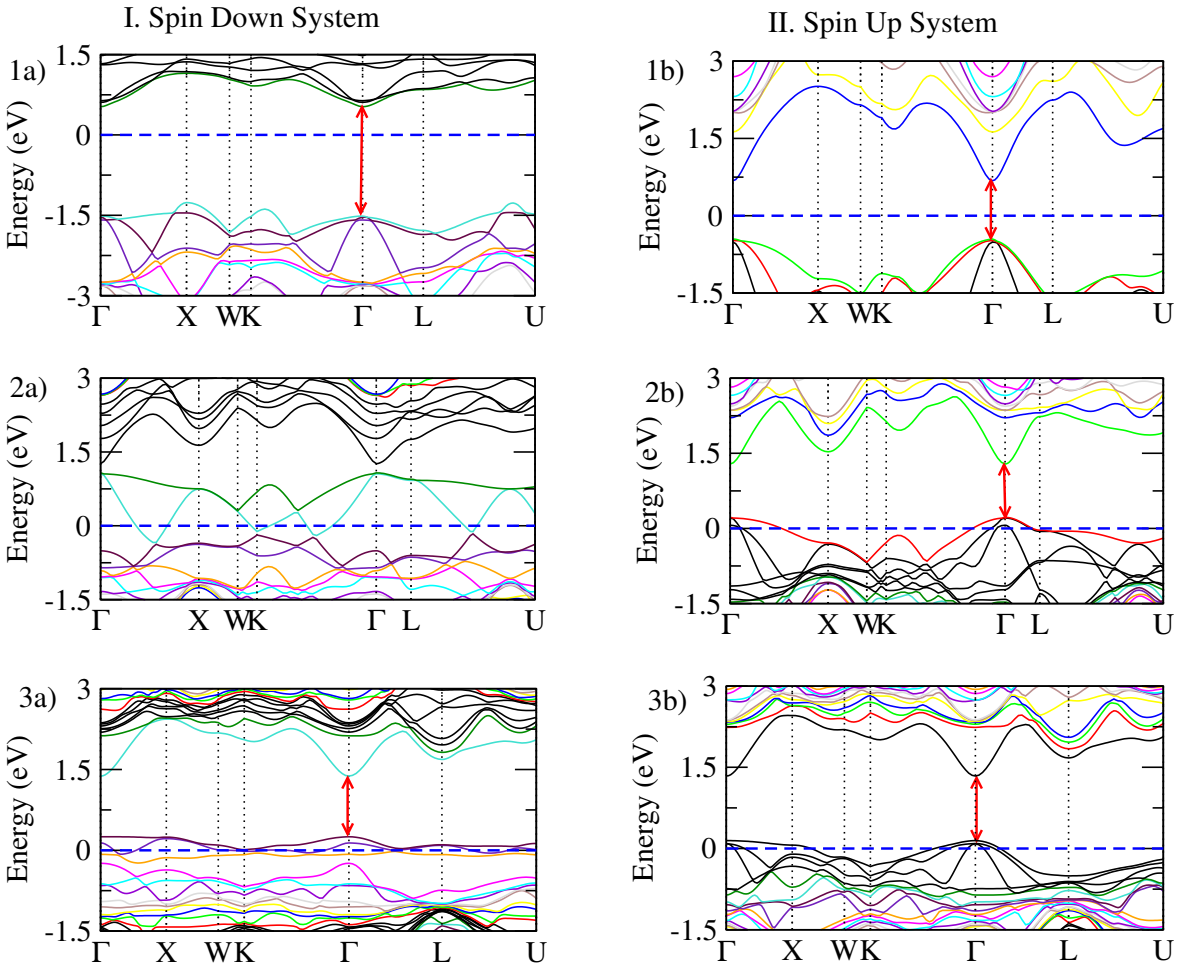

Figure 36: The spin-polarized band structure of both channels, spin down (majority channel) (I) and spin up (minority channel) (II), 1) $Zn_{0.5}Fe_{0.5}Se_{0.25}Te_{0.75}$ 2) and $Zn_{0.75}Fe_{0.25}Se_{0.125}Te_{0.875}$ 3) $Zn_{0.875}Fe_{0.125}Se_{0.0625}Te_{0.9375}$ using LDA+U approximations

can also see from Figure 38, that the system tends to be magnetic when its arrangements are in a ferromagnetic order, and it exhibits that the system tends to be dilute magnetic material as the iron concentration decreases.

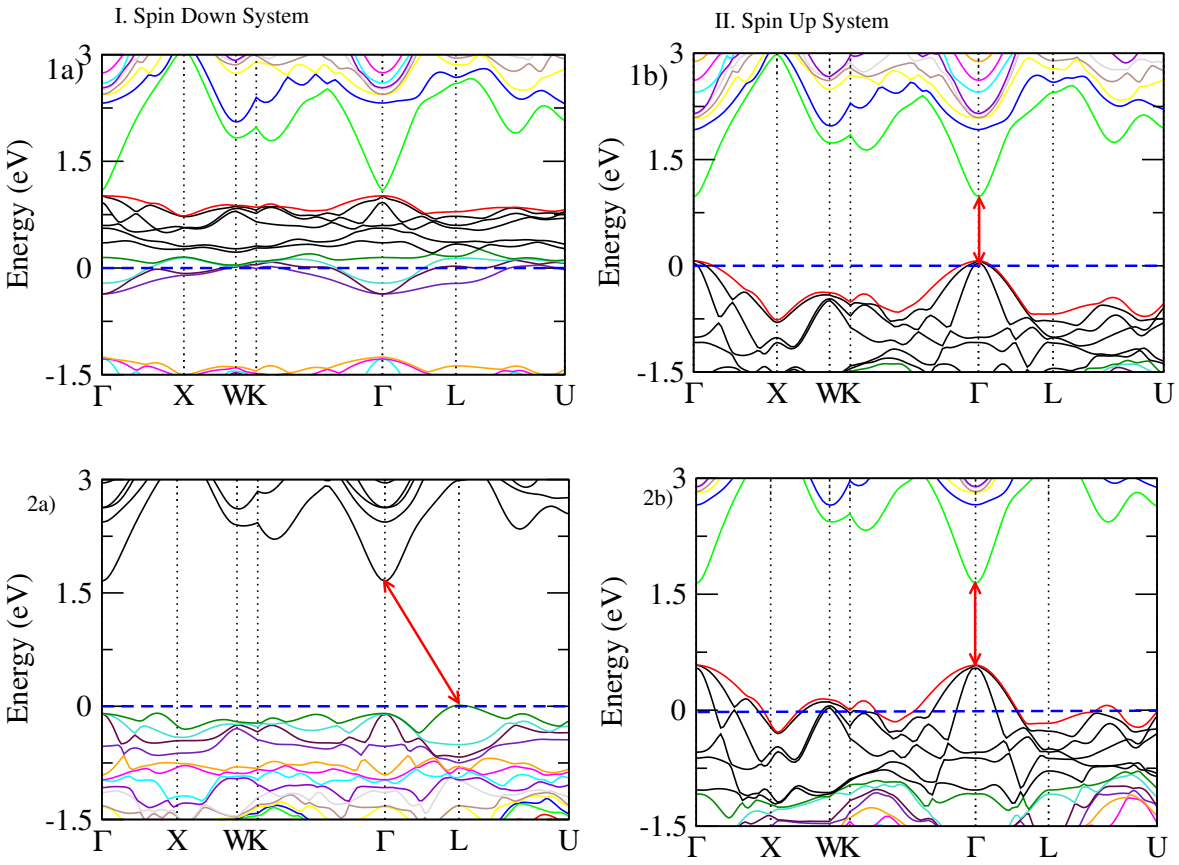

Figure 37: The spin-polarized band structure next nearest neighbors (NN) configuration of both channels is spin down (majority channel) (I) and spin up (minority channel) (II) for $Zn_{0.75}Fe_{0.25}Se_{0.125}Te_{0.875}$ using 1) LDA and 2) LDA+U approximations

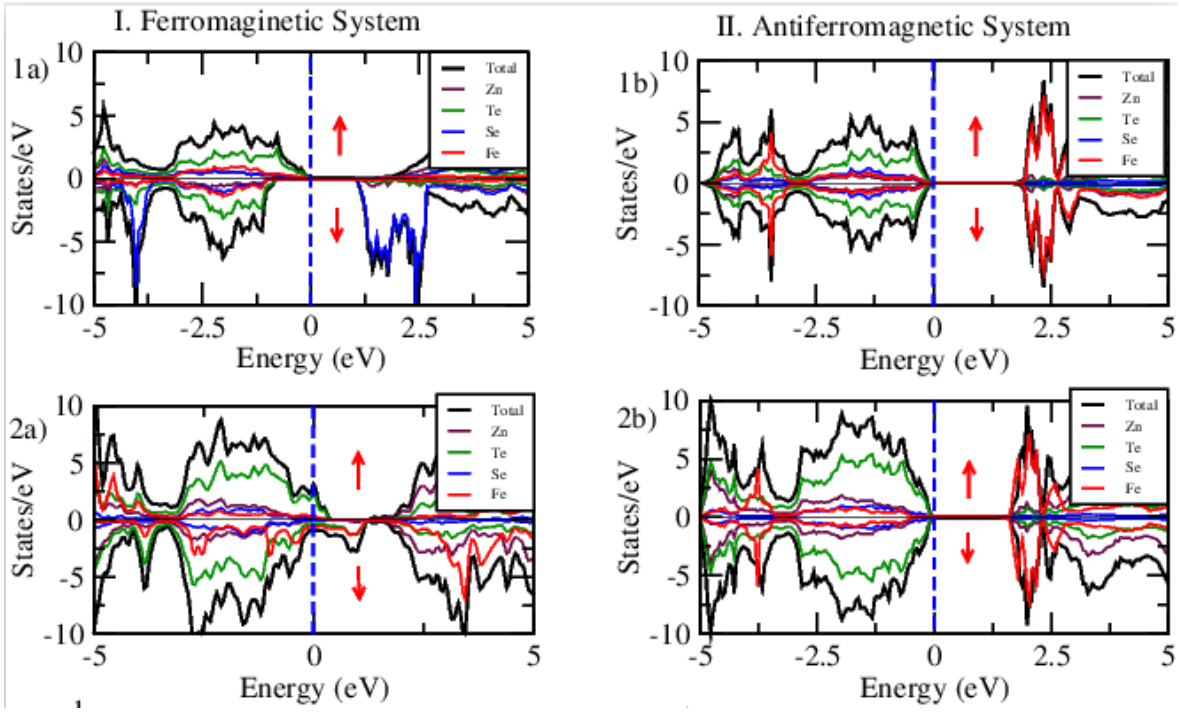

Figure 38: The partial density of states of a) ferromagnetic and b) antiferromagnetic systems of 1) $Zn_{0.5}Fe_{0.5}Se_{0.25}Te_{0.75}$ and 2) $Zn_{0.75}Fe_{0.25}Se_{0.125}Te_{0.875}$ using LDA+U approximations

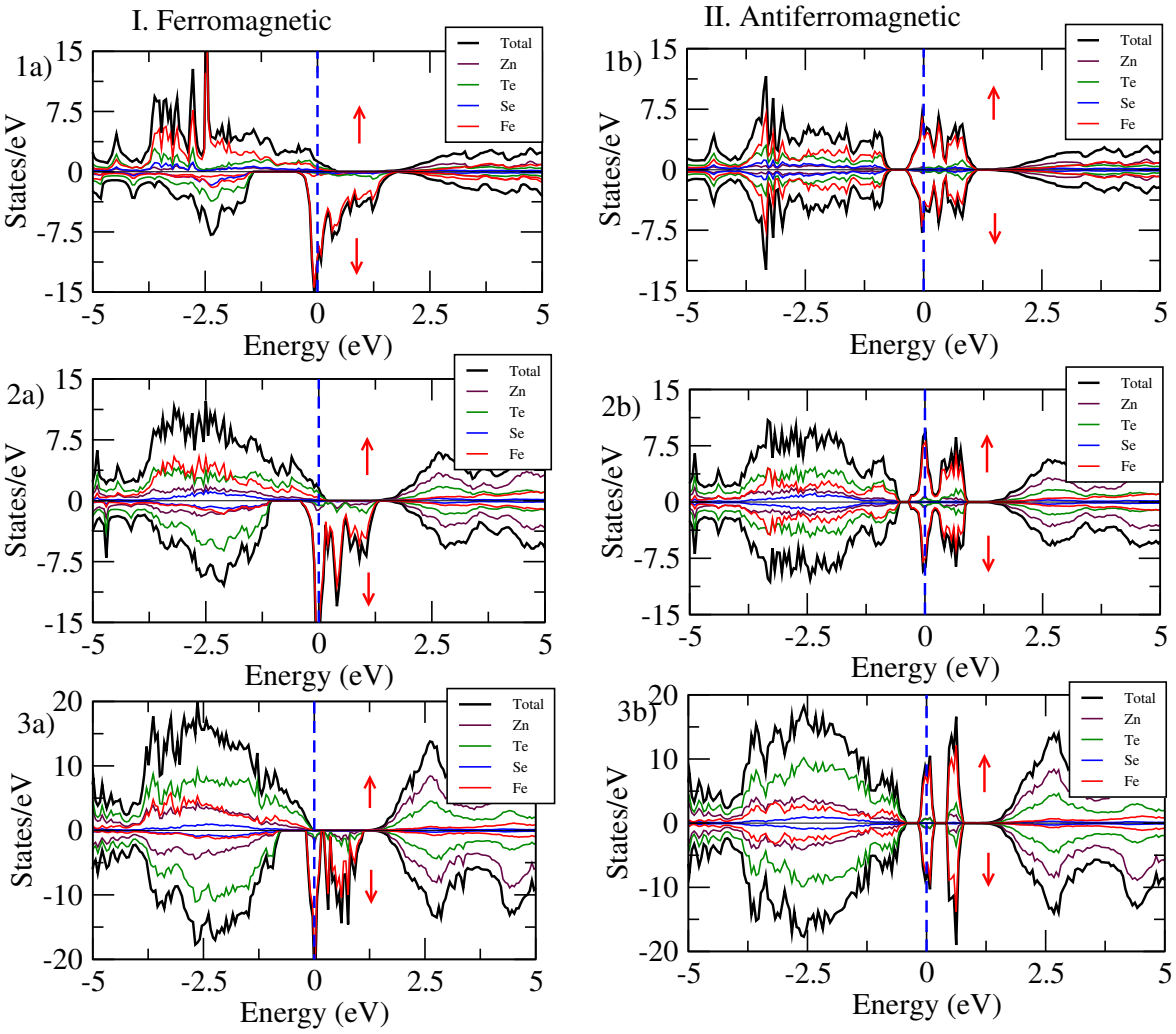

Figure 39: The partial density of states of a) ferromagnetic and b) antiferromagnetic systems of 1) $Zn_{0.5}Fe_{0.5}Se_{0.25}Te_{0.75}$ 2) $Zn_{0.75}Fe_{0.25}Se_{0.125}Te_{0.875}$ and 3) $Zn_{0.875}Fe_{0.125}Se_{0.0625}Te_{0.9375}$ using LDA approximations

4.4. Magnetic Properties $Zn_{(1-x)}$(Fe, V)$_x Se_y Te_{(1-y)}$ System

A. Magnetic Interaction of Dopants in the $Zn_{(1-x)}$(Fe, V)$_x$Se System

From the magnetic calculation, we can obtain the total magnetization and absolute magnetization for the different iron-doped zinc selenide systems. The magnetic property analysis is done with the help of the total energy difference between the ferromagnetic (FM) and antiferromagnetic (AFM) spin-polarized calculations as well as the magnetic moment of the systems. In a simple ferromagnetic material, the absolute magnetization and total magnetization should be equal, whereas in an antiferromagnetic system, the total magnetization is zero and the absolute is twice the magnetization of each of the two atoms in the system, which almost agrees with the results of this study as in Table 8. Since the experimental magnetic moment of the iron is $3\mu_B$, the result of this study agrees with it (Billas et al., 1994; Pike et al., 2022; Chen et al., 2015; Kulyuk et al., 2010). And also, it

well agrees with the previous reports (Behloul et al., 2016; Chen et al., 2015; Mermin and N.David, 1976).

The stability and coupling can be estimated from the ground energy difference between the ferromagnetic and antiferromagnetic states according to the following equation:

$$\Delta E = E_T(FM) - E_T(AM), \tag{4.3}$$

where, ΔE, the difference between ferromagnetic and anti-ferromagnetic total energy, $E_T(FM)$ is the total energy of the ferromagnetic system, and $E_T(AM)$ is also the total energy of the antiferromagnetic system. The charge and total magnetic moment of all systems are read from the output file of the self-consistent calculations as shown in Table 8

Table 8: The average charge and moment per dopant site, the magnetic moment of the system (absolute and total), and coupling in Fe-doped zinc selenide for different configurations

Functional	x	**conf.**	**Charge(A/F)**	μ_B(A/F)	**Moment,$\mu(\mu_B)$**	
					Absolute(A/F)	Total(A/F)
	0.5	N	14.16/14.15	3.01/3.16	6.7/7.70	0.0/7.70
GGA	0.25	N	14.17/14.15	3.01/3.17	6.74/7.83	0.0/7.83
		NN	14.16/14.15	3.13/3.17	7.57/7.97	0.0/7.96
	0.125	N	14.16/14.15	3.10/3.16	7.48/7.97	0.0/7.97
		NN	14.16/14.15	3.13/3.16	7.69/8.01	0.0/7.98
	0.5	N	14.06/14.06	3.51/3.54	7.71/8.05	0.0/8.00
GGA+U	0.25	N	14.06/14.06	3.51/3.55	7.72/8.06	0.0 /8.00
		NN	14.16/14.15	3.13/3.17	7.57/7.97	0.0/7.96
	0.125	N	14.14/14.14	3.37/3.30	7.59/7.63	0.0/7.41
		NN	14.14/14.14	3.31/3.30	7.65/7.67	0.0/7.43

The second nearest neighbor configuration of the dopant atoms in the 12.5% iron-doped ZnSe system exhibits stabilization in the ferromagnetic states. However, the other findings confirmed that ferromagnetic stabilization can occur for concentrations below 5% concentration of iron as a result of LDA approximation (Gromboni and Mascaro, 2016). As shown in Table 9, the magnetic states of the iron-doped ZnSe system are structurally more favorable than the nonmagnetic states of the system.

From the ferromagnetic and antiferromagnetic calculations, we obtained the total magnetization, absolute magnetization, and magnetic moments per dopant site for the vanadium and iron-doped zinc selenide systems. The magnetic property analysis is done with the help of the total energy difference between the ferromagnetic (FM) and antiferromagnetic (AFM) spin-polarized calculations as well as the magnetic moment of the systems. The calculated magnetic moment of iron agrees with the modes of this study. Since the experimental magnetic moment of the iron is 3 μ_B, the result of this study agrees with it (Billas et al., 1994; Mermin and N.David, 1976; Mann et al., 2016; Kulyuk et al.,

Table 9: The Comparison of the ground energies of nonmagnetic and ferromagnetic systems of iron-doped zinc selenide systems with different Configurations

Functional	**Composition** x	**Configuration**.	E_{tot}(Ry)	
			Nonmagnetic (NM)	**Ferromagnetic(FM)**
GGA	0.5	N	-1604.01	-1604.14
	0.25	N	-3622.59	-3622.72
		NN	-	-3622.72
	0.125	N	-7659.70	-7659.883
		NN	-	-7659.884
GGA+U	0.5	N	-1603.28	-1603.86
	0.25	N	-3621.82	-3622.42
		NN	-	-3622.27
	0.125	N	-7658.85	-7659.396
		NN	-	-7659.397

2010) as seen in Table 10. And also, it well agrees with the previous reports (Behloul et al., 2016; Chen et al., 2015; Chen et al., 2019). The magnetic moment of the vanadium atom is $2\mu_B$. Some literature claims that the magnetic moments of Fe and V can be obtained as $3.4\mu_B$ and $2.3\mu_B$ respectively, by using Hubbard parameters (Mann et al., 2016), which is still consistent with our results.

As described in Table 12 the magnetic energy difference of the iron-doped ZnSe system confirms that there is an antiferromagnetic and ferromagnetic property tunability depending on the concentration and configuration of the system. In the case of the LDA+U approximation, for concentrations of x = 0.25 and 0.125 with second nearest neighbor configurations, the iron-doped ZnSe becomes the ferromagnetic system. From Table 13, the magnetic energy difference of the vanadium-doped zinc selenide system indicates that it has a ferromagnetic coupling.

B. Estimation of Curie(Neel) Temperature, ($T_{c(N)}$)

Since the number of dopants is two and the estimated curie temperature, T_c^{MFA} is 17K, while the corrected temperature for a three-dimensional face-centered cubic lattice, T_c^{corr} = $0.8162T_c^{MFA}$ = 13.88K (Mermin and N.David, 1976). The Curie/Neel temperature and the corrected Curie/Neel temperature are calculated using equations (2.22) and (4.3) as in Table 11.

Table 10: The configuration of the system (nearest(N) and second nearest(NN) neighbor), the average charge and moment per dopant sites (antiferromagnetic(A)/ferromagnetic(F)) of vanadium and iron-doped zinc selenide

Functional	x	**Conf.**	**Charge** (C)		**Moment**,$\mu(\mu_B)$	
			Fe:ZnSe(A/F)	V:ZnSe(A/F)	Fe:ZnSe(A/F)	V:ZnSe(A/F)
	0.5	N	14.16/14.15	10.87/10.89	2.84/2.96	1.65/2.05
LDA	0.25	N	14.16/14.14	10.88/10.89	2.93/3.05	1.69/2.10
		NN	14.15/14.14	10.89/10.89	3.01/3.06	2.01/2.09
	0.125	N	14.16/14.14	10.89/10.89	2.93/3.06	1.97/2.10
		NN	14.15/ 14.15	10.89/10.89	3.02/3.05	2.04/2.08
	0.083	N	14.18/14.17	10.92/10.92	3.04/3.11	2.03/2.14
	0.5	N	14.06/14.05	10.88/10.89	3.44/3.48	2.39/2.46
LDA+U	0.25	N	14.06/14.05	10.88/10.89	3.44/3.48	2.39/2.46
		NN	14.13/14.14	10.88/10.89	3.25/3.22	2.43/2,44
	0.125	N	14.13/14.14	10.88/10.88	3.23/3.22	2.42/2.44
		NN	14.13/14.14	10.88/10.88	3.23/3.22	2.43/2.43

Table 11: The difference in total magnetic energy, configurations, coupling, and Curie/Neel temperature of Fe-doped zinc selenide configurations

Functional	**Composition**x	**Conf.**	ΔE (Ry)	**Coupling**	$T_c^{MFA}(K)$	$T_c^{cor}(K)$
	0.5	N	0.02322727	AFM	1222.4	997.7
GGA	0.25	N	0.02344861	AFM	1234	1007
		NN	0.00384055	AFM	202	164.9
	0.125	N	0.007174889	AFM	377.6	308
		NN	0.001832550	AFM	96.4	78.7
	0.5	N	0.012380160	AFM	651.5	531.8
GGA+U	0.25	N	0.011971649	AFM	630	514
		NN	0.003846789	AFM	220.4	165.2
	0.125	N	0.002479640	AFM	130.5	106.5
		NN	-0.000323079	FM	17	13.8

As shown in Table 11, the outcomes of these results revealed that the tunability among ferromagnetic and antiferromagnetic systems can be achieved by varying the percent of iron substitution instead of zinc in a ZnSe. The transition temperature decreases as the iron concentration reduces from 25% to 12.5%. Based on the change in total magnetic energy, the distance between dopants affects the magnetic property of the Fe-doped ZnSe system; as the distance increases, the system property tends to be ferromagnetic. We can also see that the distance affects the magnetic moment of the Fe atom and the transition temperature; this means that the dopant site is one of the major factors in obtaining the

room-temperature magnetic (RTM) properties. The concept of mean-field approximation (MFA) is used to estimate the Curie temperature (T_c) for the ferromagnetic system and the Neel temperature (T_N) antiferromagnetic system. The Curie/Neel temperature and the corrected Curie/Neel temperature are calculated using equation (2.22) as in Table 12 and 13 for all systems with two approximations. The result reveals that ferromagnetic properties exist for iron-doped ZnSe systems at very low temperatures, while for vanadium-doped ZnSe systems, it is possible to get ferromagnetic properties at different temperatures ranging from 52 K to 1919.7 K based on the type of functional used (LDA or LDA+U), configurations, and concentration of doping. This confirms the experimental results of iron and vanadium-doped ZnSe fabricated under as-grown crystal (Kulyuk et al., 2010) (antiferromagnetism of Fe-doped ZnSe) and epitaxial growth (ferromagnetism of V-doped ZnSe) (Sato and Katayama-Yoshida, 2002; Tahashi et al., 2009). As shown in Table 12, the outcomes of these

Table 12: The difference of total magnetic energy, configuration (N: nearest neighbor, NN: second nearest neighbor), coupling, and Curie/Neel temperature of iron-doped zinc selenide ($Zn_{(1-x)}Fe_xSe$) configurations

Functional	x	**Configuration**	ΔE (Ry)	**Coupling**	$T_N^{MFA}(K)$	$T_N^{cor}(K)$
LDA	0.5	N	0.026435569	AFM	1391.3	1135.6
	0.25	N	0.016816410	AFM	885	722.4
		NN	0.00531094	AFM	279.5	228.1
	0.125	N	0.016439170	AFM	865.2	706.2
		NN	0.00265196	AFM	139.6	113.9
	0.083	N	0.007414969	AFM	390.2	318.5
LDA+U	0.5	N	0.014564469	AFM	766.5	625.6
	0.25	N	0.01402594	AFM	738.2	602.5
		NN	-0.000722839	FM	38	31
	0.125	N	0.002876	AFM	151.4	123.7
		NN	-0.00042105	FM	22	18

results revealed that the tunability among ferromagnetic and antiferromagnetic systems can be achieved by varying the percent of iron substitution instead of zinc in a ZnSe. The transition temperature decreases as the vanadium and iron concentrations reduce from 25% to 8.3%. Based on the change in total magnetic energy, the distance between dopants affects the magnetic property of the Fe-doped ZnSe system. As the distance between dopants increases, the system property tends to be ferromagnetic. In the vanadium-doped case, the magnetic property is consistent with the variation of dopant concentration and distance between dopants, as shown in Table 13. Thus, these properties may make the vanadium-doped zinc selenide essential for spintronics devices since it is easy to obtain the room-temperature magnetic (RTM) properties.

Table 13: The difference of total magnetic energy, configuration and coupling, and ferromagnetic temperature of vanadium-doped zinc selenide ($Zn_{(1-x)}V_xSe$) configurations

Functional	x	**Configuration**	ΔE (Ry)	**Coupling**	$T_c^{MFA}(K)$	$T_c^{cor}(K)$
LDA	0.5	N	-0.01633207	FM	859.5	701.5
	0.25	N	-0.02044710	FM	1076.1	876.3
		NN	-0.00305877	FM	160.9	131.4
	0.125	N	-0.00953365	FM	501.7	409.7
		NN	-0.001213649	FM	63.9	52
	0.083	N	-0.0094493	FM	497.3	405.9
LDA+U	0.5	N	-0.042566089	FM	2240.2	1828.5
	0.25	N	-0.04468912	FM	2351.9	1919.7
		NN	-0.007455649	FM	392.4	320.3
	0.125	N	-0.01380199	FM	726.4	592.9
		NN	-0.00389084	FM	204.7	167
	0.083	N	-0.01244061	FM	654.7	534.4

C. Magnetic Interaction in $Zn_{(1-x)}Fe_xSe_yTe_{(1-y)}$ Systems

To determine the magnetic characteristics of $Zn_{(1-x)}Fe_xSe_yTe_{(1-y)}$, spin polarized calculations are done utilizing both approximations. The difference in total magnetic energies of magnetically ordered samples is used to explain the magnetic properties of the systems. The computed magnetic moment per iron atom is shown in Table 14 and is consistent with the experimental values, $3\mu_B$ (Billas et al., 1994; Mermin and N.David, 1976). The computed total and absolute magnetization are reported in Table 14 correspondingly. The magnetic stability and couplings can be deduced from the equation (4.3). The calculated results of Table 14 are read from the output of the self-consistent function of the magnetic samples for different concentrations.

Table 14: The average charge (C) and moment per dopant site, system magnetic moment (absolute and total), and coupling in Fe and Se co-doped zinc telluride systems (i.e., $Zn_{(1-x)}Fe_xSe_yTe_{(1-y)}$) for various configurations (conf.)

Fun'l	x, y	**Conf.**	**Charge(A/F)**	μ_B(A/F)	**Moment,μ(μ_B)** Absolute(A/F)	Total(A/F)
	0.5, 0.25	N	14.45/14.45	2.92/2.98	6.9/7.11	0.0/7.10
LDA	0.25, 0.125	N	14.50/14.49	2.88/2.93	6.71/7.34	0.0/7.29
		NN	14.45/14.45	3.04/3.06	7.21/7.59	0.0/7.58
	0.125, 0.0625	N	14.50/14.49	2.92/2.96	7.08/7.56	0.0/7.55
		NN	14.49/14.49	2.97/2.95	7.31/7.67	0.0/7.65
	0.5, 0.25	N	14.34/14.33	3.52/3.58	7.61/8.01	0.0/7.99
LDA+U	0.25, 0.125	N	14.38/14.51	3.49/3.15	7.73/7.34	0.0/7.29
		NN	14.55/14.56	2.85/2.81	6.50/6.67	0.0/5.21
	0.125, 0.0625	N	14.43/14.52	3.01/3.09	6.5/7.16	0.0/6.98
		NN	14,32/14.38	3.4/3.5	6.52/7.25	0.0/6.66

From Table 15, see that antiferromagnetic ordering systems are in more favorable states than non-magnetic because the magnetic states have the minimum total energy that the non-magnetic states.

Table 15: The favorable ground energies of nonmagnetic and magnetic stability in iron and selenide co-doped zinc telluride systems with various iron atom configurations

Functional	x, y	**Configuration**	**Non-magnetic (NM)**	E_{tot}(Ry) **Magnetic(AFM/FM*)**
	0.5, 0.25	N	-1476.05	-1476.16
LDA	0.25, 0.125	N	-2926.88	-2926.98
		NN	-	-2926.97
	0.125, 0.0625	N	-5828.52	-5828.63
		NN	-	-5828.62*
	0.5, 0.25	N	-1475.32	-1475.83
LDA+U	0.25, 0.125	N	-2926.035	-2926.6
		NN	-	-2926.53*
	0.125, 0.0625	N	-5827.61	-5828.16*
		NN	-	-5828.19*

To that purpose, using the mean-field theory and the difference between ferromagnetic and antiferromagnetic energy, the Curie temperature (Tc) of a structure $Zn_{1-x}Fe_xSe_yTe_{1-y}$ can

be computed (Tan et al., 2012) using equation (2.22). Since the mean field considers only isotropic magnetic moments in the material, which means it does not take into account fluctuations and correlations between individual moments, we will make geometric corrections to the critical temperature of the system. In this case, we will use the geometric correction for bulk cubic zinc blend structure, i.e., $T_c^{cor}/T_c^{MFA} = 0.8162$, to obtain better agreement values with experimental values (Mermin and N.David, 1976). So in this method, we can get dilute magnetic materials at room temperature, as seen in Table 16

Table 16: Total magnetic energy difference, configurations, coupling, and Curie/Neel temperature of Fe and Se co-doped zinc tellurium for different configurations of iron atoms in the systems

Functional	x, y	**Conf.**	ΔE (Ry)	**Stability**	$T_c^{MFA}(K)$	$T_c^{cor}(K)$
LDA	0.5, 0.25	N	0.3370	AFM	17740.6	14479.9
	0.25, 0.125	N	0.4547	AFM	23930	18531.8
		NN	0.0056	AFM	293	239
	0.125, 0.0625	N	0.0090	AFM	475	388.4
		NN	-0.0034	FM	177.9	145.2
LDA+U	0.5, 0.25	N	0.0073	AFM	382.3	312
	0.25, 0.125	N	0.0796	AFM	4192	3421.6
		NN	-0.0024	FM	127.4	103.9
	0.125, 0.065	N	-0.0404	FM	1225.5	1734.8
		NN	-0.0403	FM	2122	1732

D. Magnetic Properties in FeSe

The calculation of spin-polarized DFT is also performed for FeSe using PBE and PBEsol approximations to see its magnetic properties and compare to norm-conservative pseudo-potentials in the feasibility of magnetic property approximation, see Figure 40. Its magnetic property is described by using the total energy difference between ferromagnetic and antiferromagnetic DFT calculations. As clearly seen from the results described in Table 17, semi-relativistic norm-conservative pseudo-potential is not good at approximating magnetic properties in FeSe. The calculated total and absolute magnetic moments of FeSe by using different pseudo potentials are seen in Table 17. Since the iron is expected to be ferromagnetic in this compound, the compound is expected to be ferromagnetic in semiconductor materials.

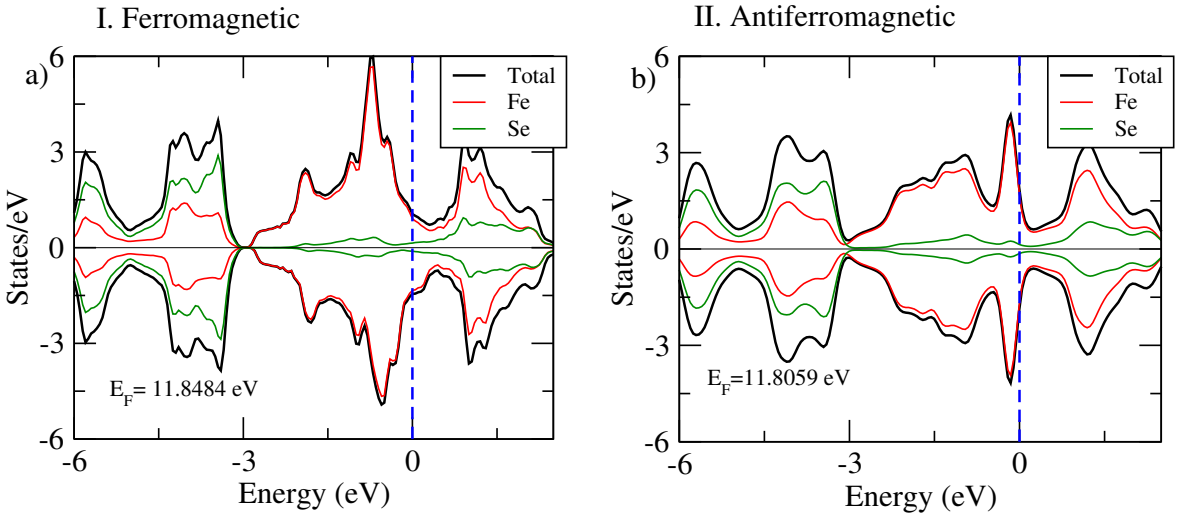

Figure 40: The total density of states of a) ferromagnetic and b) antiferromagnetic systems of FeSe

To this end, from the concept of mean-field approximation (MFA), the Curie temperature T_C can be estimated from the energy difference between the ferromagnetic and antiferromagnetic states as described in equations (2.22) and (4.3).

Table 17: The total calculated magnetic energy, distance between dopant atoms, magnetic moments (absolute and total), and couplings in FeSe

Functional	$d_{Fe-Fe},(A^o)$	**Δ E(Ry)**	**Moment,** $\mu(\mu_B)$		Coupling
			Absolute(A/F)	Total(A/F)	
PBE	3.9836	0.02322727	6.70/7.70	0.0/7.70	AFM
PBEsol	3.9836	0.0234486	6.74/7.83	0.0/7.83	AFM
PBE(NC)	2.6013	0.00574156	3.13/0.30	0.0/0.24	AFM

4.5. Lattice Vibration in $Zn_{(1-x)}Fe_xSe_yTe_{(1-y)}$ System

4.5.1 Lattice Vibration Analysis in $Zn_{(1-x)}Fe_xSe$ System

In this case, there are two types of atoms in a unit cell (Zn and Se or Te), hence there are six modes, with three optical and three acoustic branches. Specifically, there are one longitudinal (LO) and two transverse optical (TO) modes, as well as one longitudinal acoustic (LA) and two transverse optical (TA) modes. These modes are indicated in Figure 42 a). Usually, the longitudinal acoustic modes have steeper slopes near Γ points as compared to the transverse acoustic modes. Similarly, optical branches can be differentiated based on their frequencies; longitudinal optical modes are those with a higher frequency at a given k-point.

For the phonon calculation, we used the GGA functional for both cases. As a result, we get the positive phonon frequencies for all the k points. This proves that the structure is stable geometrically in both configurations. According to the findings, the highest phonon

frequency is less than $250cm^{-1}$ in both the pristine and 25% doped structures (Figures 41 a) and b). There are two atoms per unit cell for the zinc-blend ZnSe structure, so it has three optical and three acoustic phonon modes. The results for phonon dispersion agree well with the empirical results as reported (in cm^{-1}, Γ:213, 253; X: 70, 194, 213, 219; L: 57, 166) measured by neutron scattering (Wang et al., 2016a; Tanaka, 2020). The indicated points in this study for pure ZnSe are described as (in cm^{-1}, Γ:213, 216; X: 70, 96, 147, 209, 212, 231; L: 77, 118 , 181, 215, 238) which is comparable to reported values (Wang et al., 2016a). As seen in Figure 41 b), for 25% iron-doped zinc selenide, the frequencies (in cm^{-1}, Γ: 158, 198,212, 220; X: 70, 196, 213, 218, 223, 229; L: 58, 154, 227) are observed. The phonon frequency calculated for ZnSe in this work using GGA functional is comparable with the experimental result (Hennion et al., 1971).

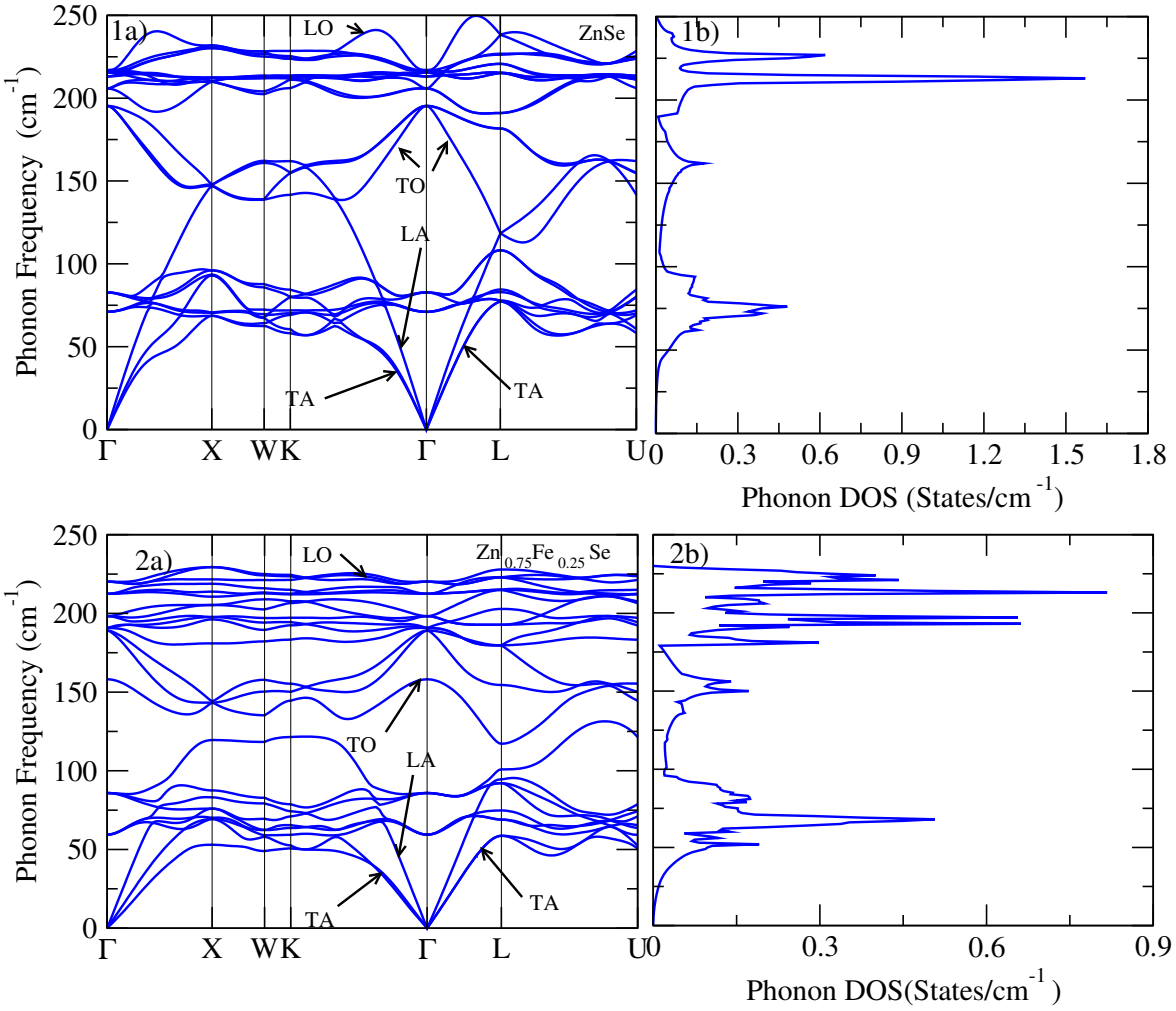

Figure 41: The phonon dispersion a) and Density of States b)of 1) ZnTe 2) $ZnSe_{0.25}Te_{0.75}$ 3) $Zn_{(0.75}Fe_{0.25}Se_{0.25}Te_{0.75}$

4.5.2 Lattice Vibration Analysis in $\mathbf{Zn_{(1-x)}Fe_xSe_yTe_{(1-y)}}$ System

The phonon frequency of the pristine ZnTe can not exceed the frequency of 225 cm^{-1} in this study, which is in agreement with experimental data and previous reports (Kremer et al., 2012). The forbidden frequency gap is also observed in the phonon dispersion gap of ZnTe around 150-160 cm^{-1} while the higher magnitude phonon density of the state is around 193 cm^{-1} as seen in Figures 42 1a) and 1b). The calculated frequencies at high symmetry points are (in cm^{-1}, Γ: 191.3517, 192.2181, X: 202.57, 202.9, W: 200.54, 202.19, 202.7 , K: 199.4, 200.88, 202.69; L: 199.5, 208.8, 209.5 and U: 199.4, 200.9, 202.7 which are consistent with the reported values. The phonon dispersion calculation of $Zn_{(1-x)}Fe_xSe_yTe_{(1-y)}$, for x = 0.25 and y = 0.25 revealed that this alloy is geometrically stable and the localized frequency states are observed above 200 cm^{-1} with overall dispersion of this system does not exceed the frequency of 300 cm^{-1} as seen in Figure 42 2a) and 2b). From the calculation result, the frequencies for $Zn_{(1-x)}Fe_xSe_yTe_{(1-y)}$ (in cm^{-1}, Γ: 218.5, 269.72, 293.85, X: 269.6, 270.2, 295.02, W: 268.8, 270.2, 293.8, K: 268.3, 269.7, 294.3, L: 268.7, 270.9, 294.3, and U: 218.5, 270.8, 293.9) are observed.

4.5.3 Lattice Vibration in FeSe

In this instance, the PBE norm conservative pseudo-potential is used to determine the lattice vibration in a tetragonal FeSe system. The system is geometrically stable, as shown in Figure 43. The transverse acoustic phonon has shorter slopes to the right of the Γ point than to the left. This is caused by the material's anisotropic crystal behavior, which is directly related to the atomic configurations, lattice constant, and other crystallographic characteristics of FeSe. The method used to measure how quickly sound waves move through crystals in various directions varies. In this system with the described pseudo-potentials, the highest computed frequency can reach 350 cm^{-1}. The greatest phonon states per energy were found to be located at optical modes approximately 300 cm^{-1}, as expected, according to the phonon density of state. In the phonon dispersion of the FeSe system, neither prohibited nor localized frequency levels are seen.

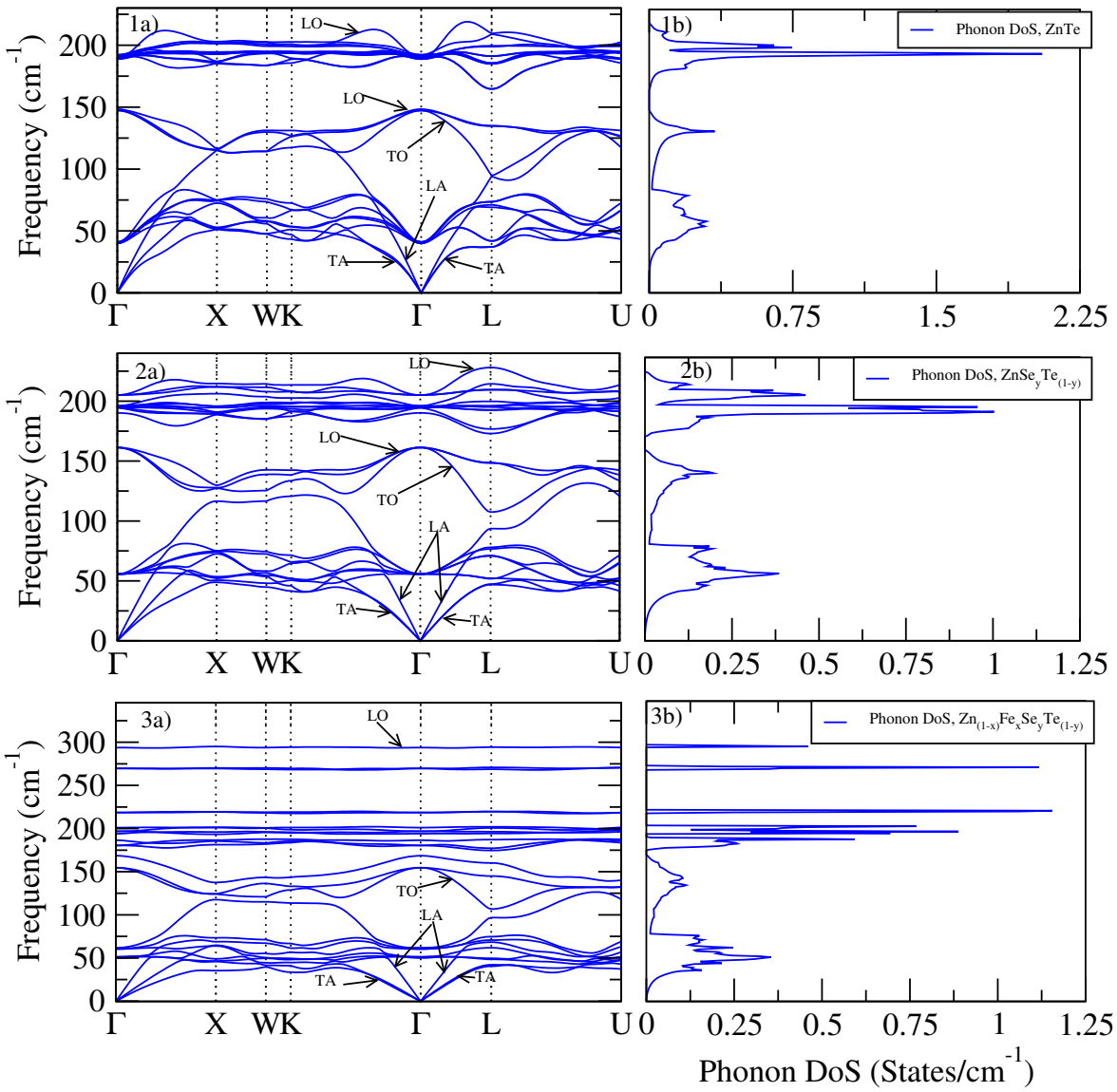

Figure 42: The phonon dispersion a) and Density of States b)of 1) ZnTe 2) $ZnSe_{0.25}Te_{0.75}$ 3)$Zn_{(0.75}Fe_{0.25}Se_{0.25}Te_{0.75}$

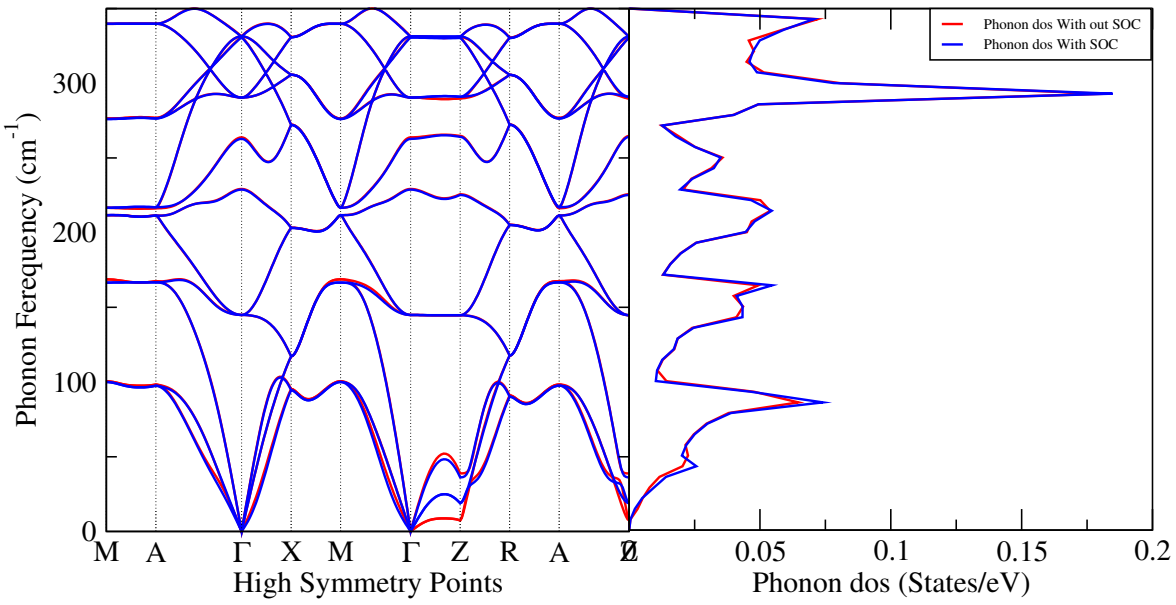

Figure 43: Spin-Orbit effect on FeSe phonon dispersion (blue solid line) and spin-orbit coupling effect (red) without spin-orbit coupling in a) phonon dispersion b) phonon density of states

The spin-orbit coupling in phonon calculation comes into effect in the acoustic modes of branches with frequencies below 150 cm^{-1}. There are three acoustic and three optical branches of vibration modes in a FeSe since it contains only two atoms per unit cell, as indicated in Figure 44.

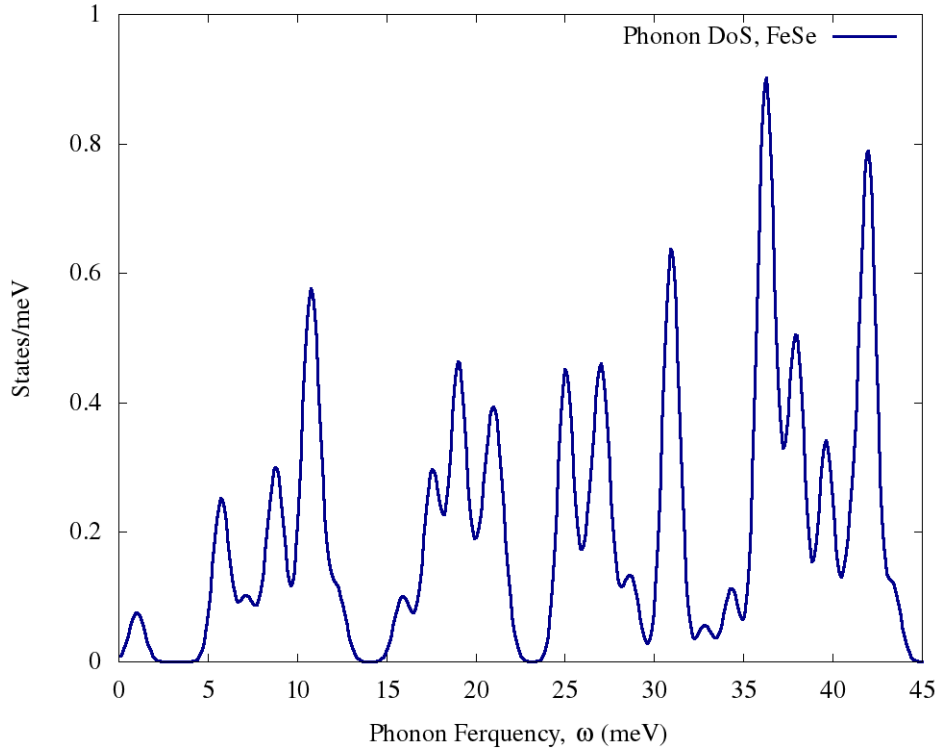

Figure 44: Phonon density of states (in meV) taken from EPW result

4.6. Isotropic Superconductivity Properties of Iron Selenide ($FeSe$)

4.6.1 Eliashberg Spectral Function, $\alpha^2F(\omega)$

The calculated $\alpha^2F(\omega)$, as seen in the Figure 45. It shows three huge and narrower peaks centered at 10, 26, and 38 meV. The electron-phonon coupling strength is $\lambda = 1.46$, indicating that the system is highly correlated. The band and wave vector-dependent coupling strength results in a number of thinner peaks scattered between the ranges λ_k = 0-2.3, making it challenging to classify the material as a multi-band superconductor. This implies that the tetragonal FeSe system exhibits isotropic superconductivity (see Figure 45.

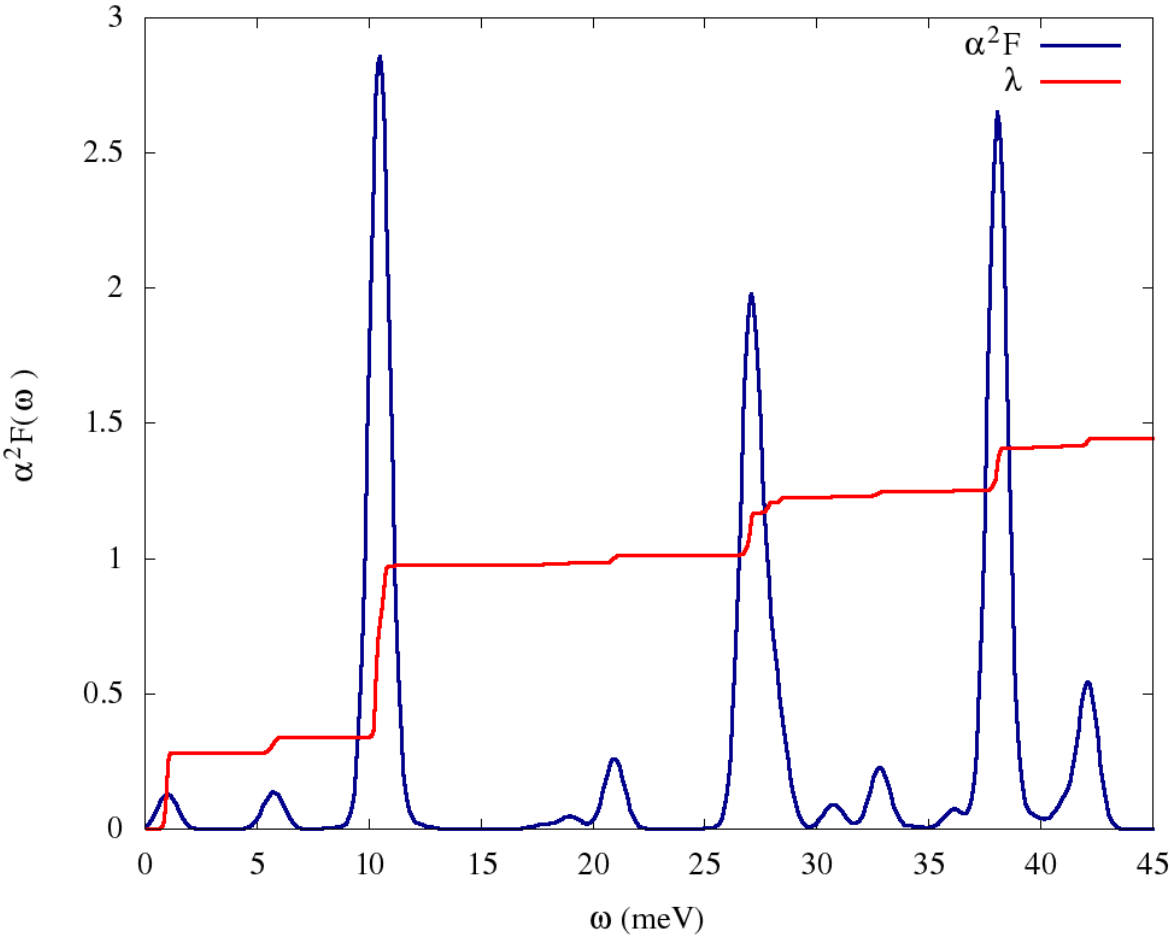

Figure 45: Computed isotropic Eliashberg spectral function $\alpha^2F(\omega)$ (blue solid line) and electron-phonon coupling strength λ (red solid line) of superconducting gap tetragonal FeSe

4.6.2 Superconductivity Critical Temperature

The critical temperature, Tc, of the FeSe superconductor, is obtained by the McMillan formula.

$$T_c = \frac{\omega_{log}}{1.2} exp\left[\frac{-1.04(1+\lambda)}{\lambda(1-0.62\mu^*)+\mu^*},\right] \tag{4.4}$$

where,

$$\omega_{log} = exp\left[\frac{2}{\lambda}\int \frac{d\omega}{\omega}\alpha^2F(\omega)\log\omega\right], \tag{4.5}$$

The $\mu*$ is an empirical parameter that describes Coulomb screening, with average values ranging from 0.1 to 0.16. For the Fermi window of 0.2, we calculated the isotropic equation stated above for $\mu*$ = 0.1 and T = 15 K (Schrodi et al., 2019) Figure 47. Along the imaginary axis, the superconductivity gap is completely real, demonstrating that the gap is frequency-dependent. The Pade approximation on the real axis illustrates that in the phonon frequency limit, the real component has two peaks with a deep valley between them (Vidberg and Serene, 1977). This shows that the computed gap agrees well with the Eliashberg spectral picture. The imaginary part of the real axis has three peaks and represents a blue shift in

comparison to the real part; see Figure 47. The dependence of the superconducting gap on the imaginary axis is calculated and shown in Figure 46.

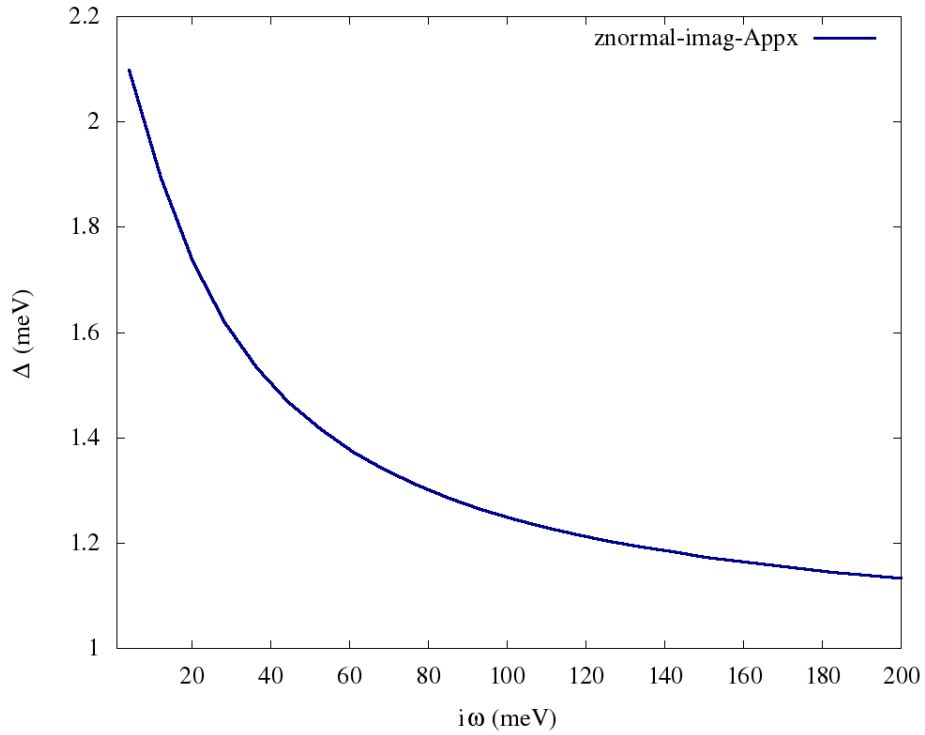

Figure 46: The superconducting gap of FeSe along the imaginary axis at a maximum temperature of 15 K

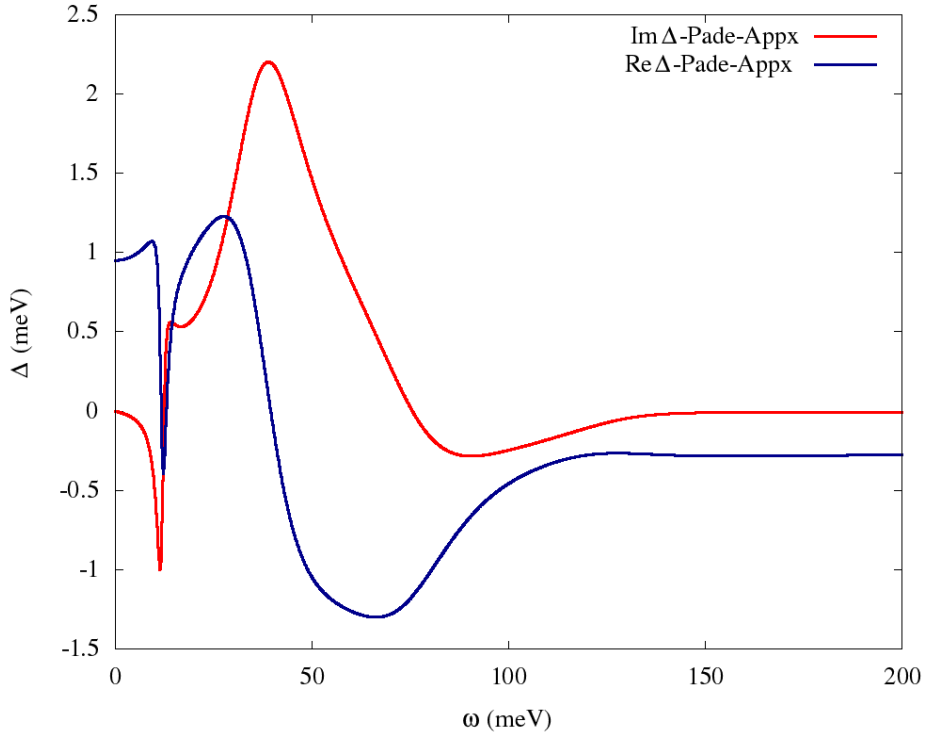

Figure 47: The superconducting gap of FeSe along the real axis via Pade approximation at a maximum temperature of 15 K

As shown in the figure, the superconductivity of the gap as a function of temperature, $\Delta_k(T)$, was calculated for a Fermi window of 0.2 eV and an effective coulomb potential of $\mu^* = 0.1$. The edge of the superconductivity gap of FeSe at T = 0 K is found to be $\Delta_k(0) = 2.738$ meV (see Figure 48). The temperature at which the superconductivity gap of FeSe vanishes is at T = 15 K, which well agrees with the previous reports; even better enhancement is observed in this case.

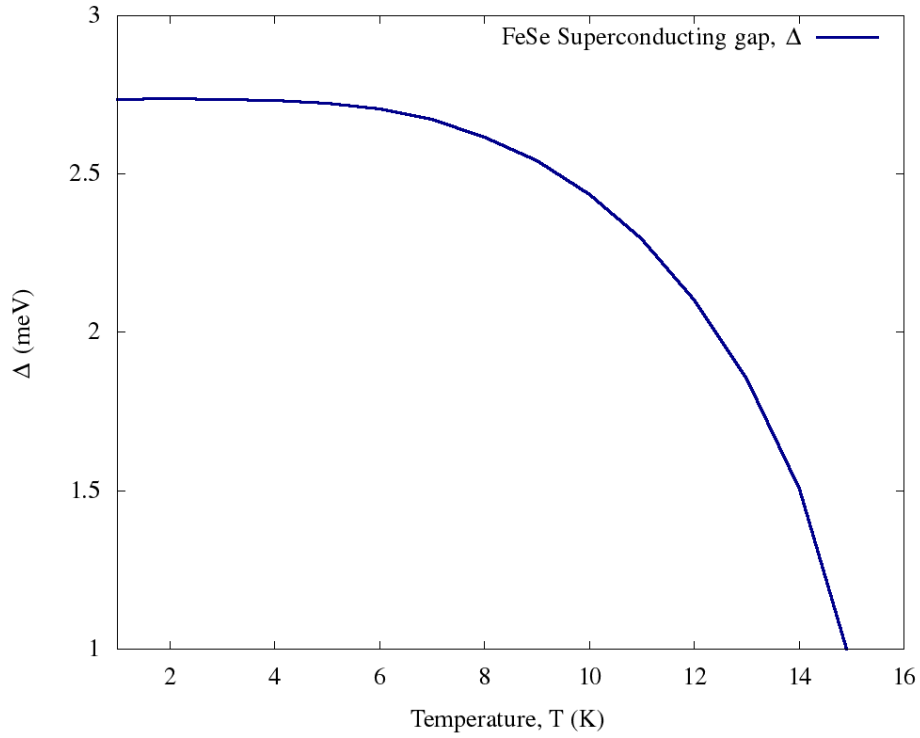

Figure 48: The superconducting gap parameter versus temperature for a tetragonal FeSe

Again, we will calculate the superconductivity gap of FeSe for different Gauss broadenings and analyze it for the converging temperatures of 4 K, 16 K, and 26 K, as shown in Figure 49.

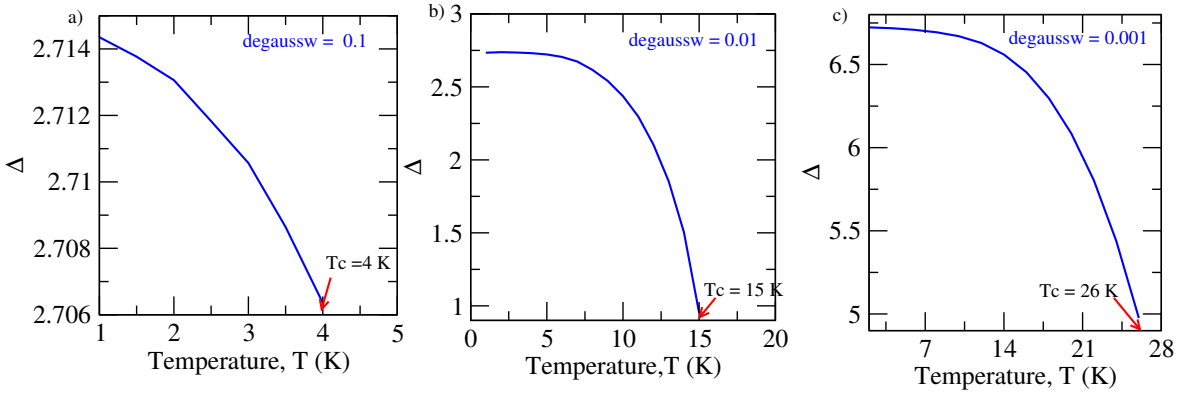

Figure 49: The superconducting gap parameter, Δ(meV) versus temperature, T(K) for a tetragonal FeSe for Gaussian broadening of a) 0.1, b) 0.01 and c) 0.001 for temperature ranges of 4 K, 16 K, and 26 K, respectively

4.6.3 Quasi Particle Density of States

As shown in the figure, we calculated the relative density of state for FeSe superconductors with Fermi windows of 0.2 eV and Gaussian broadening values of 0.01 Ry and plotted it in the frequency range of 0 meV to 10 meV (Choi et al., 2003). The quasi-particle density of states in a superconductor differs from the density of states in normal states because the gap is detected at the Fermi level due to the formation of cooper pairs, but there is no gap in normal states. The steep peak with a magnitude larger than one shows that electron-phonon coupling is strong, and gaps are found at the Fermi level. If the relative QDOS is close to one, the material has a weak coupling with a weak superconducting property or is an ordinary metallic material (Romanin et al., 2021). In this situation, however, it denotes the presence of substantial coupling and superconductivity. The single peaks further demonstrate that FeSe displays isotropic superconductivity, with electrical and superconducting properties that are direction-independent within the temperature range specified. We can tell from this plot that a FeSe has a single band (π band). At T = 15 K, the Fermi surface average of these gaps exceeds the superconducting gap of 2.738 meV. The horizontal black solid line at N_s/N_F =1 represents the normal condition. We can also see that when the temperature rises, the superconducting gap begins to close, and finally, it returns to its usual state, as clearly illustrated in Figure 50. Remarkably, the strong Van Hove singularity indicates the existence of the leading edge superconductivity gap Δ_o which also directly demonstrates the existence of strong electron-phonon coupling and can be a basis for tunneling spectroscopy.

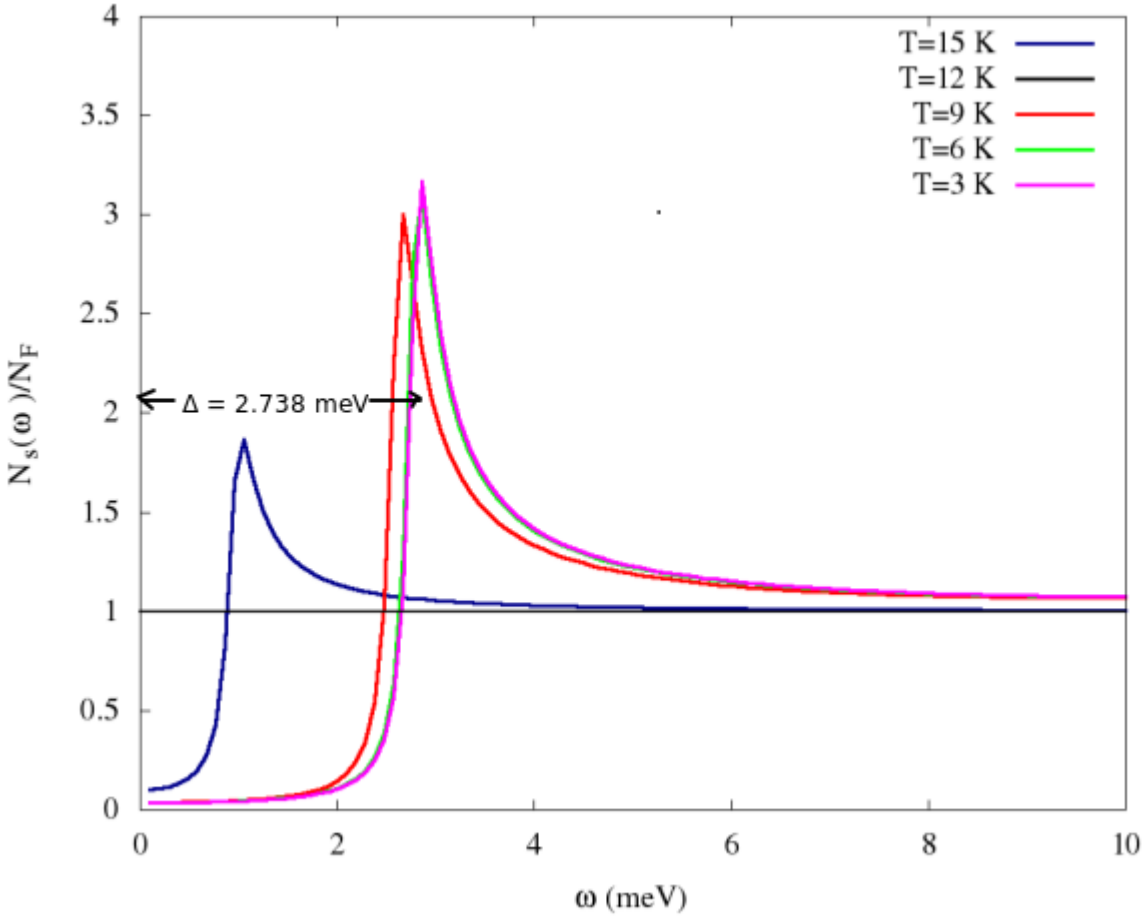

Figure 50: The quasi-particle density of states in the superconducting state relative to the density of states in the normal state N_s/N_F for different temperatures: For superconducting tetragonal FeSe. The horizontal solid line is the normal state of DOS.

4.6.4 Fermi Surface

The occupied states of the free electron gas lie within a sphere. The radius of this sphere is the Fermi radius, and the surface is the Fermi surface. It is helpful to understand material properties such as electrical conductivity, superconductivity, thermal conductivity, and electronic susceptibility. In this case, it demonstrates that there are crossings of bands across Fermi surfaces on the path Γ -M, and the system clearly indicates the metallic behavior where the Γ point is at the center and M point is at the corners, as shown in Figure 51. The Fermi surfaces nesting pockets at the corner of the first Brillouin zone are demonstrated as expected in Fe-based superconductors. The cylindrical side view shape around the top at the Γ point indicates the hybridization of Se-4p and Fe-3d orbitals, which is in line with the previous reports. The Fermi surface is considered to observe the electronic band crossing in direction Γ-X-M in the first Brillouin zone, which clearly agrees with the electronic band structure of FeSe obtained from the PBE norm conservative approximation.

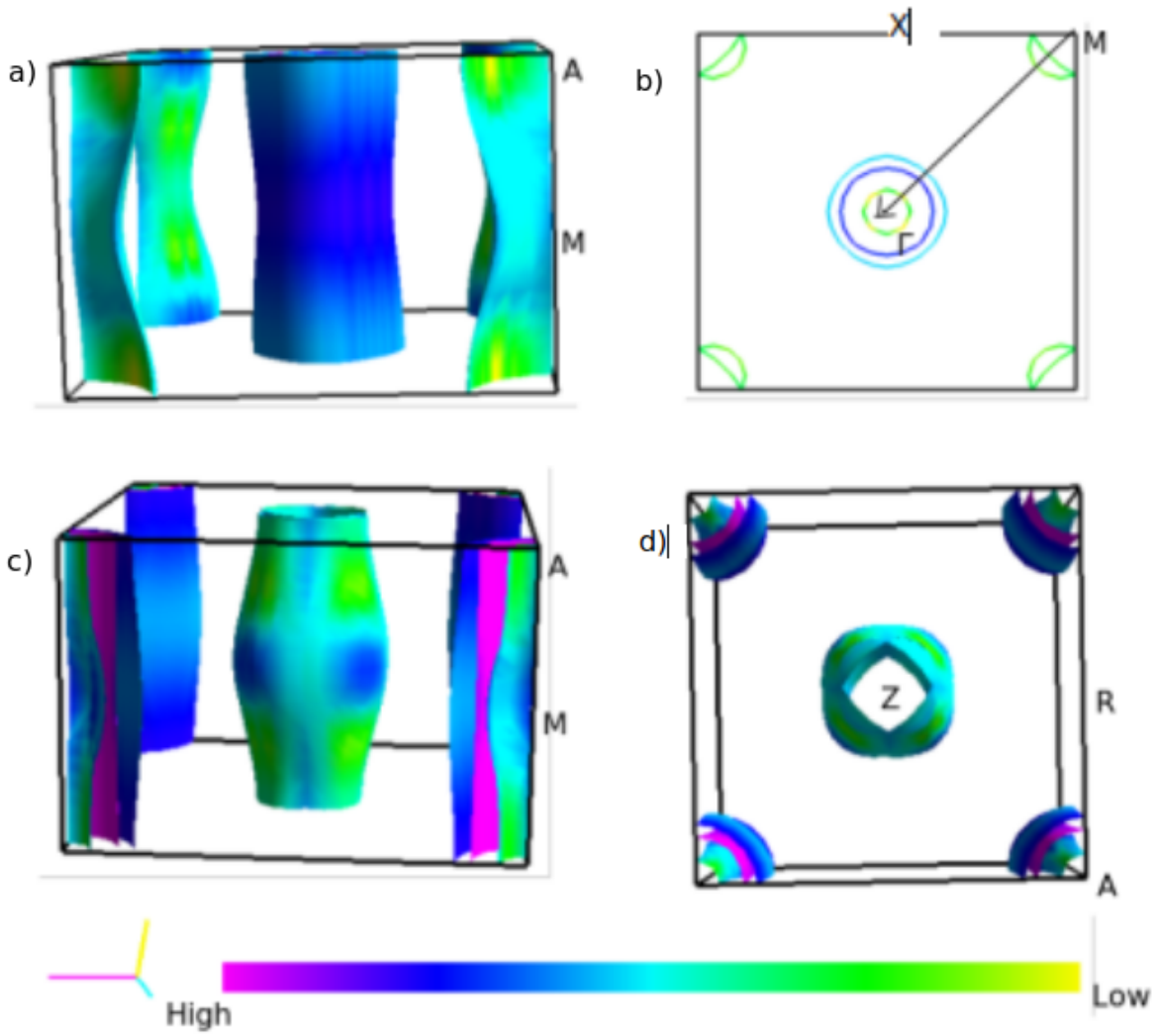

Figure 51: Fermi surface of FeSe a) side view in first Brillouin zone b) sectional view (001) c) side view in primitive Brillouin zone d) top view. The corners are the M points.

4.7. Structural and Electronic Properties of $Zn_{(1-x)}Fe_xSe$ Using Experimental Approach

4.7.1 X-ray Diffraction (XRD) Analysis

The crystal structure of cubic zinc selenide and the naked view of chemical bath-deposited yellowish-white thin films of $Zn_{(1-x)}Fe_xSe$ are shown in Figure 52. This section uses XRD patterns to analyze the obtained ZnSe and Fe-doped zinc selenide thin films and investigate their structural characteristics. Figure 53 depicts the XRD diffraction patterns of zinc selenide and iron-doped zinc selenide (with 1, 2, 3, and 4%). The structural analysis of all samples of thin films covering the Bragg 2θ ranges from 20 to 70^o as depicted in Figure 52. The results indicate that the thin films created using synthetic means are polycrystalline. According to the pattern of the prepared samples, the maximum peaks are indexed at (111), (200), (002), (220), and (222), which is consistent with the space group F43m described in standard JCPDS data card No. 37-1463 (Shikha et al., 2017; Indirajith et al., 2014). This demonstrates the cubic crystal structural phase of the produced ZnSe thin film, with a lattice constant of a = b = c = 5.668 A^o. Another thing that can be seen is that the thin films that are created are strongly oriented in the direction (111), but as the concentration rises, the plane orientation shifts to (220), which is caused by the system's excessive iron composition. The unknown peaks at (002) and (101) suggest that the created thin films are being annealed, resulting in the formation of the associated oxide, ZnO (as indicated in Card No: 00-005-0664). The sharp peaks demonstrate the growth of well-oriented crystals both ZnSe and iron-doped ZnSe. The lattice constant of the thin films can be calculated by using equations (2.48) and (2.50), which are as in Table 18

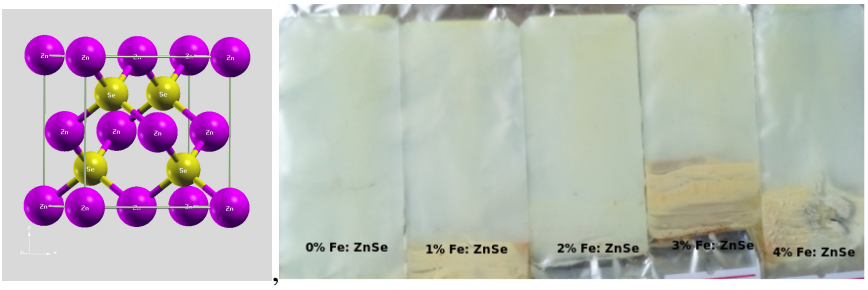

Figure 52: a) The crystal structure of cubic ZnSe b) naked view of the x% Fe: ZnSe thin films (x = 1, 2, 3, and 4)

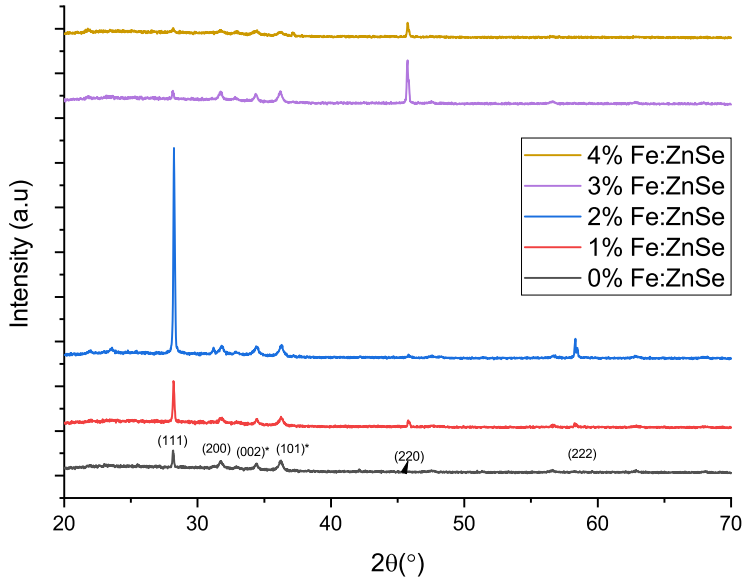

Figure 53: The X-ray diffraction result of $Zn_{(1-x)}Fe_xSe$, x= 0, 1, 2, 3, and 4% thin films

Table 18: The calculated lattice constant of the ZnSe and Fe-doped ZnSe thin films synthesized by the chemical bath deposition

Sample	(hkl)	2θ	$d_{(hkl)}$	a($\mathring{A}$)
ZnSe	111	27.2	3.2758	5.674
	200	31.7	2.820	5.640
1% Fe:ZnSe	111	27.2	3.2758	5.674
	200	31.7	2.820	5.64
2%Fe:ZnSe	111	27.2	3.2758	5.674
	200	31.7	2.8203	5.640
3%Fe:ZnSe	200	31.7	2.8203	5.640
	220	54.2	2.004	5.669
4%Fe:ZnSe	200	31.7	2.8203	5.640
	220	45.2	2.004	5.669

The experimental lattice constant is in good agreement with the JCPDS standard. As also confirmed by DFT calculations, the lattice constant is slightly decreased as the concentration of iron doping is increased.

4.7.2 Ultra Violet Visible (UV-V) Spectroscopy

The percent absorption of $Zn_{(1-x)}Fe_xSe$ for the iron concentration of 0, 1, 2 3, and 4 % are illustrated in Figure 54. This is because as the band gap increases the material becomes

more transparent to the light of longer wavelengths (low energy) (Makuła et al., 2018). This indicates that the percent absorption of light decreases as the material band gap increases. Accordingly, since 4% Fe: doped ZnSe is more conductive with a smaller band gap and the percent absorbance is lower for longer wavelengths which is acceptable in this scenario (Shikha et al., 2017).

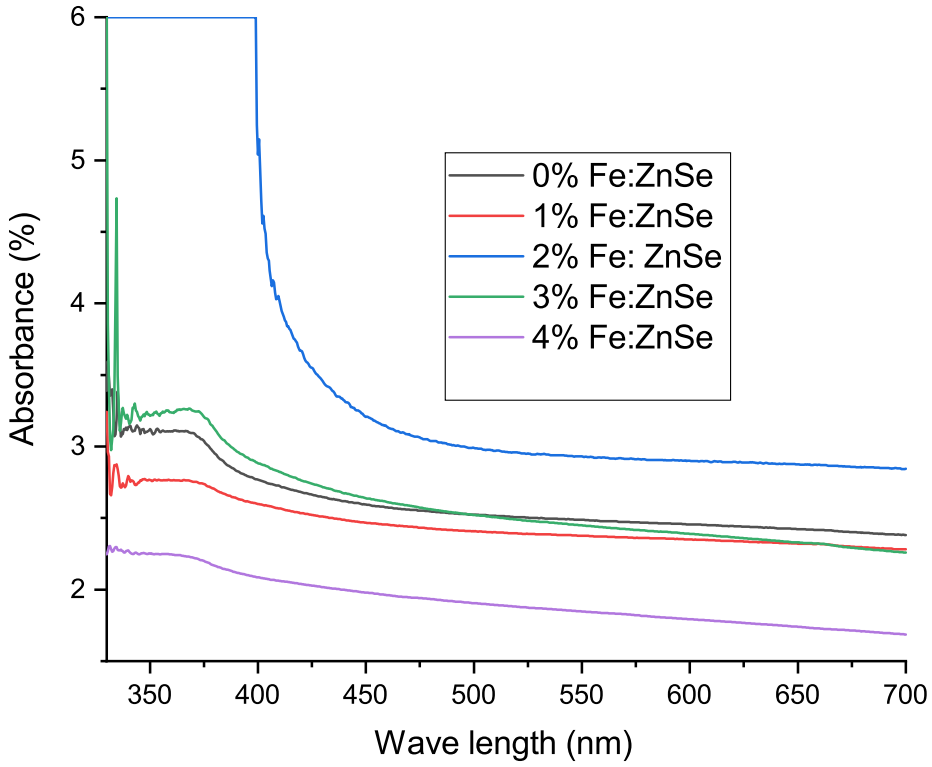

Figure 54: The Percent absorption of $Zn_{(1-x)}Fe_xSe$, x= 0, 1, 2, 3 and 4% thin films

The calculated band gap of ZnSe is 2.706 eV, which is in line with the reported values. From Figure 55, the UV result confirms that up on the iron doping, the band gap of the material is decreased. This shows that the iron metallic property dominates as the concentration of iron increases.

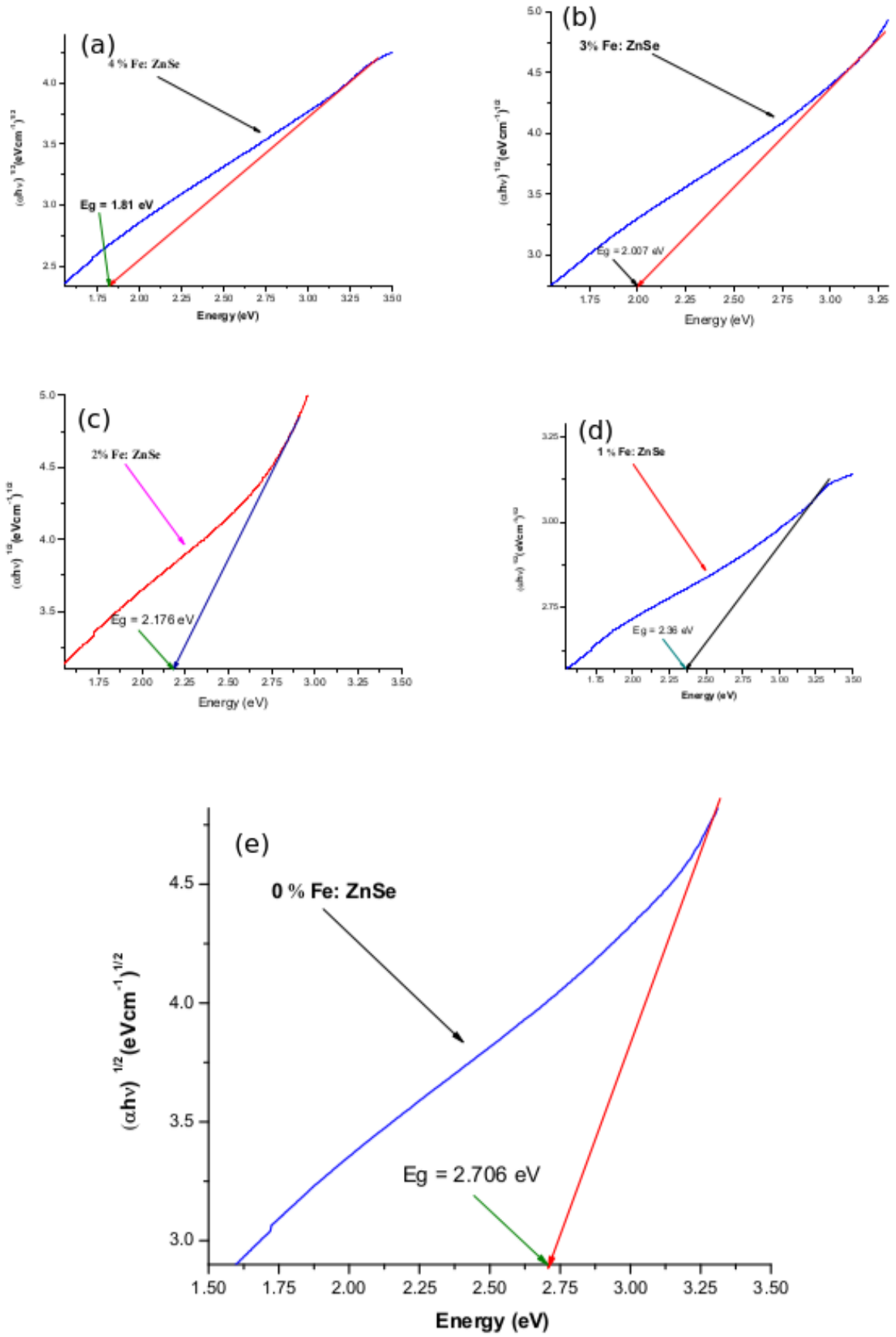

Figure 55: The band gap calculated from the UV-visible absorption data for $Zn_{(1-x)}Fe_xSe$, x= 0, 1, 2, 3, and 4% thin films

5. SUMMARY, CONCLUSIONS AND RECOMMENDATIONS

5.1. Summary

This dissertation is concerned with the study of electronic structure, lattice vibrations, magnetic, and superconducting properties of $Zn_{(1-x)}(Fe, V)_xSe_yTe_{(1-y)}$ materials using computational and experimental methods. The electronic structure, magnetic, vibrational, and superconducting properties of the $Zn_{(1-x)}(Fe, V)_xSe_yTe_{(1-y)}$ material and its fragments, such as $Zn_{(1-x)}Fe_xSe$, $Zn_{(1-x)}(Fe, V)_xSe$, $Zn_{(1-x)}Fe_xSe_yTe_{(1-y)}$ and FeSe are investigated in the context of density functional theory (DFT) using DFT and DFT+U approximations. Basically, zinc chalcogenides are composed of zinc and chalcogen elements such as Se, Te, S, and so on (in this case Se and Te only) that have a wide range of technological applications such as photovoltaic cells, lasers, diodes, visible light photo-detectors, nonlinear optical materials, magneto-optical devices, sensors, photo-converters, luminescence devices, and other optical devices. Furthermore, doping these compounds with transition metals can provide additional benefits, such as enhancing existing properties and applications as well as generating noble qualities with multiple functionalities. Electronic property tunability and mechanical and structural stability, for example, can be achieved, which is not achievable in pristine conditions. Novel properties such as magnetic and half-metal behavior can also be seen in these techniques, which are useful aspects of material application in magnetic and spintronics devices. In this regard, we investigated the quaternary alloy $Zn_{(1-x)}(Fe,V)_xSe_yTe_{(1-y)}$ and its disintegration in order to exploit its electronic, magnetic, lattice vibrations, and superconducting characteristics. As a methodology, we employed the density functional theory (DFT) as employed in a quantum espresso package to study the electronic structure, phonon, and magnetic properties of $Zn_{(1-x)}Fe_xSe$, $Zn_{(1-x)}(Fe, V)_xSe$, $Zn_{(1-x)}Fe_xSe_yTe_{(1-y)}$ and FeSe. The supportive packages such as Phonopy, Xcrysden, Vesta, Xmgrace, Gnuplot, and Fermisurfer were used for supercell creation, structural visualization and study, graphical analysis, editing, and plotting purposes in this dissertation.

5.2. Conclusion

This dissertation focused on the electronic structure, phonon, magnetic, and superconducting properties of transition metal-doped zinc chalcogenide alloys (ZnSe and ZnTe) in general. It also focuses on the properties of the quaternary alloy $Zn_{(1-x)}(Fe,V)_xSe_yTe_{(1-y)}$ and/or its disintegration. In this regard, we explored the effect of transition metal (i.e., Fe and V) doping on semiconductors such as ZnSe, $ZnSe_yTe_{(1-y)}$ in detail utilizing different functionals such as LDA, GGA, LDA+U, and GGA+U.

The short and concise list of remarkable findings of this dissertation is as follows:

- The $Zn_{(1-x)}Fe_xSe$ system shows half-metallic behavior for low concentrations of iron, but its critical temperature is quite low for real-world applications. This was discovered by studying the electronic structure, spin-polarized band, and density of state of $Zn_{(1-x)}Fe_xSe$ using the GGA+U functional.

- The half-metallic ferromagnetic feature of $Zn_{(1-x)}Fe_xSe$ with higher critical temperature is also confirmed by the LDA+U approximation; however, it is still too small for practical usage in magnetic devices.

- The LDA and LDA approximations produce impressive results when used to calculate the magnetic characteristics and electronic structure of $Zn_{(1-x)}V_xSe$. With any higher critical temperature in this system, half-metallic ferromagnetic characteristics are attainable.

- The calculation result shows that by simply adjusting the selenium concentrations, it is feasible to produce a semiconducting material of tertiary alloy, $ZnSe_yTe_{(1-y)}$ with tunable band gaps and electrical characteristics.

- The results of the computation of the electrical and magnetic properties of $Zn_{(1-x)}Fe_xSe_yTe_{(1-y)}$ showed that the system is metallic with no discernible band gaps. Furthermore, it was demonstrated that, at room temperature, this quaternary alloy exhibits half-metallic ferromagnetic properties that can be taken into account for spintronics and magnetic device applications with further experimental investigations.

- Theoretically, an isotropic superconductivity in the FeSe system with an electron-phonon coupling strength of 1.46 and a critical temperature for superconductivity up to 26 K can be confirmed.

- The structural and electrical investigation of $Zn_{(1-x)}Fe_xSe$ thin film revealed that the doping of iron in ZnSe tends to decrease the lattice constant, which is in agreement with the theoretical DFT calculation. The calculated band gap for pristine (0% Fe: ZnSe) is found to be 2.706 eV, which is consistent with the known reported values. On the other hand, as the Fe concentration in ZnS increases, the band gap is lowered, but the percent transmittance of the light is enhanced.

5.3. Recommendation

Further research in this area should concentrate on the electronic structure, lattice vibration, and magnetic characteristics of $Zn_{(1-x)}V_xSe_yTe_{(1-y)}$ employing GGA or hybrid functionals for various phases, including bulk and mono-layers. Another novel topic is the superconductivity of VSe. Other areas for future research include the synthesis of thin films and nanoparticles from composites, including ZnTe/ZnSe and FeSe, in order to examine

their structural morphology and magnetic characteristics. Also, the detailed experimental study on the magnetic properties of $Zn_{(1-x)}(Fe,V)_xSe_yTe_{(1-y)}$ and its components are necessary for the real application of these systems for spintronics and magnetic device applications.

List of Publication

A. Articles Published in a Reputable Journals

During my work, the publications are:

1. Kunsa Haho Habura, Mesfin Asfaw Afrasa and Fekadu Gashaw Hone, Density Functional Theory Study of Zn(1-x) FexSe: Electronic Structure, Phonon and Magnetic Properties, AIP Advances, 13 035102 (2023)

2. Kunsa Haho, Mesfin Asfaw and Fekadu Gashaw, Comparative Analysis of Electronic Structure, and Magnetic Properties of the Zn(1-x) TmxSe (Tm=V, Fe) Using LDA and LDA+U Approximations, Computational Condensed Matter, 35 (2023) e00799

B. Manuscripts Under Review

1. Kunsa Haho, Mesfin Asfaw, and Fekadu Gashaw, Computational Study on the Electronic, Structural, Lattice Vibrations, and Magnetism in $Zn_{(1-x)}Fe_xSe_yTe_{(1-y)}$ Quaternary materials, submitted to journal AIP Advances

2. Electronic Structure and Isotropic Superconductivity Properties of Iron Selenide ($FeSe$), submitted to the journal of in Physica Scripta, IOP Science

C. Manuscripts in Preparation

1. Kunsa Haho, Mesfin Asfaw and Fekadu Gashaw, Effect of Transition Metal Doping on Electronic Structure and Magnetic Properties in Iron Diselenide ($FeSe_2$): *First Principle Study*, intended to submit to computational condensed matter, Elsevier

2. Effect of Iron concentration on Structural and Optical Properties of Fe Doped Zinc Selenide Thin Films, intended to submit to journal of Physica Scripta, IOP Science

3. Kunsa Haho Habura, Mesfin Asfaw Afrassa and Fekadu Gashaw Hone, Electronic, Phonon and optical properties of $ZnSe_yTe_{(1-y)}$ systems, intended to Journal of Advances condensed matter physics, Hindawi

D. Presentations and Conference Participation

1. Ethiopian Physical Society 14th annual conference February 7-8 2020 at Arbaminch University, Arbaminch

2. The 2nd edition of the African Conference on Fundamental and Applied Physics, ACP2021, on March 7-11, 2022

3. Ethiopian School on Electronic Structure Methods and Applications for Emerging Energy Technologies 1^{st} annual congress of the CSESE society, November 22 to December 2, 2021, Addis Ababa University, Ethiopia

4. Abdu Selam International Center for Theoretical Physics, Ab-initio Many-Body Methods and Simulations with the Yambo Code, 04 - 08 April 2022, Trieste, Italy

5. Phonon and Magnetic Properties in Iron doped ZnSe, at 2nd Annual conference Computational Science and Engineering Society of Ethiopia (CSESE) January 2023 (Poster Abstract) organized by Addis Ababa University, Ethiopia

6. The 4th International Research Symposium on "promoting digital economy through research and innovation" April 28-29, 2023 organized by Adama Science and Technology University

7. Kunsa Haho Habura, Mesfin Asfaw Afrassa and Fekadu Gashaw Hone, DFT study of $Zn_{(1-x)}Fe_xSe$: Electronic structure, and magnetic properties, 35th Workshop on Recent Developments in Electronic Structure Methods University of California, Merced June 13th to June 16th, 2023 (Poster Abstract), USA

E. Awards and Special Recognition

1. Ethiopian Physical Society in North America (EPS-NA) awarded him in recognition of his highest scholastic achievement on February 16, 2023 G.C

REFERENCES

Adachi, S. (1999). *Optical Constants of Crystalline and Amorphous Semiconductors Numerical Data and Graphical Information*. Kluwer Academic Publishers, New York, first edition.

Adetunji, B. I., Adebambo, P. O., and Adebayo, G. A. (2012). First principles studies of band structure and electronic properties of ZnSe. *J. Alloys Compd.*, 513:294–299.

Ahluwalia, G. K. (2018). *Applications of chalcogenides: S, Se, and Te*. Springer.

Allen, P. B. and Mitrovi (1983). Theory of Superconducting Tc. *Solid State Phys. - Adv. Res. Appl.*, 37(C):1–92.

Alsaad, A. (2009). Structural and magnetic properties of mn-based diluted magnetic semiconductors and alloys. *Res. Lett. Phys.*, 2009.

A.SArico, D. Silvestro, P.L.Antonucci, N. G. and V.Antonucci (1997). Electrodeposited Thin Film ZnTe Semiconductors for Photovoltaic Applications. *Adv. Perform. Mater.*, 125(4):115–125.

Ba-sabiah, A. S. and Seyam, M. A. (2017). Some optical properties of (znte) thin films prepared by thermal evaporation technique on a glass substrate. *J. nat. appl. sci.*, 14(1):71–78.

Basak, T., Rao, M. N., Gupta, M. K., and Chaplot, S. L. (2012). Vibrational properties and phase transitions in IIVI materials: Lattice dynamics, abinitio studies and inelastic neutron scattering measurements. *J. Phys. Condens. Matter*, 24(11).

Bechiri, A., Benmakhlouf, F., and Bouarissa, N. (2009). Calculation of electronic and optical properties of Zn-based II-VI semiconductors. *Phys. Procedia*, 2(3):803–812.

Bednorz, J., Takashige, M., and Müller, K. (1987). Susceptibility measurements support high-tc superconductivity in the ba-la-cu-o system. *Europhysics Letters*, 3(3):379.

Behloul, M., Salmani, E., Ez-Zahraouy, H., and Benyoussef, A. (2016). Theoretical investigation of electronic, magnetic and optical properties of ZnSe doped TM and co-doped with MnTM (TM: Fe, Cr, Co): AB-initio study. *J. Magn. Magn. Mater.*, 419:233–239.

Benstaali, W., Bentata, S., Abbad, A., and Belaidi, A. (2013). Ab-initio study of magnetic, electronic and optical properties of znse doped-transition metals. *Materials science in semiconductor processing*, 16(2):231–237.

Bilal, M., Shafiq, M., Ahmad, I., and Khan, I. (2014). First principle studies of structural, elastic, electronic and optical properties of Zn-chalcogenides under pressure. *J. Semicond.*, 35(7).

Billas, I. M., Chatelain, A., and de Heer, W. A. (1994). Magnetism from the atom to the bulk in iron, cobalt, and nickel clusters. *Science*, 265(5179):1682–1684.

Böhmer, A. E. and Kreisel, A. (2018). Nematicity , magnetism and superconductivity in FeSe. *J. Phys. Condens. Matter*, 30(023001):28pp.

Challis, L. (1982). Phonons: Theory and Experiments I. Lattice Dynamics and Models of Interatomic Forces. *Opt. Acta Int. J. Opt.*, 29(12):1586–1586.

Chen, L., Fang, C., Liu, W., Chen, X., and Zhao, L. (2019). Structural and magnetic properties of Fe doped small ZnSe nanoclusters. *AIP Conf. Proc.*, 2073(February).

Chen, X. L., Huang, B. J., Feng, Y., Wang, P. J., Zhang, C. W., and Li, P. (2015). Electronic structures and optical properties of TM (Cr, Mn, Fe or Co) atom doped ZnSe nanosheets. *RSC Adv.*, 5(128):106227–106233.

Choi, H. J., Cohen, M. L., and Louie, S. G. (2003). Anisotropic Eliashberg theory of MgB2: Tc, isotope effects, superconducting energy gaps, quasiparticles, and specific heat. *Phys. C Supercond. its Appl.*, 385(1-2):66–74.

Chowdhury, M. T., Zubair, M. A., Takeda, H., Hussain, K. M. A., and Islam, M. F. (2017). Optical and structural characterization of znse thin film fabricated by thermal vapour deposition technique. *AIMS Materials Science*, 4(5).

Chowdhury, U. K. and Islam, R. (2018). The Properties , Advantage , Disadvantage and Applications of Iron-Based Superconductors : A Review Work. *Int. J. Adv. Res. Phys. Sci.*, 5(9):16–31.

Chu, C. H. and Leung, C. W. (2001). The convolution equation of Choquet and Deny on [IN]-groups. *Integr. Equations Oper. Theory*, 40(4):391–402.

Ciechan, A. and Winiarski, M. J. (2011). The pressure effects on electronic structure of iron chalcogenide superconductors fese(1-x)te(x). *Acta Physica Polonica A*.

Cococcioni, M. and De Gironcoli, S. (2005). Linear response approach to the calculation of the effective interaction parameters in the lda+u method. *Phys. Rev. B - Condens. Matter Mater. Phys.*, 71(3):1–16.

Coey, J. M. D. (2008). *Magnetism and Magnetic Materials*. Cambridge University Press, UK.

Coldea, A. I. and Watson, M. D. (2018). The key ingredients of the electronic structure of fese. *Annual Review of Condensed Matter Physics*, 9:125–146.

Cosar, M. B., Aydogdu, G. H., Batman, H., and Ozhan, A. E. (2017). A solution to adhesion problem of oxide thin films on Zinc Selenide optical substrates. *Surf. Coatings Technol.*, 314:118–124.

Cullity, B. D. (1956). *Elements of X-ray Diffraction*. Addison-Wesley Publishing.

David M Uhrig, S. V. C. (2019). Thermal post processing of FeSe(1-x)Tex : formation of surface iron oxides and enhancement of Jc. *Supercond. Sci. Technol.*, 32(074002).

Dietl, T. and Ohno, H. (2014). Dilute ferromagnetic semiconductors: Physics and spintronic structures. *Rev. Mod. Phys.*, 86(1):187–251.

Dixon, D. A. (2016). Density functional theory. *Encycl. Earth Sci. Ser.*, pages 1–7.

Drozdov, A. P., Eremets, M. I., Troyan, I. A., Ksenofontov, V., and Shylin, S. I. (2015). Conventional superconductivity at 203 kelvin at high pressures in the sulfur hydride system. *Nature*, 525(7567):73–76.

Eliashberg, G. (1960). Interactions between electrons and lattice vibrations in a superconductor. *Sov. Phys. JETP*, 11(3):696–702.

Eliashberg, G. M. (1961). Temperature Green's function for electrons in a superconductor. *J. Exptl. Theor. Phys.*, 12(5):1437–1441.

Faschinger, W., Ferreira, S., and Sitter, H. (1994a). Doping of zinc-selenide-telluride. *Appl. Phys. Lett.*, 64(20):2682–2684.

Faschinger, W., Ferreira, S., and Sitter, H. (1994b). Doping of zinc-selenide-telluride. *Appl. Phys. Lett.*, 64(20):2682–2684.

Fusil, S., Garcia, V., Barthélémy, A., and Bibes, M. (2014). Magnetoelectric devices for spintronics. *Annu. Rev. Mater. Res.*, 44:91–116.

Gavrichev, K. S., Sharpataya, G. A., Guskov, V. N., Greenberg, J. H., Feltgen, T., Fiederle, M., and Benz, K. W. (2002). Thermodynamic properties of ZnTe in the temperature range 15-925 K. In *Phys. Status Solidi Basic Res.*, volume 229, pages 133–135.

Gerbi, Z. D. and Singh, P. (2019). Effect of hydrostatic pressure on superconductivity of MgB2. *AIP Adv.*, 9(9).

Giannozzi, P., Baseggio, O., Bonfà, P., Brunato, D., Car, R., Carnimeo, I., Cavazzoni, C., De Gironcoli, S., Delugas, P., Ferrari Ruffino, F., et al. (2020a). Quantum espresso toward the exascale. *The Journal of chemical physics*, 152(15).

Giannozzi, P., Baseggio, O., Bonfà, P., Brunato, D., Car, R., Carnimeo, I., Cavazzoni, C., De Gironcoli, S., Delugas, P., Ferrari Ruffino, F., et al. (2020b). Quantum espresso toward the exascale. *The Journal of chemical physics*, 152(15).

Giustino, F., Cohen, M. L., and Louie, S. G. (2007). Electron-phonon interaction using Wannier functions. *Phys. Rev. B - Condens. Matter Mater. Phys.*, 76(16):1–19.

Gromboni, M. F. and Mascaro, L. H. (2016). Optical and structural study of electrodeposited zinc selenide thin fi lms. *JEAC*, 780:360–366.

Guo, M., Gao, G., and Hu, Y. (2011). Magnetism and electronic structure of Mn- and V-doped zinc blende ZnTe from first-principles calculations. *J. Magn. Magn. Mater.*, 323(1):122–126.

Gupta, A., Zhang, R., Kumar, P., Kumar, V., and Kumar, A. (2020). Nano-structured dilute magnetic semiconductors for efficient spintronics at room temperature. *Magnetochemistry*, 6(1):1–22.

Habura, K., Afrassa, M., and Hone, F. (2023). Comparative analysis of the electronic structure and magnetic properties of Zn(1-x)Tmx Se(Tm = Fe, V) using LDA and LDA+U approximations. *Comput. Condens. Matter*, 35(November 2022):e00799.

Hasaneen, M., Alrowaili, Z., and Mohamed, W. (2020a). Structure and optical properties of polycrystalline znse thin films: validity of swanepol's approach for calculating the optical parameters. *Materials Research Express*, 7(1):016422.

Hasaneen, M. F., Alrowaili, Z. A., and Mohamed, W. S. (2020b). Structure and optical properties of polycrystalline ZnSe thin films: Validity of Swanepol's approach for calculating the optical parameters. *Mater. Res. Express*, 7(1).

Hennion, B., Moussa, F., Pepy, G., and Kunc, K. (1971). Normal modes of vibrations in ZnSe. *Phys. Lett. A*, 36(5):376–378.

Hosono, H., Yamamoto, A., Hiramatsu, H., and Ma, Y. (2018). Recent advances in iron-based superconductors toward applications. *Materials today*, 21(3):278–302.

Hu, K., Wu, M., Hinokuma, S., Ohto, T., Wakisaka, M., Fujita, J. I., and Ito, Y. (2019). Boosting electrochemical water splitting: via ternary NiMoCo hybrid nanowire arrays. *J. Mater. Chem. A*, 7(5):2156–2164.

Indirajith, R., Rajalakshmi, M., Ramamurthi, K., Ahamed, M. B., and Gopalakrishnan, R. (2014). Synthesis of ZnSe nano particles, deposition of ZnSe thin films by electron beam evaporation and their characterization. *Ferroelectrics*, 467(1):13–21.

Isherwood, P. J. M., Kaminski, P. M., Walls, J. M., Li, J., Wolden, C. A., and Uli, S. (2017). Development of ZnTe as a back contact material for thin fi lm cadmium telluride solar cells. *Vacuum*, 139:159–163.

Ismayilova, N. A. and Abbasov, I. I. (2021). First principle calculation of electronic, optical and magnetic properties of Zn 1 - X Fe x Se compound. *Int. J. Mod. Phys. B*, 35(28):1–7.

Jang, D., Han, Y., Baek, S., and Kim, J. (2019). Theoretical comparison of the energies and wave functions of the electron and hole states between CdSe- and InP-based core/shell/shell quantum dots: effect of the bandgap energy of the core material on the emission spectrum. *Opt. Mater. Express*, 9(3):1257.

Jung, J. Y., Park, J. H., Jeong, Y. J., Yang, K. H., Choi, N. K., Kim, S. H., and Kim, W. J. (2006). Involvement of Bcl-2 family and caspases cascade in sodium fluoride-induced apoptosis of human gingival fibroblasts. *Korean J. Physiol. Pharmacol.*, 10(5):289–295.

Kabita, K. and Indrajit Sharma, B. (2017). A theoretical study on the B3 phases of ZnSe: Structural and electronic properties. *Pramana - J. Phys.*, 89(1):1–4.

Kanki, K. and Yamada, K. (1993). Electron-Phonon Interaction and Superconductivity in Heavy Electron Systems. *J. Phys. Soc. Japan*, 62(11):4031–4043.

Khalfi, R., Talantikite-Touati, D., Tounsi, A., Souici, A., Merzeg, F. A., and Azizi, A. (2023). Effect of manganese doping on the structural, morphological and optical properties of zinc selenide thin films prepared by chemical bath deposition method. *Applied Physics A*, 129(3):231.

Khenata, R., Bouhemadou, A., Sahnoun, M., Reshak, A. H., Baltache, H., and Rabah, M. (2006). Elastic, electronic and optical properties of ZnS, ZnSe and ZnTe under pressure. *Comput. Mater. Sci.*, 38(1):29–38.

Koch, W. and Holthausen, M. C. (2015). *A chemist's guide to density functional theory*. John Wiley & Sons.

Kohn, W. and Sham, L. J. (1965). Self-consistent equations including exchange and correlation effects. *Phys. Rev.*, 140(4A).

Kokalj, A. (1999). XCrySDen-a new program for displaying crystalline structures and electron densities. *J. Mol. Graph. Model.*, 17(3-4):176–179.

Kremer, R. K., Cardona, M., Lauck, R., Siegle, G., and Romero, A. H. (2012). Vibrational and thermal properties of ZnX (X=Se, Te): Density functional theory (LDA and GGA) versus experiment. *Phys. Rev. B - Condens. Matter Mater. Phys.*, 85(3).

Kuan, T. (1995). *Semiconductor alloys: physics and materials engineering*. Springer Science.

Kulyuk, L. L., Laiho, R., Läshkul, A. V., Lhderanta, E., Nedeoglo, D. D., Nedeoglo, N. D., Radevici, I. V., Siminel, A. V., Sirkeli, V. P., and Sushkevich, K. D. (2010). Magnetic and luminescent properties of iron-doped ZnSe crystals. *Phys. B Condens. Matter*, 405(20):4330–4334.

Kumar, P. and Singh, K. (2011). Ferromagnetism in Cu-doped ZnSe semiconducting quantum dots. *J. Nanoparticle Res.*, 13(4):1613–1620.

Laiho, R., Lashkul, A. V., Lähderanta, E. M., Nedeoglo, D. D., Nedeoglo, N. D., Radevici, I. V., Sirkeli, V. P., and Sushkevich, K. D. (2010). Magnetic properties of ZnSe crystals doped with transition metals. *AIP Conf. Proc.*, 1292:197–200.

Li, X. and Yang, J. (2016a). First-principles design of spintronics materials. *Natl. Sci. Rev.*, 3(3):365–381.

Li, X. and Yang, J. (2016b). First-principles design of spintronics materials. *National Science Review*, 3(3):365–381.

Liu, H. and Zhang, J.-M. (2017). Effect of two identical 3d transition-metal atoms m doping (m= v, cr, mn, fe, co, and ni) on the structural, electronic, and magnetic properties of zno. *physica status solidi (b)*, 254(10):1700098.

Liu, X., Lam, K. H., Zhu, K., Zheng, C., Li, X., Du, Y., Liu, C., and Pong, P. W. (2019). Overview of Spintronic Sensors with Internet of Things for Smart Living. *IEEE Trans. Magn.*, 55(11).

Liu, X., Zhao, L., He, S., He, J., Liu, D., Mou, D., Shen, B., Hu, Y., Huang, J., and Zhou, X. (2015). Electronic structure and superconductivity of fese-related superconductors. *Journal of Physics: Condensed Matter*, 27(18):183201.

Lumsden, M. D. and Christianson, A. D. (2010). Magnetism in fe-based superconductors. *Journal of Physics: Condensed Matter*, 22(20):203203.

Lungu, I., Zalamai, V. V., Monaico, E. I., Ghimpu, L., and Potlog, T. (2023). Effect of deposition temperature on structural, morphological and optical properties of ZnTe thin films. *J. Mater. Sci.*, 58(10):4384–4398.

Mahi, N. and Bouhafs, B. (2012). Contribution to the study of electronic structure of crystalline semiconductors (si, ge, gaas, gap, znte, znse). 29:00027.

Mahmood, Q., Hassan, M., and Noor, N. A. (2016). Systematic study of room-temperature ferromagnetism and the optical response of Zn1-xTMxS/Se (TM = Mn, Fe, Co, Ni) ferromagnets: First-principle approach. *J. Phys. Condens. Matter*, 28(50):506001.

Mahmood, Q., Murtaza, G., Ali, G., Hassan, M., Algrafy, E., Shahid, M. S., Kattan, N. A., and Laref, A. (2020). Probing the electronic structure and magnetism in Ni doped ZnTe: A DFT modeling and experiment. *J. Alloys Compd.*, 834:155176.

Majid, A., Ahsan, S. A., Alkhedher, M., Haider, S., and Akhtar, M. S. (2023). A density functional theory study on al2co-based diluted magnetic semiconductor. *Journal of Superconductivity and Novel Magnetism*, pages 1–13.

Majorana, E. and Zichichi, A. (1991). *Semimagnetic Semiconductors and Diluted Magnetic Semiconductors*. Springer, New York.

Makula, P., Pacia, M., and Macyk, W. (2018). How to correctly determine the band gap energy of modified semiconductor photocatalysts based on uv–vis spectra. *Phys. Chem. Lett.*, 9(23):6814–6817.

Makuła, P., Pacia, M., and Macyk, W. (2018). How To Correctly Determine the Band Gap Energy of Modified Semiconductor Photocatalysts Based on UV-Vis Spectra. *J. Phys. Chem. Lett.*, 9(23):6814–6817.

Mann, G. W., Lee, K., Cococcioni, M., Smit, B., and Neaton, J. B. (2016). First-principles Hubbard U approach for small molecule binding in metal-organic frameworks. *J. Chem. Phys.*, 144(17).

Margine, E. R. and Giustino, F. (2013). Anisotropic Migdal-Eliashberg theory using Wannier functions. *Phys. Rev. B - Condens. Matter Mater. Phys.*, 87(2):1–12.

Margine, E. R., Lambert, H., and Giustino, F. (2016). Electron-phonon interaction and pairing mechanism in superconducting Ca-intercalated bilayer graphene. *Sci. Rep.*, 6(January):2–7.

Martin, R. M. (2020). *Electronic structure: basic theory and practical methods*. Cambridge university press.

Mehmood, K., Rehman, U., Liu, X., Riaz, M., and Yang, Y. (2019). Fabrication and Characterization of Zinc Telluride (ZnTe) Thin Films Grown on Glass Substrates. *Phys. B Phys. Condens. Matter*.

Mekuye, B. and Abera, B. (2023). A theoretical model of high curie temperature for n-type ferromagnetic diluted semiconductors based on iron-doped indium antimonide. *Front. Phys.*, 11:1196391.

Mermin, N. W. and N.David (1976). *Solid State Physics*. Saunders college, Chicago, 17 edition.

Migdal, A. (1958). Interaction between electrons and lattice vibrations in a normal metal. *Sov. Phys. JETP*, 7(6):996–1001.

Mondal, A., McCandless, B. E., and Birkmire, R. W. (1992). Electrochemical deposition of thin ZnTe films as a contact for CdTe solar cells. *Sol. Energy Mater. Sol. Cells*, 26(3):181–187.

Morkoç, H., Strite, S., Gao, G. B., Lin, M. E., Sverdlov, B., and Burns, M. (1994). Large-band-gap SiC, III-V nitride, and II-VI ZnSe-based semiconductor device technologies. *J. Appl. Phys.*, 76(3):1363–1398.

Muratov, A. V., Sadakov, A. V., Gavrilkin, S. Y., Prishchepa, A. R., Epifanova, G. S., Chareev, D. A., and Pudalov, V. M. (2018). Specific heat of FeSe: Two gaps with different anisotropy in superconducting state. *Phys. B Condens. Matter*, 536(October 2017):785–789.

N. Kamoun Allouchea, b, T. B. N. N. T. K. C. G. (2010). Synthesis and properties of chemical bath deposited ZnS multilayer films. *Mater. Chem. Phys.*, 123(2-3):620–624.

Nagamatsu, J., Nakagawa, N., Muranaka, T., Zenitani, Y., and Akimitsu, J. (2010). ChemInform Abstract: Superconductivity at 39 K in Magnesium Diboride. *ChemInform*, 32(21):no–no.

Nekrasov, I., Pavlov, N., Sadovskii, M., and Slobodchikov, A. (2016). Electronic structure of fese monolayer superconductors. *Low Temp. Phys.*, 42(10):891–899.

Nitsuk, Y. A. (2014). Optical absorption of vanadium in znse single crystals. *Semiconductors*, 48(2):142–147.

Ochoa-Estrella, F. J., Vera-Marquina, A., Mejia, I., Leal-Cruz, A. L., Pintor-Monroy, M. I., and Quevedo-López, M. (2018). Structural, optical, and electrical properties of ZnTe:Cu thin films by PLD. *J. Mater. Sci. Mater. Electron.*, 29(24):20623–20628.

Ogawa, H., Irfan, G. S., Nakayama, H., Nishio, M., and Yoshida, A. (1994). Growth of low-resistivity n-type znte by metalorganic vapor phase epitaxy. *Jpn. J. Appl. Phys.*, 33(7):L980–L982.

Olayinka Oluwatosin Abegunde, Esther Titilayo Akinlabi, O. P. O. S. A. and Ude, A. U. (2019). Overview of thin film deposition techniques. *AIMS Mater. Sci.*, 6(2):174–199.

P., C. and et al (2014). *Superconductivity,3rd Eddition*. Elsevier, Netherlands.

Pankove, J. I. (1975). *Optical processes in semiconductors*. Courier Corporation, New York.

Perdew, J. P., Burke, K., and Ernzerhof, M. (1996). Generalized gradient approximation made simple. *Phys. Rev. Lett.*, 77(18):3865–3868.

Perdew, J. P. and Zunger, A. (1981). Self-interaction correction to density-functional approximations for many-electron systems. *Phys. Rev. B*, 23(10):5048–5079.

Piela, L. (2020). *Ideas of Quantum Chemistry*. Elsevier, Warsaw, Poland, 2nd edition.

Pike, N. A., Pachter, R., Martinez, A. D., and Cook, G. (2022). Computational analysis of the optical response of ZnSe with d-orbital defects. *J. Phys. Condens. Matter*, 34(20):205402.

Ponci, S., Margine, E. R., Verdi, C., and Giustino, F. (2016). EPW: Electron–phonon coupling, transport and superconducting properties using maximally localized Wannier functions. *Comput. Phys. Commun.*, 209:116–133.

Pradhan, K. and Das, S. K. (2017a). A new route to enhance the ferromagnetic transition temperature in diluted magnetic semiconductors. *Scientific Reports*, 7(1):9603.

Pradhan, K. and Das, S. K. (2017b). A new route to enhance the ferromagnetic transition temperature in diluted magnetic semiconductors. *Sci. Rep.*, 7(1):9603.

Pustovit and et.al (2016). Metamorphoses of electronic structure of FeSe-based superconductors. *Low Temp. Phys.*, 42(11):1268–1283.

Rachidi, A., Atmani, E. H., Fazouan, N., and Boujnah, M. (2016). A study by ab-initio calculation of structural and electronic properties of semiconductor nanostructures based on znse. *Mater. Sci. Appl.*, 07(09):562–573.

Radevici, I., Nedeoglo, N., Sushkevich, K., Huhtinen, H., Nedeoglo, D., and Paturi, P. (2016). Magnetic and luminescent properties of vanadium-doped ZnSe crystals. *Phys. B Condens. Matter*, 503:11–17.

Rajpal, S. and Kumar, S. R. (2018). Thermoluminescent properties of nanocrystalline ZnTe thin films: Structural and morphological studies. *Phys. B Condens. Matter*, 534(December 2017):145–149.

Robinson, W. (2020). Wide Band Gap Chalcogenide Semiconductors. *Chem. Rev.*, 120(9):4007–4055.

Romanin, D., Ummarino, G. A., and Piatti, E. (2021). Migdal-Eliashberg theory of multi-band high-temperature superconductivity in field-effect-doped hydrogenated (111) diamond. *Appl. Surf. Sci.*, 536(February 2020):147723.

Sadique, M. J. and Shahjahan, M. (2018). The role of the Mn, Fe and La dopants on magnetic properties and electronic structures of strontium titanate quinary compounds. *J. Sci. Adv. Mater. Devices*, 3(3):342–347.

Sagadevan, S. and Das, I. (2017). Chemical bath deposition (cbd) of zinc selenide (znse) thin films and characterisation. *Aust. J. Mech. Eng.*, 15(3):222–227.

Saha and et.al (2020). Electrodeposition Fabrication of Chalcogenide Thin Films for Photovoltaic Applications. *Electrochem 2020,*, 1:286–321.

Samarth, N. and Furdyna, J. K. (1988). Diluted Magnetic Semiconductors. *MRS Bull.*, 13(6):32–36.

Sato, K. and Katayama-Yoshida, H. (2002). Ab initio study on the magnetism in ZnO-, ZnS-, ZnSe- and ZnTe-based diluted magnetic semiconductors. *Phys. Status Solidi Basic Res.*, 229(2):673–680.

Sato, T., Souma, S., Nakayama, K., Terashima, K., Sugawara, K., Takahashi, T., Kamihara, Y., Hirano, M., and Hosono, H. (2008). Superconducting gap and pseudogap in iron-based layered superconductor La(O1-xFx)FeAs. *J. Phys. Soc. Japan*, 77(6).

Schrodi, F., Aperis, A., and Oppeneer, P. M. (2019). Increased performance of Matsubara space calculations: A case study within Eliashberg theory. *Phys. Rev. B*, 99(18):184508.

Search, H., Journals, C., Contact, A., Iopscience, M., and Address, I. P. (2003). Curie temperatures of III-V diluted magnetic. *EPL (Europhysics Lett.*, 61:403.

Setyawan, W. and Curtarolo, S. (2010). High-throughput electronic band structure calculations : Challenges and tools. *Comput. Mater. Sci.*, 49(2):299–312.

Shaaban, E. R., Almohammedi, A., Yousef, E. S., Ali, G. A., Chong, K. F., Adel, A., and Ashour, A. (2018). Structural, optical and electrical characteristics of sulfur incorporated ZnSe thin films. *Optik (Stuttg).*, 164:527–537.

Shannon, R. D. (1976). Revised effective ionic radii and systematic studies of interatomic distances in halides and chalcogenides. *Acta Crystallogr. Sect. A*, 32(5):751–767.

Sharma, D. C., Srivastava, S., Vijay, Y. K., and Sharma, Y. K. (2013). Preparation and characterization of the chromium doped ZnTe thin films. *Adv. Mater. Lett.*, 4(1):68–70.

Sharma, J., Singh, H., Singh, T., and Thakur, A. (2018). Structural, optical and photo-electrical properties of nanocrystalline ZnSe thin films. *J. Mater. Sci. Mater. Electron.*, 29(7):5688–5695.

Shibauchi and et.al (2020). Exotic Superconducting States in FeSe-based Materials. *J. Physicsal Soc. Japan*, 89(102002):1–34.

Shikha, D., Mehta, V., Sharma, J., and Chauhan, R. P. (2017). Study of structural, optical and electrical parameters of ZnSe powder and thin films. *J. Mater. Sci. Mater. Electron.*, 28(12):8359–8365.

Si, Q., Yu, R., and Abrahams, E. (2016). High-temperature superconductivity in iron pnictides and chalcogenides. *Nat. Rev. Mater.*, 1.

Singh, H., Singh, M., Singh, J., Bansod, B. S., Singh, T., Thakur, A., Wani, M. F., and Sharma, J. (2019). Composition dependence study of thermally evaporated nanocrystalline ZnTe thin films. *J. Mater. Sci. Mater. Electron.*, 30(4):3504–3510.

Singh, H., Singh, T., and Sharma, J. (2018). Review on optical, structural and electrical properties of ZnTe thin films: effect of deposition techniques, annealing and doping. *ISSS J. Micro Smart Syst.*, 7(2):123–143.

Singh, P., Sharma, P., Sharma, V., and Thakur, A. (2017). Linear and non-linear optical properties of $ag-dopedge2sb2te5$ thin films estimated by single transmission spectra. *Semicond. Sci. Technol.*, 32(4):045015.

Sizoo, G. and Onnes, H. (1925). G.J. Sizoo and H.K. Onnes, Commun. Phys. Lab. Univ. Leiden, No. 180b (1925). *Commun. Phys. Lab. Univ. Leiden*, (180b):1925.

Slade, T. J., Furukawa, N., Smith, T. R., Schmidt, J., Mudiyanselage, R. S. D., Wang, L.-L., Xie, W., Bud'ko, S. L., and Canfield, P. C. (2023). High-temperature ferromagnetism in cr 1+ x pt 5- x p. *Phys. Rev. Mat.*, 7(2):024410.

Snider and et. al (2020). Room-temperature superconductivity in a carbonaceous sulfur hydride. *Nature*, 586(15):373–377.

Soykan, C. and Kart, S. Ö. (2012). Structural, mechanical and electronic properties of ZnTe polymorphs under pressure. *J. Alloys Compd.*, 529:148–157.

Stanton, J. F. (2001). *A Chemist's Guide to Density Functional Theory*, volume 123. Wiley-VCH: Weinheim, New York.

Su, K. and Wang, Y. (2010). Electronic structure and linear optical properties of ZnSe and ZnSe:Mn. *J. Nanosci. Nanotechnol.*, 10(3):1857–1859.

Swanepoel, R. (1983). Determination of the thickness and optical constants of amorphous silicon. *Journal of Physics E: Scientific Instruments*, 16(12):1214.

Tahashi, M., Wu, Z., Goto, H., Hayashi, Y., and Ido, T. (2009). Effect of vanadium doping on structure and properties of ZnSe films prepared by metal-organic vapor phase epitaxy. *Mater. Trans.*, 50(4):719–722.

Tan, Z., Xiao, W., Wang, L., and Yang, Y. (2012). Magnetic properties of ZnS doped with noble metals (X = Ru, Rh, Pd, and Ag). *J. Appl. Phys.*, 112(12).

Tanaka, M. (2020). Recent progress in ferromagnetic semiconductors and spintronics devices. *Jpn. J. Appl. Phys.*, 60(1).

Timrov, I., Marzari, N., and Cococcioni, M. (2018). Hubbard parameters from density-functional perturbation theory. *Phys. Rev. B*, 98(8):1–15.

Togo, A. and Tanaka, I. (2015). First principles phonon calculations in materials science. *Scr. Mater.*, 108:1–5.

Trujillo, A. G., Aguilera, M. L. A., Morán, D. A. R., Arellano, M. G., Acevedo, A. M., Cruz, G. C., Ipn, E., Básica, F., and México, D. F. (2012). Optical and electrical properties of znte thin films using deposition technique. *Int. J. Innov. Appl. Stu.*

Tsymbal, E. Y. and Igor Zutic Nasirpouri, F. (2013). *Spintronics Handbook: Spin Transport and Magnetism, Second Edition Semiconductor Spintronics*, volume 53.

Vidberg, H. J. and Serene, J. W. (1977). Solving the Eliashberg equations by means of N-point Padé approximants. *J. Low Temp. Phys.*, 29(3-4):179–192.

Villa-Cortés, S. and Baquero, R. (2018). On the calculation of the inverse isotope effect in PdH(D): A Migdal-Eliashberg theory approach. *J. Phys. Chem. Solids*, 119(March):80–84.

Wang, C.-Z., Yu, R., and Krakauer, H. (1994). First principles linear response calculations of lattice dynamics for cucl. *Physical review letters*, 72(3):368.

Wang, Y., Shang, S.-L., Fang, H., Liu, Z.-K., and Chen, L.-Q. (2016a). First-principles calculations of lattice dynamics and thermal properties of polar solids. *npj Computational Materials*, 2(1):1–10.

Wang, Y., Shang, S. L., Fang, H., Liu, Z. K., and Chen, L. Q. (2016b). First-principles calculations of lattice dynamics and thermal properties of polar solids.

Wolfgang Nolting · Anupuru Ramakanth (2020). *Quantum Theory of Magnetism*. Number July. Springer Berlin, Heidelberg.

Xie, R., Li, Y., Jiang, L., and Zhang, X. (2014). Applied Surface Science Insights into the microstructural and physical properties of colloidal Fe : ZnSe nanocrystals. *Appl. Surf. Sci.*, 317:469–475.

Yaakob, M. K., Hussin, N. H., Taib, M. F., Kudin, T. I., Hassan, O. H., Ali, A. M., and Yahya, M. Z. (2014). First principles LDA+U calculations for ZnO materials. *Integr. Ferroelectr.*, 155(1):15–22.

Yadav, K., Dwivedi, Y., and Jaggi, N. (2015). Structural and optical properties of Ni doped ZnSe nanoparticles. *J. Lumin.*, 158:181–187.

Yadav, P. S. and Pandey, D. K. (2012). A DFT study for the structural and electronic properties of Zn m Se n nanoclusters. *Appl. Nanosci.*, 2(3):351–357.

Yahyaoui, M., Amdouni, S., and Kallel, T. (2020). K.P modeling of the density of states of II-VI semiconductors. *Int. J. Sci. Technol. Res.*, 9(1):448–453.

Yang, J. H., Chen, S., Yin, W. J., Gong, X. G., Walsh, A., and Wei, S. H. (2009). Electronic structure and phase stability of MgTe, ZnTe, CdTe, and their alloys in the B3, B4, and B8 structures. *Phys. Rev. B - Condens. Matter Mater. Phys.*, 79(24):1–7.

Yang, T. R. and Lu, C. C. (2000). Infrared studies and optical characterization of ZnSe1-xTex molecular beam epitaxial films. *Phys. B Condens. Matter*, 284-288(PART II):1187–1188.

Yang, X.-T., Lin, J.-H., Khan, M. S., Zou, B.-S., and Shi, L.-J. (2019). Interstitial zn-modulated ferromagnetism in co-doped znse. *Materials Research Express*, 6(10):106121.

You, J.-Y., Dong, X.-J., Gu, B., and Su, G. (2023). Possible room-temperature ferromagnetic semiconductors. *Chinese Physics Letters*, 40(6):067502.

You, J. Y., Gu, B., Maekawa, S., and Su, G. (2020). Microscopic mechanism of high-temperature ferromagnetism in Fe, Mn, and Cr-doped InSb, InAs, and GaSb magnetic semiconductors. *Phys. Rev. B*, 102(9):1–13.

Younus, I. A., Ezzat, A. M., and Uonis, M. M. (2020). Preparation of ZnTe thin films using chemical bath deposition technique. *Nanocomposites*, 6(4):165–172.

Yu, Z., Xu, Z., Wu, X., and Ma, Z. (2014). Electronic structure and optical properties of ZnSe from first-principles calculations. *Optoelectron. Devices Integr. OEDI 2014*, pages 3–5.

Zaari, H., Boujnah, M., El Hachimi, A., Benyoussef, A., and El Kenz, A. (2014a). Optical properties of ZnTe doped with transition metals (Ti, Cr and Mn). *Opt. Quantum Electron.*, 46(1):75–86.

Zaari, H., Boujnah, M., El Hachimi, A. G., Benyoussef, A., and Kenz, A. A. E. (2014b). Electronic structure, optical and magnetic properties of Zn1-xMxTe (M = Ti, Cr and Mn)

Ab initio calculations. In *Proc. 2014 Int. Renew. Sustain. Energy Conf. IRSEC 2014*, number June, pages 611–614. IEEE.

Zargar and et.al (2014). Structural , Electrical and Magnetic Behaviour of FeTe0.5Se0.5 Superconductor. *J Supercond Nov Mag*, 27:897–901.

Zelai, T., Hakami, O., and Najari, M. (2022). Exploring the electronic structure, and ferromagnetism of Co-doped ZnTe for spintronics: an experimental and DFT modelling approach. *Eur. Phys. J. Plus*, 137(3).

Zhang (2014). *Electric-Field Control of Magnetization and Electronic Transport in Ferromagnetic/Ferroelectric Heterostructures*. Springer, Berlin Heidelberg.

Zhang, Q., Li, H., Ma, Y., and Zhai, T. (2016). ZnSe nanostructures: Synthesis, properties and applications. *Prog. Mater. Sci.*, 83:472–535.

Žutić, I., Fabian, J., and Sarma, S. D. (2004). Spintronics: Fundamentals and applications. *Rev. Mod. Phys.*, 76(2):323–410.